

**APPARATUS FOR POSITRONIUM  
PRODUCTION VIA RYDBERG  
CESIUM CHARGE-EXCHANGE**

RICHARD THAI

A DISSERTATION SUBMITTED TO THE FACULTY OF  
GRADUATE STUDIES IN PARTIAL FULFILMENT OF THE  
REQUIREMENTS FOR THE DEGREE OF

DOCTOR OF PHILOSOPHY

GRADUATE PROGRAM IN PHYSICS AND ASTRONOMY

YORK UNIVERSITY

TORONTO, ON

May 2021

© RICHARD THAI, 2021

# *Abstract*

This dissertation outlines research conducted with positrons towards the production of positronium via charge-exchange with Rydberg cesium atoms. Positronium is a purely leptonic atomic system that is ideal for tests of quantum electrodynamics (QED) theory. A frozen neon crystal moderator produces low-energy positrons from a radioactive source that are magnetically guided towards a buffer-gas accumulator. The buffer-gas accumulator has been optimized to store large numbers of positrons ( $> 40$  million in 2 minutes) for a long time to perform a variety of experiments. The 200 meV energy width of the accumulated positrons is suitable for charge-exchange experiments. The positrons are then magnetically guided through a  $90^\circ$  bend towards an apparatus where charge-exchange takes place.

The experimental techniques to produce and detect Rydberg positronium are described and the progress is presented. A data acquisition system has been developed to detect positron signatures based on the coincidence-timing of back-to-back annihilations on a single-event basis where time and energy analysis cuts allow strict criteria to distinguish signal from background.

The long-term goal of the research program is to perform precision spectroscopy of the internal structure of Rydberg positronium. These measurements can be used to determine fundamental constants of nature and to test QED theory. A deviation from the QED predictions can be an indication of physics beyond the Standard Model. Physics beyond the Standard Model can provide a solution to unsolved problems, such as the matter-antimatter imbalance that is observed today.

*For my mother*

# *Acknowledgements*

I would like to thank my supervisor, Cody Storry, for all that he has taught me throughout the years. It's been a great experience working in the positron lab. He's taught me how to be an excellent experimentalist and was always willing to give me a hand and encouragement when I needed it. I'm grateful for the opportunities to work on the project at the McMaster Nuclear Reactor and with the ATRAP collaboration at CERN.

I would like to thank Eric Hessels for all his input and advice during research meetings. He's a brilliant experimentalist and has always made time to chat with me about the experiment. He's treated me like I was one of his students and I truly appreciated that. I had a close connection to his lab, and I was able to borrow equipment that was critical for this work.

I'd like to thank Matthew Weel for being the post-doc during my first two years. He was the go-to person to ask any questions and to help brainstorm ideas. I learned a lot by directly working with him in the lab. I'd also like to thank Matthew George for providing any advice related to the positron accumulator. Thank you to Greg Koyanagi for being so helpful around the lab whenever I needed another set of hands, and for sharing ideas on how to improve the apparatus.

Thank you to my friends in the Hessels 309 lab: Kosuke Kato, Nikita Bezginov, Taylor Skinner, and Travis Valdez. They've always made me feel like I was a part of the group and I've enjoyed our time in and out of the labs. They're such a hard-working group and I am proud of all their accomplishments.

I've had the chance to work with several undergraduate students throughout the years and I thank them for their contributions.

Thank you to Gloria Orchard and Sampa Bhadra for letting me borrow NIM electronics that have been essential for the detection system. I'd like to thank William van Wijngaarden for providing his 852 nm laser system when I was in urgent need.

Thank you to the graduate program assistants, Marlene Caplan and Cristalina Del Biondo. They were a pleasure to chat with and have helped me stay on track with all the administrative parts of graduate school.

Thank you to Marko Horbatsch for being a part of my committee. His feedback has been valuable and he asked great questions about theory during the evaluations. He was my first physics professor and his course was a great introduction to the physics program at York.

I'd like to thank my beloved partner, Tina. You were always there for me and gave me the boost to get through tough days. Thank you for all your patience, understanding, and listening to me talk about positrons. You always believe in me and give me your full support, and I'll always do the same for you.

Thank you to my parents, brother, and sister for all their support. My parents worked so hard to raise me and my siblings, and have set a great example for me.

My mom was the kindest and loving person I've ever known. I will always cherish the fun times we've had together, and I'll never forget the life lessons you've taught me. Thank you for being my wonderful mother.

# Contents

<b>Abstract</b>	<b>ii</b>
<b>Dedication</b>	<b>iii</b>
<b>Acknowledgements</b>	<b>iv</b>
<b>List of Figures</b>	<b>ix</b>
<b>List of Tables</b>	<b>xiii</b>
<b>1 Introduction</b>	<b>1</b>
1.1 Overview of Positronium Spectroscopy . . . . .	1
1.1.1 Methods for Ps formation . . . . .	5
1.2 Resonant Rydberg Charge-exchange . . . . .	6
1.3 Experiment Overview . . . . .	8
1.4 Energy Level Structure of Positronium and Cesium . . . . .	12
1.4.1 States of Cesium and Positronium for Resonant Charge- Exchange . . . . .	14
1.5 Estimates for Charge-Exchange . . . . .	16
<b>2 Positron System</b>	<b>18</b>
2.1 Positron Detection System . . . . .	18
2.1.1 Gamma Detectors . . . . .	19
2.1.1.1 Photon Counting . . . . .	21
2.1.2 Faraday Cups . . . . .	23
2.1.3 Plasma Imaging . . . . .	24

---

2.2	$^{22}\text{Na}$ Source . . . . .	26
2.3	Positron Moderation . . . . .	27
2.3.1	Moderator Growth . . . . .	31
2.3.2	Radial Profile of the Moderated $e^+$ Beam . . . . .	34
2.4	Penning Trap Theory . . . . .	34
2.5	Buffer-Gas Trap . . . . .	38
2.5.1	Three-Stage Penning Trap Electrodes . . . . .	39
2.5.2	Moderated Positron Beam Energy . . . . .	41
2.5.3	Inelastic Collisions with $\text{N}_2$ Buffer-Gas . . . . .	43
2.5.4	Rotating Wall . . . . .	44
2.6	Positron Accumulation . . . . .	49
2.6.1	Pulsed Beam . . . . .	51
2.6.2	Ramped Beam . . . . .	56
<b>3</b>	<b>Magnetic Transfer Guide</b> . . . . .	<b>58</b>
3.1	Magnetic Field Model . . . . .	58
3.2	Transfer Detection and Optimization . . . . .	61
3.3	Ramped $e^+$ Beam Energy Distribution . . . . .	63
<b>4</b>	<b>Laser Systems</b> . . . . .	<b>66</b>
4.1	852 nm Laser System . . . . .	66
4.2	Rydberg-Excitation Laser System . . . . .	69
<b>5</b>	<b>Positronium Experimental System</b> . . . . .	<b>74</b>
5.1	Ps Apparatus Vacuum System . . . . .	74
5.2	Cesium Oven . . . . .	75
5.3	Liquid Nitrogen-Cooled Components . . . . .	80
5.3.1	Dewar . . . . .	80
5.3.2	Cold Trap and Surrounding Components . . . . .	82
5.4	Cesium Laser Excitation to Rydberg States . . . . .	84
5.4.1	$6\text{S}_{1/2}$ to $6\text{P}_{3/2}$ Excitation . . . . .	85
5.4.1.1	Laser absorption . . . . .	85

---

5.4.1.2	Fluorescence Imaging . . . . .	88
5.4.1.3	Density of ground state Cs . . . . .	89
5.4.2	$6P_{3/2}$ to $nD_{5/2}$ Excitation . . . . .	90
5.4.2.1	EIT detection . . . . .	90
5.4.2.2	Fluorescence measurements for Rydberg Density and Lifetime . . . . .	91
5.5	In-Vacuum Magnetic Field Coils . . . . .	95
5.6	Detection Region and Quadrupole Guide . . . . .	97
5.7	State-Selective Field-Ionization Detector . . . . .	107
5.8	Data Acquisition . . . . .	113
5.8.1	Detection of Triplet Ps Formation on Metal Surface . . . . .	123
5.9	Rydberg Positronium Production Trials . . . . .	125
<b>6</b>	<b>Conclusion</b>	<b>137</b>
	<b>Bibliography</b>	<b>141</b>

# List of Figures

1.1	Apparatus Overview . . . . .	10
1.2	Diagram of Rydberg Charge-Exchange . . . . .	11
1.3	$n = 11$ Triplet Ps* Fine Structure Intervals for Precision Measurements . . . . .	13
1.4	Comparison of Cs and Ps energy levels . . . . .	15
2.1	Gamma Detection Electronics Diagram . . . . .	22
2.2	Faraday Cup Signal . . . . .	24
2.3	Plasma-Imaging System Schematic . . . . .	25
2.4	Moderated $e^+$ Filter Through the Jog Chamber . . . . .	29
2.5	$e^+$ Annihilation Rate for Various Overjog and Jog Vertical Coil Currents . . . . .	30
2.6	Moderator Growth Plots . . . . .	32
2.7	Moderator Temperature Scan . . . . .	33
2.8	Neon Moderator Decay Plot . . . . .	33
2.9	Moderated $e^+$ Beam Image . . . . .	35
2.10	Ideal Penning Trap Geometry . . . . .	36
2.11	Buffer-Gas Trap Schematic . . . . .	39
2.12	Moderated $e^+$ Energy Distribution . . . . .	43
2.13	Expected Moderated $e^+$ Energy Distribution without Magnetic Mirroring . . . . .	44
2.14	Rotating Wall Schematic . . . . .	47
2.15	Rotating Wall Frequency Scan . . . . .	49
2.16	Rotating Wall Amplitude Scan . . . . .	50

---

2.17	Plasma Image . . . . .	51
2.18	Rotating Wall Radial Compression Scan . . . . .	52
2.19	On-Axis Electric Potentials During $e^+$ Accumulation . . . . .	53
2.20	Number of $e^+$ Accumulated Over Time . . . . .	54
2.21	Nitrogen Buffer-Gas Scan . . . . .	54
2.22	$e^+$ Lifetime in the Buffer-Gas Trap . . . . .	55
2.23	Positron Diameter and Number Plot . . . . .	55
2.24	On-axis Potential During $e^+$ Ramp . . . . .	57
3.1	Magnetic Field Model of Transfer-Guide $e^+$ Trajectory . . . . .	60
3.2	Magnetic Field Along Transfer Guide . . . . .	61
3.3	Moderated $e^+$ Beam Image in a Reduced Source Magnetic Field . . . . .	63
3.4	Voltage Distribution of Triggers During $e^+$ Ramp . . . . .	64
4.1	Laser Frequency Stabilization Optics Schematic . . . . .	67
4.2	Doppler-Free Spectrum within a Vapour Cell . . . . .	69
4.3	Vapour Cell EIT-SAS Spectrum . . . . .	71
4.4	Vapour Cell Rydberg Fluorescence Images . . . . .	73
5.1	Cesium Oven . . . . .	76
5.2	Oven Cross-Section . . . . .	77
5.3	Liquid Cesium Vapour Pressure Curve . . . . .	78
5.4	Cesium Oven Angular Distribution . . . . .	79
5.5	Liquid Nitrogen Dewar System . . . . .	81
5.6	Liquid Nitrogen Cooling Thermal Paths . . . . .	82
5.7	Cross-section View of Liquid Nitrogen Cooled Components . . . . .	83
5.8	Thermal Cs Beam $6S_{1/2} \rightarrow 6P_{3/2}$ Laser Absorption Scan . . . . .	86
5.9	1D Speed Distribution Along Laser . . . . .	87
5.10	CCD Image of $6P_{3/2} \rightarrow 6S_{1/2}$ Fluorescence . . . . .	88
5.11	852 nm Absorption Scan as a Function of Wavelength . . . . .	90
5.12	Ground State Cesium Density Plot . . . . .	91
5.13	EIT from Thermal Cs Beam . . . . .	92

---

5.14	CCD Image of Rydberg Cs Fluorescence . . . . .	94
5.15	Intensity Profile of Rydberg Fluorescence . . . . .	94
5.16	In-vacuum Coils and Cesium Oven Photograph . . . . .	96
5.17	On-Axis Magnetic Field of Vacuum Coils . . . . .	97
5.18	Electrostatic Quadrupole Guide Overview . . . . .	98
5.19	Low-Field Stark Fan . . . . .	100
5.20	High-Field Stark Fan . . . . .	101
5.21	Electrostatic Quadrupole Potentials and Electric Field . . . . .	102
5.22	Electrostatic Quadrupole Guide Energy Efficiency . . . . .	103
5.23	Ps* Lifetimes . . . . .	104
5.24	Electrostatic Quadrupole Trajectories . . . . .	105
5.25	Electrostatic Quadrupole $l$ -state Fraction Guided . . . . .	106
5.26	State-Selective Field-Ionization Schematic . . . . .	108
5.27	Field Ionization Equipotential Contours and Trajectories . . . . .	110
5.28	Monte Carlo Simulation of Ps* Through SS-FI with Various Block- ing Wire Diameters . . . . .	111
5.29	Wire Mesh-2 and Mesh-3 . . . . .	112
5.30	Assembled SS-FI . . . . .	113
5.31	Data Acquisition System Overview . . . . .	114
5.32	Sample Coincidence Signal . . . . .	115
5.33	Coincidence Time Delay Analysis . . . . .	117
5.34	$e^+$ Reference Coincidence Gamma Spectrum . . . . .	119
5.35	Background Reference Coincidence Gamma Spectrum . . . . .	120
5.36	False Coincidence Scatter Events . . . . .	121
5.37	Ramped $e^+$ Beam Trigger Timestamps . . . . .	122
5.38	Triplet Ps Coincidence Spectrum Formed from Metal Surface . . . . .	124
5.39	Magnet Coil Steering Trends . . . . .	126
5.40	Blocking the Ramped $e^+$ Beam with Nozzle Bias . . . . .	128
5.41	Density Histogram of Upstream Coincidence Gamma Spectrum . . . . .	130
5.42	False Coincidences from Single-Photon Events . . . . .	131

---

5.43 $e^+$ Energy Scan with Laser On/Off (0.1 mW of 852 nm) . . . . .	132
5.44 $e^+$ Energy Scan with Laser On/Off (1 mW of 852 nm) . . . . .	133

# List of Tables

1.1	Ps Spectroscopy Summary . . . . .	4
2.1	Scintillator Properties . . . . .	20
2.2	Electrode Parameters . . . . .	40
2.3	$e^+$ Cooling Gases . . . . .	48
3.1	Transfer Magnet Coils . . . . .	59
5.1	Rydberg Fluorescence Rate Calculation Parameters . . . . .	93
5.2	Detector Fit Parameters . . . . .	116
5.3	Ps Trial Results . . . . .	129
5.4	Energy Scans with Various Experiment Parameters . . . . .	134
5.5	Ps Trial 2 Results . . . . .	135

# Chapter 1

## Introduction

### 1.1 Overview of Positronium Spectroscopy

Positronium (Ps) is an unstable bound-state atomic system consisting of an electron ( $e^-$ ) and its antimatter-counterpart, a positron ( $e^+$ ). The  $e^+$  was predicted in 1928 by Paul Dirac when he began to formulate a quantum field theory (QFT) to combine quantum mechanics with special relativity [1]. The  $e^+$  was experimentally discovered by Carl Anderson in 1932 [2], which led to Anderson winning the Nobel prize in physics. The  $e^+$  is identical to the  $e^-$  in all aspects except that it has an elementary charge of  $+e$  instead of  $-e$ .

When a  $e^+$  comes in contact with an  $e^-$ , the particles annihilate into gamma photons with a total energy governed by Einstein's mass-energy equivalence principle

$$E = m_{total}c^2 = 2m_e c^2 \tag{1.1}$$

where the total energy of the two photons is  $E$ , and the masses of the  $e^+$  and  $e^-$  is  $m_e$ . In energy units, the mass of each particle is 511 keV/ $c^2$ . In the rest frame of the  $e^-$  and  $e^+$  system, the photons must be emitted in opposite directions with 511 keV each to conserve energy and momentum.

A  $e^+$  can be bound to an  $e^-$  before annihilation occurs, to form positronium. This exotic atom was discovered in 1951 by Martin Deutsch at MIT by studying the interaction of  $e^+$  with various gases [3]. Ps can be formed in the singlet state (parapositronium), where the spin of the  $e^-$  and  $e^+$  are anti-aligned or it can be formed in the triplet state (orthopositronium) where the spins are aligned. In the ground state, parapositronium has an annihilation lifetime of approximately 0.1244 ns whereas orthopositronium has a lifetime of approximately 138.6 ns. In highly-excited states, also known as Rydberg states, the lifetime is dominated by the radiative lifetime. These states are long-lived due to the small spatial overlap of the  $e^+$  and  $e^-$  wavefunction, leading to small probabilities to annihilate and radiative lifetimes on the scale of microseconds or more.

Ps is a purely leptonic system (composed of point particles) that is ideal for testing bound-state quantum electrodynamics (QED) theory and has several advantages over measurements of other atoms. Precision measurements of the energy level structure can be used to infer values of fundamental constants of nature such as the Rydberg constant,  $R_\infty$ , and the fine-structure constant,  $\alpha$ . These measurements can be compared to theoretical QED calculations, where corrections are expressed in terms of order  $\alpha$  or  $R_\infty$ . Fundamental constants can often be expressed in terms of other fundamental constants. For example, the fine structure constant can be expressed as

$$\alpha = \frac{e^2}{4\pi\epsilon_0\hbar c} = \sqrt{\frac{2hR_\infty}{m_e c}} \quad (1.2)$$

The fine-structure constant sets the strength of the electromagnetic coupling between electromagnetic fields and charged particles. Additionally, Ps is purely leptonic so nuclear structure effects do not contribute to uncertainties as in all other atoms. Recoil effects and hyperfine corrections in Ps are not suppressed by factors of  $m/M$  such as in hydrogen where  $m/M \approx 1/1836$ . For Ps,  $m/M = 1$ , hence it is sensitive to high-order corrections, and the ratio does not contribute to the uncertainty.

An example of a nuclear structure effect is the finite size of the proton in spectroscopic measurements. The finite size of the proton is one of the contributing effects of the Lamb shift [4]. A measurement of the 2S–2P interval in muonic hydrogen resulted in a determination of the proton size that was 5 standard deviations from the accepted value [5]. This discrepancy has been known as the “proton radius puzzle”. A recent measurement of the 2S–2P Lamb shift in atomic hydrogen is consistent with the muonic hydrogen measurement and has resolved this discrepancy [6]. The energy correction due to the nuclear structure of the proton is

$$E_{NS} = R_{\infty} \delta_{l0} \frac{C_{NS}}{n^3} r_p^2 \quad (1.3)$$

where  $C_{NS}$  is a leading order coefficient correction due to the nuclear structure (proton radius) [7]. The Kronecker delta term,  $\delta_{l0}$ , provides the energy correction for  $S$  states where the  $e^-$  has a non-zero probability to be inside the proton. Precision hydrogen spectroscopy measurements of the proton radius are highly correlated to the Rydberg constant, as a consequence, a discrepancy in the proton radius could be linked to a discrepancy in the Rydberg constant. Precision spectroscopy of Ps is highly motivated as it can provide an independent measurement of the Rydberg constant that is unaffected by nuclear structure.

Table 1.1 outlines the most recent precision measurements within the  $n = 1$  and  $n = 2$  manifold of Ps. It has been over 20 years since the last precision measurement and interest has re-emerged in Ps where research is active in topics such as Ps precision spectroscopy [8], Bose-Einstein condensation of Ps [9], and Ps to test anti-matter gravity [10].

Research in Rydberg Ps (Ps\*) spectroscopy has been a growing field over the past 10 years with improved techniques of efficient ground state Ps production and excitation to Rydberg states. Precision microwave spectroscopy of Rydberg states

Experiments		
Interval	Measurement	Group (Year)
$1S$ Hyperfine	203 389 100(740) kHz	Ritter, M. (1984) [11]
	203 387 500(1600) kHz	Mills, A. P. (1975) [12]
$1S - 2S$	1 233 607 216.4(3.2) MHz	Mills, A. P. (1970) [13]
$2^3S_1 - 2^3P_0$	18 499 650(4176) kHz	Hagena, D. (1993) [14]
	18 504 100(10100) kHz	Hatamian, S. (1993) [15]
	18 501 020(62) kHz	Gurung, L. (2020) [8]
$2^3S_1 - 2^3P_1$	13 012 420(1680) kHz	Hagena, D. (1993) [14]
	13 001 300(4000) kHz	Hatamian, S. (1993) [15]
$2^3S_1 - 2^3P_2$	8 624 380(1500) kHz	Hagena, D. (1993) [14]
	8 628 400(2800) kHz	Mills, A. P. (1975) [16]
	8 619 600(2800) kHz	Hatamian, S. (1993) [15]
Theory		
$1S$ Hyperfine	203 391 700(600) kHz	Sources in Karshenboim (2004) [17]
$1S - 2S$	1 233 607 222.2(6) MHz	
$2^3S_1 - 2^3P_0$	18 498 250(90) kHz	
$2^3S_1 - 2^3P_1$	13 012 410(90) kHz	
$2^3S_1 - 2^3P_2$	8 625 700(90) kHz	

TABLE 1.1: An overview of latest Ps spectroscopy measurements. The theory values have been summarized in Karshenboim, S. G. (2004) [17], where sources are cited within.

can be used for improved measures of fundamental constants of nature such as the Rydberg constant and fine-structure constant.

A research group lead by Dr. David Cassidy has made significant progress in the field Ps\* research. They have developed an apparatus to use a trap-based  $e^+$  beam that is optimized for Ps laser spectroscopy, where they implant time-bunched 4 ns wide beams of  $e^+$  into a target to produce ground-state Ps atoms [18]. The ground-state atoms are laser-excited to the short-lived 2P states, and then laser-excited to the Rydberg states, ranging from  $n = 10 - 22$ . Single shot positron annihilation lifetime spectroscopy (SSPALS) is a fast detection technique that is used to measure the change in Ps lifetime distribution when different states of Ps are produced [19]. The fluorescence lifetimes of Ps\* and how it scales have also been measured with time-of-flight (TOF) experiments [20]. By applying electric fields at the Ps production region, they have demonstrated laser-excitation

to the Stark-shifted states within a Rydberg manifold [21]. The group has also demonstrated manipulating the motion of  $\text{Ps}^*$  with an electrostatic quadrupole guide [22] and velocity-selection with a curved electrostatic quadrupole guide [23]. Most recently, they have performed the most precise measurement to date of the  $2^3\text{S}_1 \rightarrow 2^3\text{P}_0$  fine structure interval where they obtained a transition frequency of  $\nu_0 = 18\,501.02(62)$  MHz [8]. This result has a  $4.5\sigma$  discrepancy from theory, which is motivation for more independent experiments and to check for any discrepancies in current theory.

### 1.1.1 Methods for Ps formation

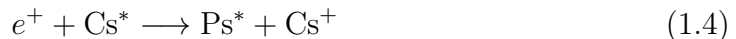
The measurements listed in Table 1.1 are of Ps in low-level states. Ps atoms were produced from high-energy  $e^+$  incident on metal targets [24], powders (such as  $\text{SiO}_2$  [25],  $\text{MgO}$  [26]) and gases [27]. Since these measurements, methods for producing large numbers of low-energy  $e^+$  have been developed with the use of solid neon moderators to produce low-energy  $e^+$  [28], and the buffer-gas trap to accumulate these low-energy  $e^+$  for a new era of measurements [29].

Recently, a group used buffer-gas accumulated  $e^+$  implanted on mesoporous  $\text{SiO}_2$  films to efficiently produce ground-state Ps within the material [30]. The films contain porous voids with diameters in the range of 4 nm to 16 nm where Ps atoms lose energy via collisions with the internal pore surfaces. The Ps atoms diffuse to the surface after many wall collisions and are emitted with low energies dependent upon the implantation depth, with a low-energy limit determined by the pore size. This technique has produced ground-state Ps with  $\sim 60$  meV that were subsequently laser-excited to produce  $\text{Ps}^*$  [31]. Excitation from the ground-state to Rydberg states requires high-cost pulsed laser systems that generate 243 nm laser light to excite the  $1^3\text{S} - 2^3\text{P}$  state, and an infrared laser excites it to the Rydberg states [32] [33]. To improve the laser excitation efficiency, the  $e^+$  are time-compressed using bunchers to produce short pulses of Ps that overlap with the laser pulse timing [34]. By contrast, the technique used in this experiment

only requires low-cost continuous wave lasers where every  $e^+$  has an opportunity to form Ps directly in a Rydberg state.

## 1.2 Resonant Rydberg Charge-exchange

An efficient, cost-effective technique to create Rydberg atoms is via resonant charge-exchange with thermal Rydberg alkali atoms. This thesis focuses on experimental techniques for producing slow  $e^+$  beams, and the charge-exchange of slow  $e^+$  with a Rydberg cesium ( $\text{Cs}^*$ ) target, where a  $e^+$  can capture a loosely bound cesium (Cs) valence  $e^-$  to form  $\text{Ps}^*$ . The equation demonstrating this process is represented by



$\text{Cs}^*$  can be produced with commercially available continuous-wave lasers with a two-step transition. An 852 nm photon excites the ground state to the first excited state ( $6\text{S}_{1/2} - 6\text{P}_{3/2}$ ), and a 510–520 nm photon drives it to the Rydberg state ( $6\text{P}_{3/2} - n\text{D}_j$ ), where  $n \approx 18$ . Laser technology to address the  $6\text{S}_{1/2} - 6\text{P}_{3/2}$  Cs transition is commonly available in external cavity diode lasers (ECDL), distributed Bragg reflector (DBR) lasers, and distributed-feedback (DFB) lasers that provide narrow line-widths with excess power to saturate the transition ( $I_{\text{sat}} = 2.7 \text{ mW/cm}^2$ ). Low-power tunable lasers at 520 nm are available in ECDL and higher power options are commercially available with a frequency doubling unit to down-convert high power 1040 nm diode laser light to 520 nm. A three-step laser transition using low-power infrared lasers can also efficiently produce Rydberg states. For example, the transition  $6\text{S}_{1/2} \rightarrow 6\text{P}_{3/2} \rightarrow 7\text{S}_{1/2} \rightarrow 18\text{P}_{3/2}$  requires lasers of wavelengths of 852 nm, 1470 nm, and 810 nm. These too are conveniently in the infrared wavelength range and require lower power than the two-step excitation described. Both approaches are viable, but the two-step process is chosen for the reduced cost, simpler laser frequency stabilization system, and the adequate power available for 520 nm diodes to produce  $\text{Cs}^*$ .

This Ps\* production method was demonstrated by the ATRAP collaboration in a two-stage charge-exchange to produce antihydrogen [35, 36]. The second charge-exchange was between Ps\* atoms and trapped antiprotons producing Rydberg antihydrogen. For antihydrogen trapping, this technique has the benefit of producing antihydrogen at the temperature of the antiproton ( $\sim 4$  K). At the cryogenic temperature of the antiprotons, the  $e^+$  have negligible momentum. Another common technique to form antihydrogen is by three-body recombination, where a trapped plasma of antiprotons is heated and mixed with an adjacent trapped  $e^+$  plasma, producing antihydrogen at a higher temperature relative to the double charge-exchange method [37]. Recently, other collaborations have adopted the Ps\*-antiproton charge-exchange to produce beams of antihydrogen [38]. Research in efficient production of Ps\* is important for efficient antihydrogen synthesis at CERN where the supply of antiprotons is shared between  $\sim 10$  collaborations for limited times during the annual beam run.

The cross-section of resonant charge-exchange is large if the speed ( $v$ ) of the  $e^+$  is less than the speed of the Cs valence  $e^-$  ( $v_e$ ), where  $v/v_e < 1$ . The classical radius of the valence  $e^-$  orbit from the nucleus is  $n_{Cs}^2 a_0$ , where  $n_{Cs}$  is the principal quantum number of the Cs target atom and  $a_0 = 0.53 \times 10^{-11}$  m is the Bohr radius. The geometric area of the Rydberg atom is therefore  $n_{Cs}^4 \pi a_0^2$ . The  $n_{Cs}^4$  scaling demonstrates how large the cross-section can be if excited to a high- $n$  state. The speed of the valence  $e^-$  is approximately  $v_e = \alpha c/n_{Cs}$ , where  $\alpha$  is the fine-structure constant and  $c$  is the speed of light. For an  $n_{Cs} = 18$  Cs atom, this corresponds to a speed of approximately 120 000 m/s. For efficient charge-exchange, the  $e^+$  kinetic energy must be below 42 meV ( $v \approx 120$  000 m/s), which is achievable from room-temperature buffer-gas  $e^+$  accumulation where the  $e^+$  have a thermal energy distribution. The Ps\* is produced in a state where the binding energy is similar to the Cs\* binding energy. The Ps\* is produced isotropically due to the random momentum distribution of the valence  $e^-$  and the electric potential hill that slows the  $e^+$  to zero average velocity at the charge-exchange.

The choice of  $n_{Cs}$  determines the state of Ps\* resonantly produced,  $n_{Ps}$ . This determines important parameters such as the lifetime of the Rydberg state and

the electric field required to ionize  $\text{Ps}^*$ , important to determine design constraints for the experimental apparatus. A typical method for Rydberg atom detection is via state-selective field ionization to determine the quantum state of the atom [39]. The Rydberg atom is loosely bound such that a weak electric field is sufficient to ionize the atom with near unit efficiency, and either the ion or  $e^-$  can be collected on a detector. The apparatus for this experiment is designed with the capability for  $\text{Ps}^*$  ionization and detection methods, where either the  $e^+$  can be directed towards or away from a detector.

### 1.3 Experiment Overview

The goal of this research program is to produce long-lived Rydberg triplet-state Ps for precision radio-frequency (RF) spectroscopy of the fine structure of high- $n$  states. Figure 1.1 depicts the entire experimental system excluding the extensive electronics and laser systems. A broad-energy moderated  $e^+$  beam from the radioactive source is magnetically guided through a  $30^\circ$  bend towards the buffer-gas accumulator. The  $e^+$  are trapped and cooled within a strong magnetic field and electrostatic trapping well via inelastic collisions with nitrogen molecules and sulfur-hexafluoride, resulting in  $e^+$  with a much lower energy distribution. The cooled  $e^+$  are extracted from the trap and are magnetically guided through a  $90^\circ$  bend towards the Ps apparatus. In the Ps apparatus, a thermal oven emits ground-state Cs atoms that are laser-excited to produce a  $\text{Cs}^*$  gas target. The  $e^+$  are guided and slowed at the  $\text{Cs}^*$  target and charge-exchange to produce  $\text{Ps}^*$ , where a fraction of the  $\text{Ps}^*$  are guided for detection and spectroscopy. A depiction of this interaction is shown in Figure 1.2. Experiments involving the triplet states of  $\text{Ps}^*$  will be the focus, where the lifetimes are much longer than the singlet states. The goal is to produce triplet  $\text{Ps}^*$  in the  $11^3\text{S}_1$  state and drive transitions to the P states. The lifetime of the  $11^3\text{S}_1$  state is  $0.50\ \mu\text{s}$  whereas the  $11^3\text{P}_j$  states have a lifetime of  $5.23\ \mu\text{s}$ . An apparatus and technique have been developed to selectively filter out states and to drive RF transitions between the S and P states.

The following sections show theoretical calculations of Cs and Ps energy levels to find resonant states optimal for charge-exchange.

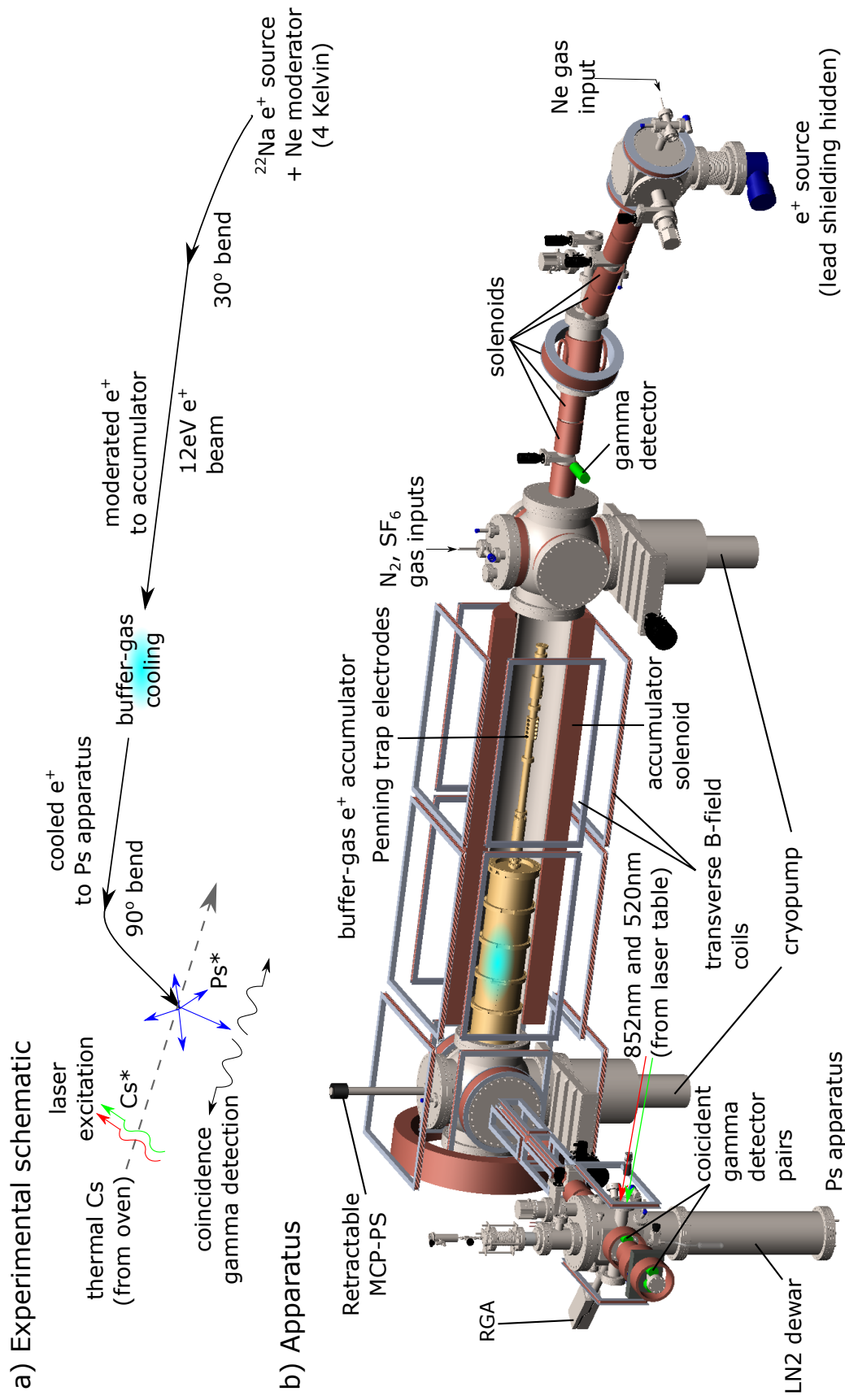


FIGURE 1.1: An overview of the entire e<sup>+</sup> beamline and vacuum system. a) A simplified schematic of the experimental sequence b) The current experimental apparatus. RGA: residual gas analyzer, MCP-PS: microchannel plate-phosphor screen.

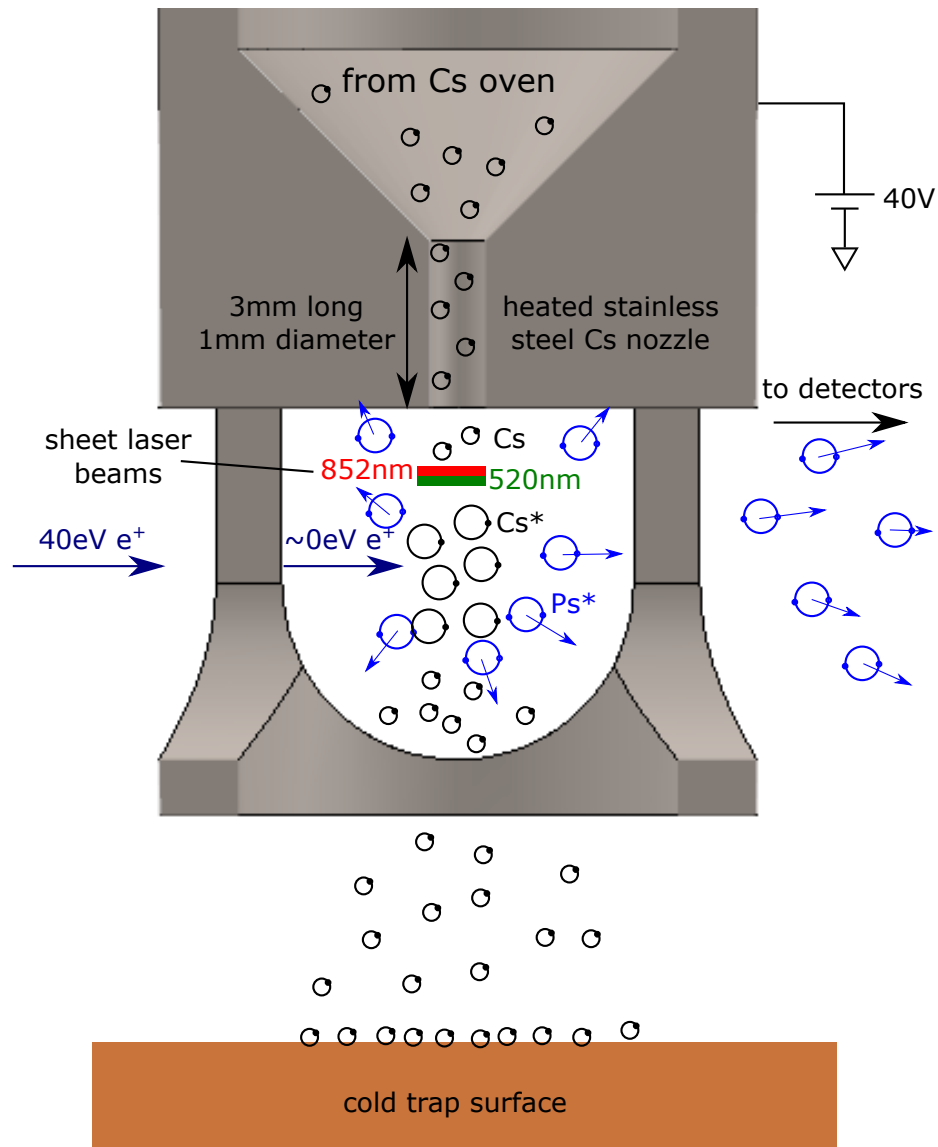


FIGURE 1.2: A representation of the beam of slow  $e^+$  charge-exchanging with  $\text{Cs}^*$  to produce  $\text{Ps}^*$ . The  $e^+$  exit the accumulator with 40 eV and enter from the left. The ground state  $\text{Cs}$  atoms are emitted downwards from the heated nozzle (cross-section shown) and are laser-excited to the Rydberg state. The lasers (out of the page) are overlapped and focused to a sheet. The  $\text{Ps}^*$  atoms are produced isotropically, with a fraction directed towards the detectors. The  $\text{Cs}$  atoms are collected on a cryogenically-cooled surface (distance to surface not to scale).

## 1.4 Energy Level Structure of Positronium and Cesium

The gross structure of Ps is similar in many ways to hydrogen. To first order, the non-relativistic energy levels are given by

$$E_n = -\frac{\alpha^2 \mu c^2}{2n^2} \quad (1.5)$$

where  $\mu$  is the reduced mass of the two-body system,  $c$  is the speed of light,  $\alpha$  is the fine structure constant and  $n$  is the principal quantum number. For hydrogen, the reduced mass is effectively the  $e^-$  mass,  $m_e$ , due to the proton having a mass that is approximately  $1836m_e$ . The reduced mass for Ps is exactly  $m_e/2$  since the  $e^+$  and  $e^-$  have equal masses. The reduced mass of Ps results in several intrinsic properties that are reduced by a factor of 2 compared to hydrogen. The first-order non-relativistic energy of Ps is approximately

$$E_n = -\frac{13.6 \text{ eV}}{2n^2} = -\frac{6.8 \text{ eV}}{n^2} \quad (1.6)$$

Higher-order terms can be calculated using the two-body relativistic Bethe-Salpeter equations [40]. The energies of triplet-state Ps including fine-structure and hyper-fine structure corrections are given by

$$E_{n,l,j} = -\frac{\alpha^2 mc^2}{4n^2} + \frac{\alpha^4 mc^2}{4n^3} \left[ \frac{11}{64n} + \frac{1}{2(2l+1)} + \frac{7}{12} \delta_{0l} + \epsilon_{l,j} \right] \quad (1.7)$$

where

$$\epsilon_{l,j} = \frac{(1 - \delta_{0l})}{8(l + \frac{1}{2})} \begin{cases} \frac{3l+4}{(l+1)(2l+3)}, & j = l + 1 \\ -\frac{1}{l(l+1)}, & j = l \\ -\frac{3l-1}{l(2l-1)}, & j = l - 1 \end{cases} \quad (1.8)$$

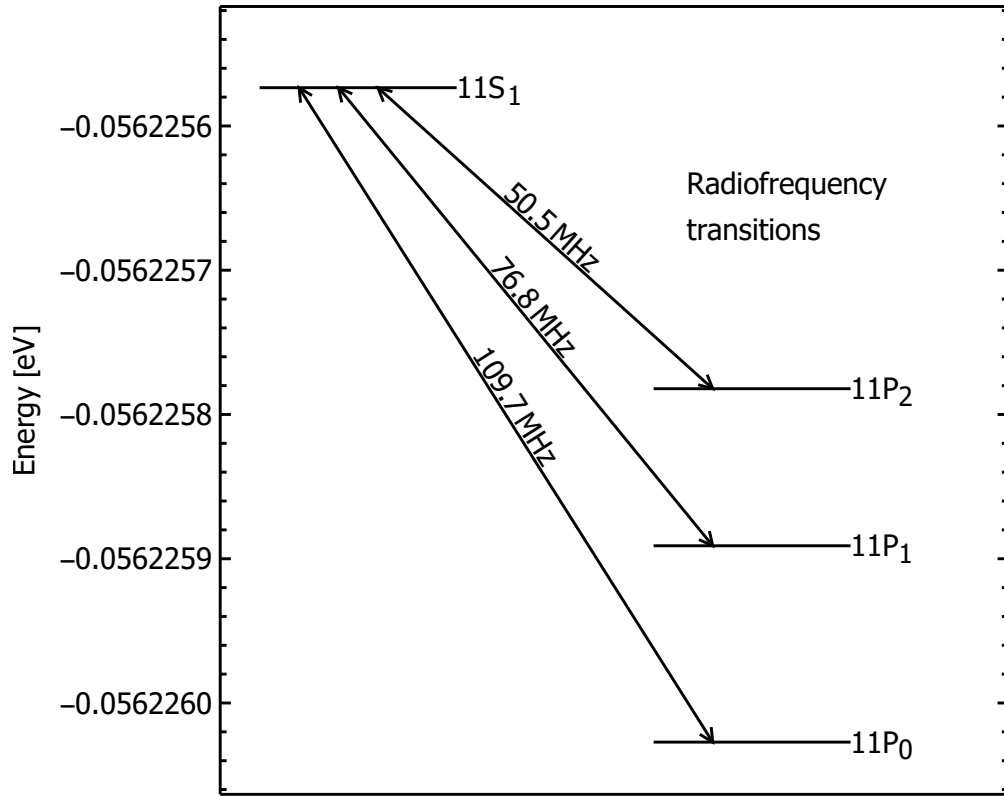


FIGURE 1.3: The  $n = 11$  triplet-Ps S-to-P transitions. The apparatus is developed for a precise measurement of the three S-to-P $_j$  transition frequencies.

The state is specified by  $l$ , the orbital angular momentum quantum number, and  $j$ , the total angular momentum. The term  $\epsilon_{l,j}$  is a correction term provided in the reference [41]. The hyperfine structure of Ps is not suppressed by  $m/M \approx 1/1836$  as in hydrogen, resulting in the hyperfine splittings that are on the same order as the fine structure splittings. The splittings for the  $n = 11$  S and P triplet states are shown in Figure 1.3. The theoretical transition frequencies from the  $11^3S_1$  state to the  $11^3P_0$ ,  $11^3P_1$ ,  $11^3P_2$  states are 109.685(8) MHz, 76.779(8) MHz, and 50.455(8) MHz respectively. An experimental uncertainty on the scale of 50 kHz would provide a competitive measurement relative to the  $n = 2$  fine-structure interval measurements.

Cs is an atomic system with a single valence  $e^-$ , with a nuclear structure more

complex than hydrogen. The nonrelativistic approximations of the energy levels differ from hydrogen by the inclusion of quantum defect correction terms. The quantum defect accounts for the modified electric potential observed by the valence  $e^-$  due to the core electrons. The energy levels of Cs for  $n \gtrsim 5$  are given by

$$E_n = E_\infty - \frac{\alpha mc^2}{2(n - \delta_n)^2} \quad (1.9)$$

where  $E_\infty$  is the binding energy of the ground state and  $\delta_n$  is the quantum defect for a state with principal quantum number  $n$ . The quantum defect has the form

$$\delta_n = A + \frac{B}{(n - A)^2} + \frac{C}{(n - A)^4} + \dots \quad (1.10)$$

where these terms have been accurately determined for Cs for a range of  $nL_j$  states for terms  $A$  to  $F$  [42].

### 1.4.1 States of Cesium and Positronium for Resonant Charge-Exchange

The Cs atoms are laser excited to the Rydberg state by a two-step laser transition. The first excitation drives the  $6S_{1/2}$ -to- $6P_{3/2}$  transition with a photon of 852 nm. From the  $6P_{3/2}$  state, either an  $nS_{1/2}$  or  $nD_{3/2,5/2}$  state can be excited. The  $nD_{5/2}$  state is chosen since the electric dipole moment is larger, therefore requiring a lower laser intensity to saturate the transition. Oscillator strengths for Cs transitions have been computed [43], where the ratio of the electric dipole moments are related to the oscillator strengths,  $f$ , by

$$\frac{\langle 6P_{3/2} | \vec{r} | nD_{5/2} \rangle}{\langle 6P_{3/2} | \vec{r} | nD_{3/2} \rangle} = \sqrt{\frac{f(6P_{3/2} \rightarrow nD_{5/2})}{f(6P_{3/2} \rightarrow nD_{3/2})}} \approx 3 \quad (1.11)$$

$$\frac{\langle 6P_{3/2} | \vec{r} | nD_{5/2} \rangle}{\langle 6P_{3/2} | \vec{r} | nS_{1/2} \rangle} = \sqrt{\frac{f(6P_{3/2} \rightarrow nD_{5/2})}{f(6P_{3/2} \rightarrow nS_{1/2})}} \approx 1.3 \quad (1.12)$$

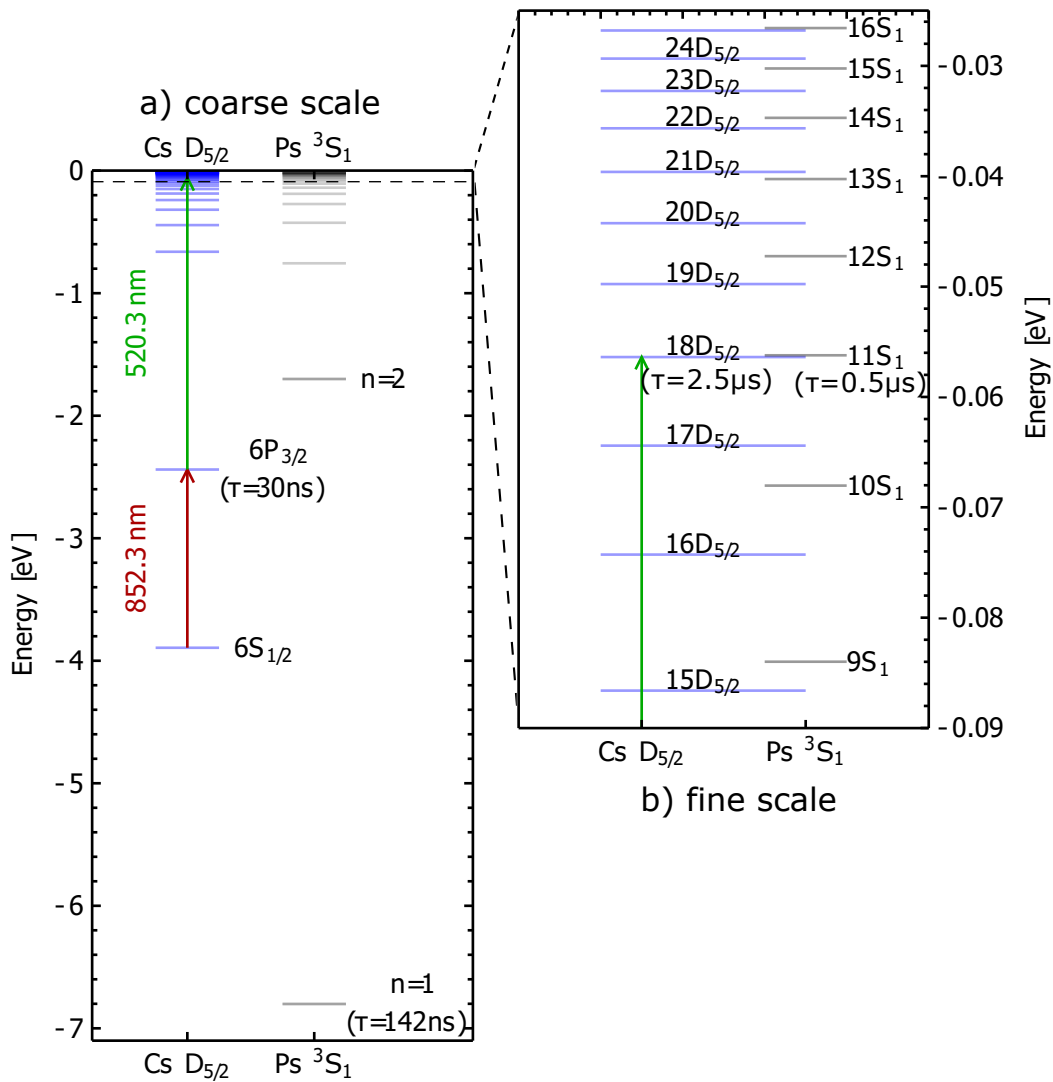


FIGURE 1.4: A comparison of Cs  $nD_{5/2}$  and Ps  $n^3S_1$  energy levels. a) The full energy scale showing the two-step laser transition in Cs. b) A finer scale view of the closely-spaced Rydberg states. The Cs states extend over to the Ps states to visualize the resonant states.

Figure 1.4 plots the energy levels of Cs  $nD_{5/2}$  and Ps  $n^3S_1$  states to compare states that are resonant and optimal for charge-exchange.

For  $n_{Cs} = 15 - 24$ , it can be seen that Cs  $18D_{5/2}$  is most resonant with Ps  $11^3S_1$ , where a 520.3nm photon is required to drive the transition. Classical trajectory Monte-Carlo calculations (CTMC) simulations have shown that Ps is mostly populated in the resonant state and neighbouring  $n_{Ps} \pm 1$  states [37].

Several properties can be calculated with the choice of these states. The lifetime of

the Cs  $6P_{3/2}$  state is about 30.5 ns and the typical thermal speed is about 250 m/s. An atom excited in this state travels approximately 8  $\mu\text{m}$  before radiatively decaying to the ground state. The excitation to the Rydberg state must occur before it decays, therefore an overlap of the 852 nm and 520 nm laser beams ensures that the second excitation can occur.

The lifetime of Rydberg states follow an  $n^3$  scaling law. For a Cs D state, the quantum defect to first order is  $\delta_D = 2.466\,315\,24(63)$  [42]. The resulting lifetime scales as

$$\tau_{nD} = (0.67 \text{ ns})(n - \delta_D)^3 \quad (1.13)$$

For Cs  $18D_{5/2}$ , the lifetime is approximately 2.5  $\mu\text{s}$ , which is 82 times longer than the  $6P_{3/2}$  state.

The downward directed Cs beam is emitted from a 3 mm long, 1 mm diameter tube (see Figure 1.2). The details of the Cs oven is discussed in Section 5.2. At thermal speeds ( $\sim 250$  m/s), the laser-excited Cs\* atoms traverse a distance of approximately 0.6 mm before decaying, setting the height of the Cs\* target. The  $e^+$  that are within this target can charge-exchange.

## 1.5 Estimates for Charge-Exchange

For unit charge-exchange efficiency where the  $e^+$  has a single chance to traverse the Cs\* target, the following condition must be satisfied:

$$\rho\sigma l = 1 \quad (1.14)$$

The parameter  $\rho$  is the Cs\* density,  $\sigma$  is the charge-exchange cross section, and  $l \approx 1$  mm is the Cs\* target thickness.

The predicted cross-section from CTMC calculations [37] is

$$\sigma = 9.7n_{Cs^*}^4\pi a_0^2 \quad (1.15)$$

The required Cs\* density for unit efficiency in an  $n_{Cs}$  state is therefore

$$\rho^* = \frac{1}{\sigma l} = 10^{11} \text{ Cs}^*/\text{cm}^3 \quad (1.16)$$

The Cs\* beam enters a target volume that has a  $d = 1$  mm diameter with a speed  $v = 250$  m/s. The rate  $R^*$  that enters this volume is

$$R^* = 0.25\rho^*\pi d^2v = 2 \times 10^{16} \text{ Cs}^*/\text{s} \quad (1.17)$$

Estimating a 30% laser excitation efficiency (9/16 ground states in a weak magnetic field, 50% of these can go to the Rydberg state) to the Rydberg state, the ground state rate of Cs emitted from the oven is approximately

$$R = \frac{1}{0.3}R^* = 7 \times 10^{16} \text{ Cs}^*/\text{s} \quad (1.18)$$

This rate of Cs atoms is achievable at an oven temperature of approximately 500 K. To date, the highest temperature that the oven has been operated was 400 K for a cautious and systematic approach to produce Ps\* with a low rate of Cs atoms. At this temperature, experiments were conducted at a reduced charge-exchange efficiency to extend the usage time of the liquid Cs reservoir in the oven and to monitor any degradation of the  $e^+$  systems due to Cs.

# Chapter 2

## Positron System

This chapter discusses aspects of the  $e^+$  system used to produce slow  $e^+$  for charge-exchange. A radioactive  $^{22}\text{Na}$  source emits high-energy  $e^+$  and is mounted on a 4K-cold system. A solid neon crystal moderates high-energy  $e^+$  to thermal speeds that can be efficiently captured in a buffer-gas accumulator. Buffer-gas accumulators can store large numbers of  $e^+$  with a narrow energy distribution and produce dense plasmas.

### 2.1 Positron Detection System

The detection of the single  $e^+$  and plasmas of  $e^+$  is accomplished with a variety of detectors and techniques. In one technique, the  $e^+$  are annihilated and the emitted gamma rays are detected. The key signature of a  $e^+$  is the annihilation into two back-to-back gamma rays that have a photon energy of 511 keV each. Photodetectors are capable of resolving the energy of the photons with precise timing. The  $e^+$  also carries a charge that can be detected with charge-integration methods for large numbers of  $e^+$  deposited on a Faraday cup. A Faraday cup is typically used to detect intense charged particle beams such as  $e^-$  and ion beams, however for the low-density moderated  $e^+$  beam, it generates a current that is insufficient for a typical detection on the scale of nano-Ampere. The radial profile

of the  $e^+$  is also measured by depositing the beam onto an imaging system where the light output is collected on a camera. A detailed description of each of these detector systems is given below.

### 2.1.1 Gamma Detectors

For the detection of  $e^+$  annihilations from Ps or from impact on surfaces, high-energy photons are detected with scintillating crystals coupled to photodetectors. A high-energy photon interacts with the  $e^-$  and molecules within the scintillator, and the scintillator outputs lower-energy, visible photons. The amount of visible scintillation light emitted is proportional to the energy of the high-energy photon absorbed. The light output is coupled into a photodetector to amplify and convert the output to an electrical signal. This signal is recorded and analyzed by a variety of electronics and software.

Scintillators can be composed of several organic and inorganic compounds. The ideal type of material produces the largest amount of visible photons per high-energy photon. Other factors that must be considered are the material density, the rise and decay times, and the output wavelength spectrum and efficiency. Gamma radiation is efficiently detected in dense, high- $Z$  inorganic scintillators, where  $Z$  is the atomic number. The photon is absorbed in the material by the photoelectric effect, Compton scattering, or by pair production. The photoelectric effect is the dominant process for a 511 keV photon, where an  $e^-$  in the scintillator absorbs the entire photon energy. Compton scattering occurs when the high-energy photon partially transfers energy to an  $e^-$ . For both effects, the  $e^-$  loses kinetic energy through inelastic collisions that excite the scintillator molecules and emit the visible photons. A scintillator with a fast rise-time is critical for coincidence detection applications such as the back-to-back gammas produced from  $e^+$  annihilations. The decay time of the scintillation pulse limits the amount of time between events that can be resolved. The output wavelength spectrum of the scintillator is matched with a photodetector with a response similar to the spectrum. A table of commonly used inorganic scintillators and their properties are shown in Table 2.1.

Scintillator	Yield (photons/keV)	Density (g/cm <sup>3</sup> )	Decay time (ns)	Max wavelength (nm)
NaI(Tl)	43	3.67	230	415
BGO	8.2	7.13	300	480
LYSO	32	7.1	41	420
CsI(Tl)	54–61	4.51	600	550

TABLE 2.1: A brief table of common inorganic scintillators and their properties [44]. For this experiment, NaI(Tl) scintillators are used for its low cost and relatively high photon yield.

The scintillators used for this experiment are NaI(Tl) crystals (St. Gobain 2R2) with a 5.08 cm diameter and 5.08 cm length. The crystal is hermetically sealed within a thin aluminum housing to permit gamma rays to enter, and with an optical window to transmit the down-converted photons to the photodetector. A white Teflon paste between the crystal and aluminum housing provides a cushion and a highly reflective surface, resulting in an increased amount of light detected.

The scintillators are coupled to either a photomultiplier tube (PMT) or a silicon photomultiplier (SiPM) to provide an approximate amplification of  $10^6$  and converts the light signal to an electrical signal. The PMT is an evacuated tube with a photocathode and a series of dynodes. The scintillation photons incident on the photocathode results in  $e^-$  ejected via the photoelectric effect. The  $e^-$  are attracted to a dynode and gain  $\sim 100$  eV of kinetic energy. Upon impact with the dynode, a large amount of  $e^-$  are ejected and are attracted towards the next dynode. This chain-reaction process is repeated for several dynodes and provides an amplification of the  $e^-$  count of approximately  $10^6$ . The  $e^-$  after this amplification are collected on an anode and results in a measureable current pulse for detection. The centimeter-scale distances that the  $e^-$  traverses between dynodes causes PMTs to be highly susceptible to magnetic fields.

The SiPM is a solid-state device that is a modern alternative to the PMT. The SiPM is insensitive to magnetic fields since it is composed of silicon semiconductors with no free-space distance for  $e^-$  to traverse. To operate the detector, it only requires a low-voltage reverse bias as opposed to high-voltages. The size of SiPMs is also much smaller than PMTs, resulting in a more compact detector. The sensor

(SensL ArrayJ-30035-64P-PCB) contains an  $8 \times 8$  array of  $3 \text{ mm} \times 3 \text{ mm}$  single-photon avalanche diodes (SPAD) with individual quench resistors. The reverse bias is set above the nominal breakdown voltage creating a large electric field across the  $p - n$  junction. A photon creates an  $e^-$ -hole pair in the depletion region that triggers an avalanche of secondary  $e^-$ -hole pairs, causing a breakdown and flow of a measurable current pulse. The breakdown is halted by the flow of current across a quench resistor which reduces the net voltage across the junction below the breakdown voltage. A printed circuit board (PCB) attached to the sensor sums the signal of all 64 SPADs to a single output for detection. This detector provides 30% coverage of the scintillator optical window.

#### 2.1.1.1 Photon Counting

With these detectors, single gamma rays and coincident gamma rays can be detected from events such as  $e^+$  annihilation or cosmic background radiation. A flow diagram of both single and coincidence measurements is shown in Figure 2.1. To measure the rate of gamma rays emitted, an electronics system has been developed that implements an amplifier (LeCroy 612AM), discriminator (LeCroy 4608C), inverter (TC 212), and a ratemeter (Ortec 441). After amplification, if the signal exceeds a threshold set by the discriminator, a 60 ns negative square-pulse logic signal is outputted that is then inverted and sent to the ratemeter. The ratemeter produces a voltage output proportional to the count rate, and this is recorded on a data logger (Keithley 2701).

For coincidence-counting, the timing between the leading edge of the discriminator outputs from two detectors must be compared. This is nearly identical to the single-event counting system, with a coincidence detection module (LeCroy 465) and a logic module (LeCroy 365AL) inserted between the discriminator and inverter. The coincidence module compares the overlap timing of the two 60 ns pulses with a minimum resolving time of 1.1 ns. At the end of the overlap, the module generates a 100 ns square pulse that is outputted to a logic module. The coincidence module analyzes coincidences for two separate detector pairs and has

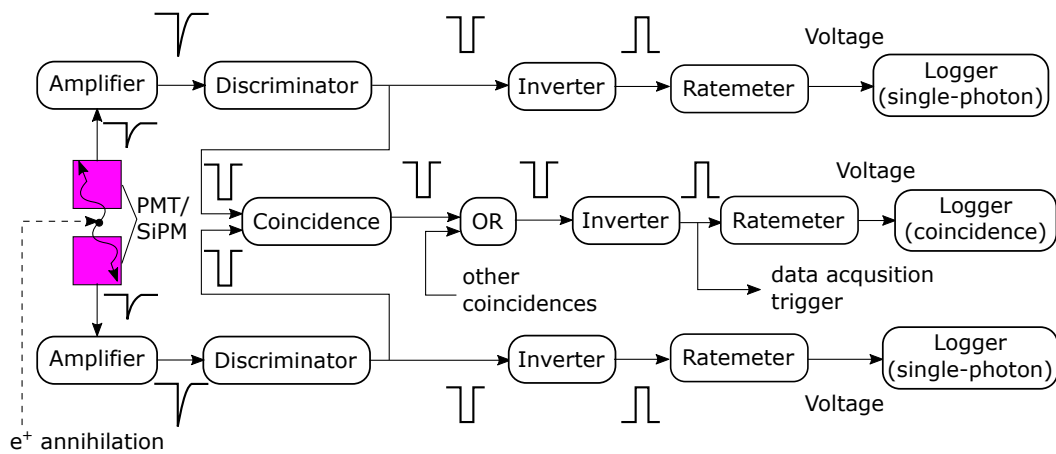


FIGURE 2.1: A schematic for single (top + bottom row) and coincidence detection (middle row) of gamma rays using two photodetectors. A raw photodetector signal pulse is amplified and discriminated against a threshold to produce a square-pulse logic signal. For a coincidence measurement between two detectors, the timing of the square-pulse leading edges are compared, and a square pulse is outputted if the time separation is below a set timing threshold. The square-pulse signals are inputted to ratemeters for rate measurements.

individual outputs for each pair. The two outputs are sent to a logic module with an OR gate which will produce a negative square-pulse logic signal if either detector pair detects a coincidence. This pulse is then inverted and is sent to a ratemeter for a coincidence rate measurement and also sent to the data acquisition system as a trigger (discussed in Section 5.8). For the data acquisition system, the raw signals are post-analyzed to ensure a strict-timing between leading edges. The coincidence module can toggle on/off channels to switch between single event detection of either detector or for coincidence detection. Coincidence detection is a powerful tool for searching for localized  $e^+$  annihilation events and reducing background events from cosmic rays and uncorrelated  $e^+$  annihilations.

The buffer-gas accumulator releases pulsed  $e^+$  beams that contain large numbers of  $e^+$  that are annihilated within a time much shorter than the decay time of the NaI(Tl) scintillator. This generates large amounts of 511 keV gamma rays that cannot be individually resolved by the photodetectors and are detected as if it originated from a single photon that possessed many multiples of 511 keV in energy (also known as pileup). The photodetector becomes saturated when the

current pulse output amplitude becomes nonlinear with respect to the amount of incident gamma rays.

Depending on the type of experiment conducted, this must be taken into consideration. For the current experiment, the goal is to detect  $\text{Ps}^*$  production on an event-by-event basis without any pileup signals, which can be achieved with low density  $e^+$  beams. For future  $\text{Ps}^*$  production experiments using pulsed  $e^+$  beams, the annihilation of  $e^+$  around the target region can be used as a prompt timing reference.  $\text{Ps}^*$  produced from the pulsed  $e^+$  beam can travel a distance before decaying, which can be observed as a delayed annihilation signal from the prompt.

### 2.1.2 Faraday Cups

For pulsed  $e^+$  beams, the total number of  $e^+$  can be measured on a Faraday cup using charge-integration. A Faraday cup is a conductive surface that charged particles can be deposited on to detect the number of charges. A  $e^+$  that is deposited on the Faraday cup annihilates a surface  $e^-$ , and what is detected is the  $e^-$  deficit. Faraday cups are connected to charge-sensitive preamplifiers (Cremat CRZ110/111) that output a voltage proportional to the charge deposited. The simplified picture is that the charge,  $Q$ , deposited onto the Faraday cup is coupled to a capacitor, with capacitance  $C$ , so that the voltage across the capacitor is

$$V = \frac{Q}{C} \quad (2.1)$$

The preamplifier is based on a charge-integrating op-amp circuit that dissipates the charge deposited on the capacitor over a timescale determined by the circuit time constant. The CRZ110 model contains a 1.4 pF capacitor and 100 M $\Omega$  resistance, where up to  $1.3 \times 10^7$   $e^+$  can be detected per pulse due to the circuit's voltage output limitation. The output of the preamplifier is a pulse with a short 7 ns rise time, and a decay time of  $\tau = RC = 140$   $\mu\text{s}$ . The CRZ111 model contains a 15 pF capacitor and 10 M $\Omega$  resistor, where up to  $1.3 \times 10^8$   $e^+$  per pulse can be detected. The output of the preamplifier is 50  $\Omega$  terminated at the oscilloscope,

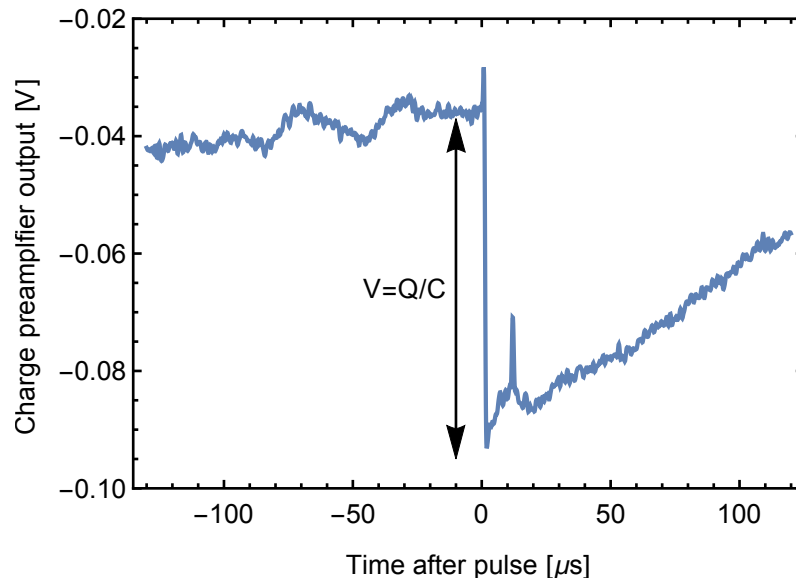


FIGURE 2.2: The output of the charge preamplifier from a pulse of  $e^+$ . The amplitude of the signal is used to calculate the number of  $e^+$  in the pulse. The decay time is determined by the  $RC$  time constant.

and a typical trace is shown in Figure 2.2. The oscilloscope is triggered by the pulse that ejects the  $e^+$  plasma from the trap. The  $e^+$  are given 40 eV of kinetic energy and traverses a 1 m distance to the Faraday cup, resulting in a 0.3  $\mu\text{s}$  transit time. This time delay is negligible on the time scale shown in the figure.

A  $e^+$  with kinetic energy greater than the work function of the Faraday cup material can eject an  $e^-$ , and then annihilate a surface  $e^-$  which results in over-counting. The Faraday cups are biased by 9 V through the preamplifier to inhibit  $e^-$  ejection from the surface [45].

### 2.1.3 Plasma Imaging

The imaging system consists of a microchannel plate (MCP) and a phosphor screen mounted on a vertical translation stage. A schematic of the imaging system is shown in Figure 2.3. The MCP (Del Mar Photonics MCP-MA25) is a 2.54 cm diameter, 0.5 mm thin glass plate that contains millions of secondary  $e^-$  multiplier channels, where each channel diameter is typically 10  $\mu\text{m}$  to 15  $\mu\text{m}$ . The channels are coated with a resistive semiconducting film. A high-energy particle or photon

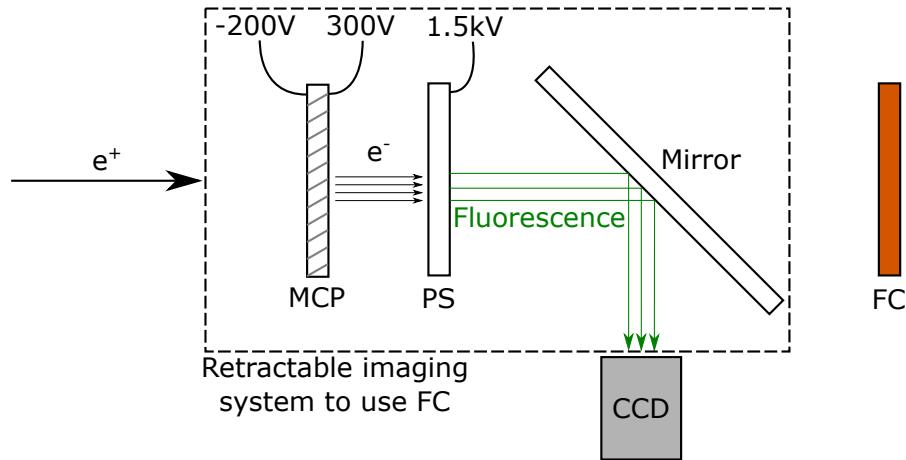


FIGURE 2.3: A schematic of the plasma-imaging system mounted on motorized translation stage (dashed region). The phosphor screen light output is reflected by a  $45^\circ$  mirror through a glass viewport into a CCD. The imaging system can be translated out of position to use the Faraday cup. MCP: Micro-channel plate, PS: phosphor screen, FC: Faraday cup.

that impacts a channel causes an ejection of secondary  $e^-$ . By applying a bias across the channel, the secondary  $e^-$  are accelerated by the electric field and collide with the surfaces multiple times, amplifying number of  $e^-$ . A metallic coating is deposited on the front and back of the glass surface that provides electrical contact to the semiconductor layer in each channel. The bias between the front and back face is typically 200 V–1000 V, where a  $10^4$ – $10^6$  gain can be expected.

The  $e^+$  energy is determined from  $U = e\Delta V$ , where  $\Delta V$  is the potential difference between the  $e^+$  emission location and a reference  $e^+$  location. The  $e^+$  are released from a 10 V to 40 V reference and are magnetically guided to the MCP front surface that is biased to  $-200$  V, resulting in  $>200$  eV  $e^+$  kinetic energy upon impact. The spatial profile of the incident  $e^+$  beam on the MCP channels results in  $e^-$  ejected from the MCP back surface with an identical spatial profile. The ejected  $e^-$  are accelerated across a 1.5 kV electric potential over a 1.6 cm distance towards a 2.54 cm diameter phosphor screen for imaging. The strong electric field accelerates the  $e^-$  along a straight-line path to the phosphor screen that preserves the spatial profile, otherwise a weak electric field can lead to a diverging  $e^-$  beam that distorts the original spatial profile. The  $e^-$  excite the phosphor atoms and the fluorescence is reflected by a mirror and can be viewed through a

vacuum chamber viewport. A CCD camera (Basler acA640-300gm) mounted to the viewport images the phosphor screen. The CCD is used for a continuous live image of the moderated beam. To image the pulsed  $e^+$  plasma ejected from the trap, the camera is triggered with a 100 ms exposure time just prior to the  $e^+$  arriving to the MCP.

The imaging system (dashed box within the figure) is mounted on a motorized vertical translation stage that can be retracted for  $e^+$  detection on a Faraday cup, and to magnetically guide  $e^+$  to the Ps apparatus. The system is remotely controlled such that studies involving plasma-imaging and Faraday cup measurements can be completely automated.

## 2.2 $^{22}\text{Na}$ Source

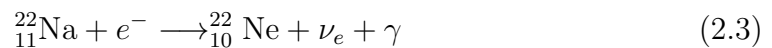
The  $e^+$  source is a sealed titanium capsule containing radioactive  $^{22}\text{Na}$ . The half-life of  $^{22}\text{Na}$  is 2.602 years where it can beta decay to emit  $e^+$  (90.57% probability) or emit high energy gamma rays via  $e^-$  capture (9.43% probability).

The beta decay process can be represented with the reaction



where the  $e^+$  is emitted with up to 546 keV of kinetic energy and  $^{22}_{11}\text{Na}$  decays to an excited state of  $^{22}_{10}\text{Ne}$ . The radiative decay to the  $^{22}_{10}\text{Ne}$  ground state emits a 1275 keV gamma ray.

The  $e^-$  capture process can be represented by



Both processes decay to a stable isotope of Neon-22.

The source is produced by iThemba LABS in South Africa, currently the sole supplier in the world. The source capsule is filled with a drop of  $^{22}\text{Na}$  solution that is evaporated until the salt remains. The salt is deposited on a tantalum cup, which is a high- $Z$  material that is efficient for  $e^+$  reflection [46]. The front end is sealed with a  $5\ \mu\text{m}$  thin titanium window where  $e^+$  can exit. The salt emits  $e^+$  in an isotropic distribution, where 50% are directed towards the window, an additional 25% are redirected to the window from reflecting from the tantalum surface, resulting in a net 75% forward-going  $e^+$  directed towards the window [47]. There is an additional 50% loss from the absorption and annihilation within the salt itself, and 33% of the incident  $e^+$  annihilate in the titanium window. Accounting for all factors, the source has a net efficiency of  $\sim 25\%$  to emit forward-going  $e^+$  through the window from each  $^{22}\text{Na}$  disintegration.

## 2.3 Positron Moderation

The  $e^+$  emitted from the radioactive source have kinetic energies up to 546 keV. To efficiently trap  $e^+$  in a buffer-gas accumulator, they must be moderated to low energies with an energy width on the order of 1 eV. It is at this scale where  $e^+$  can effectively lose energy to buffer-gas excitations, otherwise a competing mechanism that forms Ps dominates and leads to  $e^+$  losses. There are many types of moderators that slow  $e^+$  such as thin metal films (tungsten) and frozen rare-gas solid moderators (Ne, Ar, Xe, Kr)[48, 49]. Thin metal moderators, such as single-crystal tungsten result in much narrower energy distributions compared to rare-gas moderators, however the rare-gas moderators have higher efficiencies for slowing the  $e^+$  [28]. In a rare-gas moderator, the high-energy  $e^+$  lose kinetic energy to the creation of  $e^-$ -hole pairs, excitons, and Ps atoms [50]. Within an insulator, an  $e^-$  in the valence band can be excited to the conduction band, leaving behind a positively-charged hole. The hole can bind to an electron, and this quasi-particle is referred to as an exciton. When the  $e^+$  energy is reduced below the threshold for these processes, the  $e^+$  continue to lose energy by phonon excitations ( $\lesssim 10\ \text{meV}$  for rare-gases) within the rare-gas lattice structure. A phonon is a vibrational

quanta excited within the lattice structure that does not lead to  $e^+$  annihilation, such that the  $e^+$  can excite many phonons and lose energy as it diffuses towards the surface. The  $e^+$  can escape from the surface if it has more energy than the  $e^+$  work function,  $\sim 2$  eV for the rare-gases mentioned. The most commonly used moderator is a solid neon rare-gas moderator. The moderator consists of a thin layer of solid neon frozen onto a conical copper surface at the exit of the  $e^+$  source capsule window. The conical copper surface will be referred to as the cone. The neon moderator with the conical geometry has an efficiency of  $\sim 0.5\%$ , more than 20 times more efficient than thin-metal tungsten moderators [51].

The source and cone are cooled to 8 K by a cryogenic refrigerator–cold head (Sumitomo RDK 408D2). The cold head consists of two stages that are cooled by the expansion of compressed helium from a closed-cycle system. A  $\sim 77$  K copper cylindrical shell is connected to the first stage of the cold head. It surrounds the source and cone to minimize the heat load from blackbody radiation from the room-temperature vacuum chamber walls. A sapphire disk is sandwiched between the source assembly and second stage to electrically isolate it from the cold head, such that a voltage bias can be applied to the source to tune the kinetic energy of moderated  $e^+$ . To maximize the thermal contact across the sapphire isolator, a thin layer of indium is sandwiched between the surfaces. A schematic of the source assembly is shown on the inset of Figure 2.4.

To grow a neon moderator, the source is cooled to 8 K and then gradually elevated from 8 K to 50 K by turning off the cold head. Neon gas flows into the vacuum chamber with the flow rate controlled by a mass flow controller (MKS Type 1179 Mass-Flo Controller). The moderator strength and lifetime can be optimized by studying the neon flow rate, neon flow time, and base temperature of the cone. The cone can be heated by a cartridge heater (Lakeshore HTR-50) mounted to the second stage that can provide up to 50 W of power. The cartridge heater is a resistive element composed of nickel lead wires insulated by magnesium oxide and is enclosed within a 6.2 mm diameter, 25.4 mm long iron/nickel/chromium alloy case. The vacuum chamber is pumped by a 77 L/s turbomolecular pump (Agilent

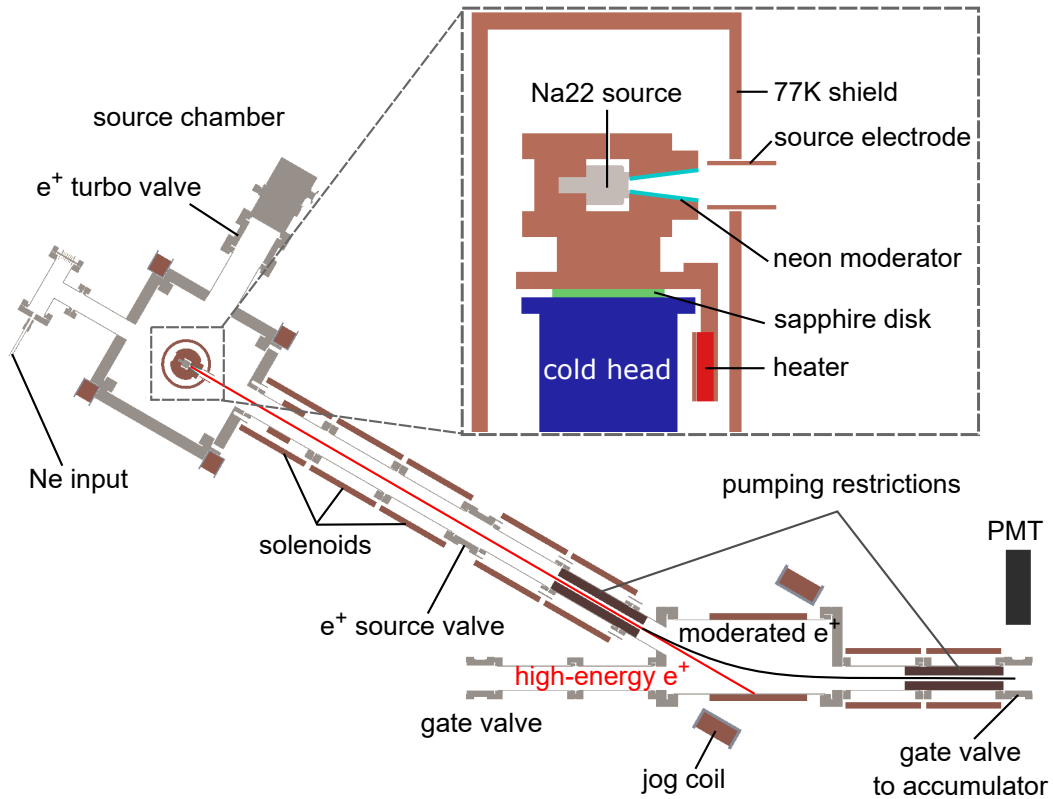


FIGURE 2.4: The trajectory of moderated  $e^+$  that are deflected through the jog chamber towards the buffer-gas accumulator. The unmoderated high energy  $e^+$  travel in a straight path and annihilate on a vacuum chamber wall. The inset is a diagram of the  $e^+$  source system.

Varian Twisstor FS84), which is backed by a scroll pump (Agilent Varian SH110). With the cold head at 8 K, the vacuum base pressure is  $4 \times 10^{-9}$  Torr.

The moderated  $e^+$  follow magnetic field lines ( $\sim 0.01$  T strength) and are guided through the “jog section” vacuum system while the unmoderated high-energy  $e^+$  are not guided and annihilate on the stainless steel vacuum chamber walls. The moderated  $e^+$  are magnetically guided towards a closed gate valve. A scintillator detector 13.5 cm away from the gate valve center detects annihilations and indicates the intensity of the moderated  $e^+$  beam.

The trajectory of the moderated  $e^+$  through the jog section and pumping restrictions is shown in Figure 2.4, where magnetic-field generating coils are indicated. An angled “jog coil” generates a magnetic field directed towards the offset hole, and a “jog vertical” provides a vertical magnetic field correction to maximize the rate (see Figure 2.5). Each coil used in this experimental system is current-controlled

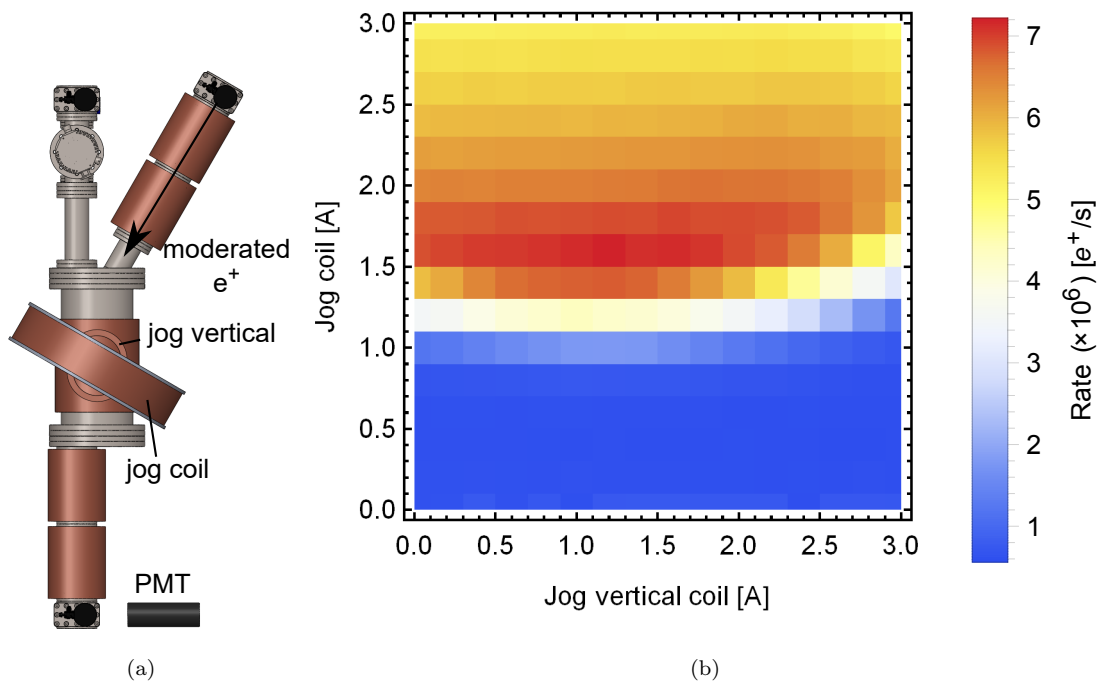


FIGURE 2.5: A heatmap scan of the overjog coil and jog vertical coil to maximize the PMT ratemeter signal at the input valve of the accumulator.

with the current monitored across a shunt resistor, and the voltage monitored across the leads. By measuring the voltage and current, this provides diagnostics of any faults in the coils such as electrical shorts, or resistance changes.

Two  $^{22}\text{Na}$  sources have been used during this work, where a stronger source replaced a weaker source. For the 7 mCi source, the maximum rate detected is  $1.68(1) \times 10^4$  cps, corresponding to  $1.9(4) \times 10^6 e^+/s$  when considering solid angle ( $\epsilon_\Omega = 0.009$ ) and detector efficiency factors. For the newer source at 28.5 mCi, the maximum rate detected is  $6.52(4) \times 10^4$  cps, which is  $7.23(14) \times 10^6 e^+/s$ . The dominant uncertainty in the conversion to a  $e^+$  rate is the determination of the detection efficiency of 50(10) % [52]. The solid-angle factor is based on the 5.08 cm diameter face of the detector distanced 13.5 cm from the gate valve center, and is given by

$$\begin{aligned}
\Omega &= \iint \sin \theta \, d\theta \, d\phi \\
&= 2\pi \left( 1 - \cos \left( \frac{2.54}{13.5} \right) \right) \\
&= 0.11 \text{ sr} \\
&= 4\pi(0.009) = 4\pi\epsilon_{\Omega}
\end{aligned}$$

A pumping restriction (20 cm long, 1.2 cm diameter) is placed at the entrance and exit of the jog chamber to isolate the buffer-gas accumulator and the source chamber. The jog section is pumped by a 67 L/s turbomolecular pump (Agilent Varian Twisstor FS84), which minimizes the amount of nitrogen that can flow from the buffer-gas accumulator towards the source. The operating pressure in this section is  $3 \times 10^{-9}$  Torr.

### 2.3.1 Moderator Growth

The gamma count rate is monitored during the moderator growth to optimize the growth parameters. An example of an optimized moderator growth is shown in Figure 2.6.

To begin a growth, the cold head cryostat and source heater cartridge are turned off to warm up the source and evaporate the existing neon moderator and other impurities. The “ $e^+$  source valve” between the source chamber and the jog chamber is shut. At 13 K, the neon moderator begins to evaporate from the source surfaces. The large neon gas load on the “source turbomolecular pump” is avoided by turning it off once the chamber pressure reaches 0.2 Torr and the system is pumped by the backing scroll pump. The source turbomolecular pump is turned back on once the chamber pressure is reduced down to 0.75 Torr. The system is warmed up to 50 K, and then the cryostat is turned back on to begin cooling.

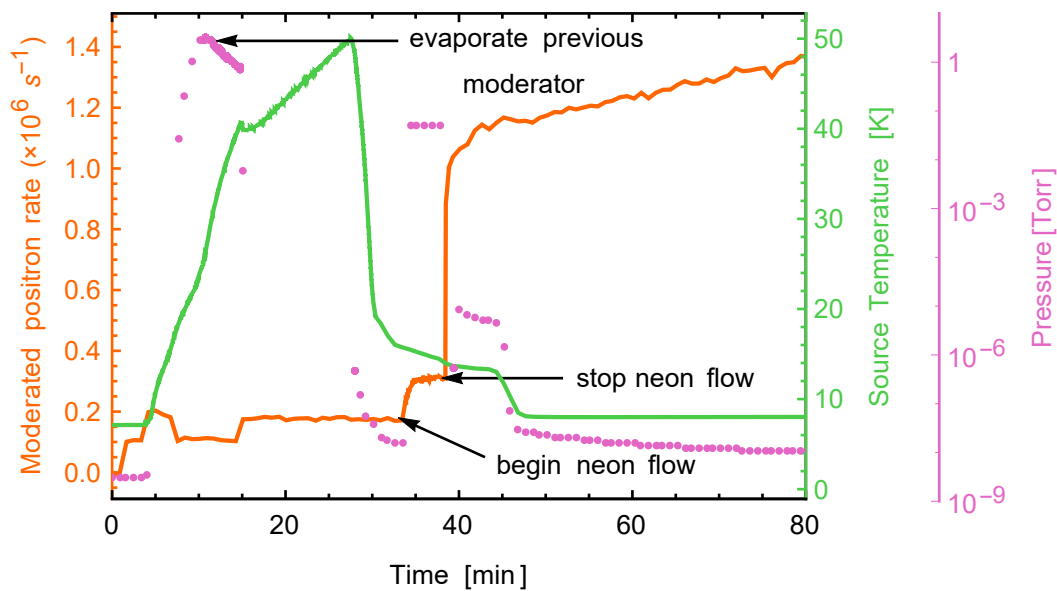


FIGURE 2.6: A plot of the source temperature, chamber pressure and moderated  $e^+$  rate during a neon moderator growth. From 8 K, the cryocooler is turned off and the source is warmed to 50 K to evaporate the current neon moderator and impurities. The cryocooler is then turned on and the neon growth occurs within a temperature range for a set amount of time. After the neon moderator has been grown, the neon flow is shut and the procedure is complete.

Upon reaching 20 K, the source cartridge heater is set to 4.2 W for 10 minutes to obtain an equilibrium temperature of 10.8 K on the cone. This heater setting has been found to give the largest rate of slow  $e^+$  as shown in Figure 2.7. This temperature is set just below the sublimation point to condense the neon gas onto the cone. The source turbomolecular pump is then valved shut, the source valve to the jog chamber is opened, and the system is actively pumped by the “jog turbomolecular pump” through the pumping restriction. Neon gas (99.999 % purity) flows into the source chamber at 120 standard cubic centimeters per minute (sccm) where the crystal growth begins. As the neon crystal thickness increases over time, the number of slow  $e^+$  emitted increases. A large fraction of the slow  $e^+$  annihilate on the neon gas, and a small fraction is magnetically guided to the annihilation gate valve where the gamma rate is monitored. The number of slow  $e^+$  emitted plateaus and the neon flow is shut after 4 minutes of growth. The valve to the source turbomolecular pump is opened and the remaining neon gas is quickly pumped out, leading to a large increase in detected  $e^+$  annihilations.

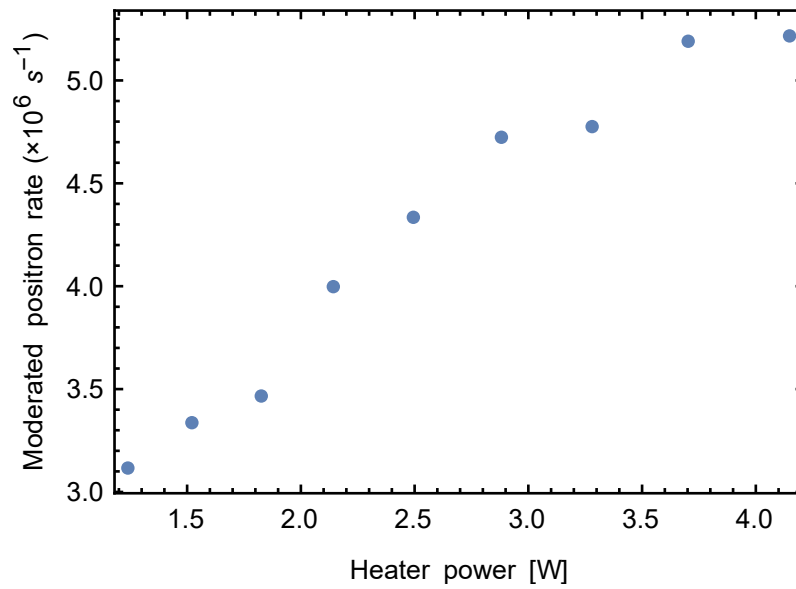


FIGURE 2.7: The rate of moderated  $e^+$  emitted from the moderator for different heater settings during the growth. This is the immediate rate after the growth is complete.

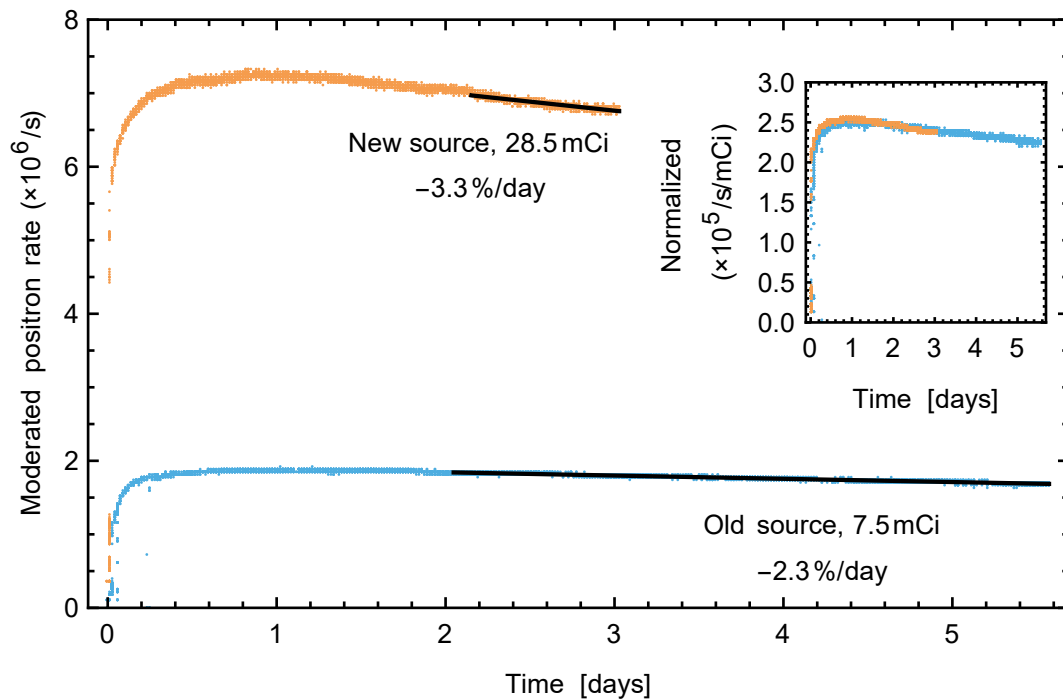


FIGURE 2.8: The decay of the neon moderator for both  $e^+$  sources. The inset shows the rate of moderated  $e^+$  normalized to the strength of  $e^+$  source, and it shows that the trend is nearly identical.

The source cartridge heater remains at 4.2 W for an additional 5 minutes, and then the power is reduced to 1.2 W to stabilize the source to 8 K. The decay of the moderator is shown in Figure 2.8, where the moderator decays at a rate of 2.3%/day for the older source at 7.5 mCi, and 3.3%/day for the newer source at 28.5 mCi. The moderator decay of the newer source improves with the vacuum condition over time, where it has only been under vacuum for a year compared to over 6 years for the older source. When normalized by the strength of the source, the decay curves are nearly equivalent (shown in the inset). The entire growth process takes  $\sim 45$  minutes to complete. The moderator is typically regrown once a week but has also been used for over a month.

### 2.3.2 Radial Profile of the Moderated $e^+$ Beam

The moderated  $e^+$  beam can be magnetically guided through the buffer-gas trap (discussed in Section 2.5) and imaged onto the plasma-imaging system. The MCP front surface is typically biased to  $-200$  V, the MCP back surface biased to 300 V, and the phosphor screen biased to 1.5 kV. An image of the moderated beam is shown in Figure 2.9.

The radial profile of the moderated beam shows a toroidal geometry, where the beam is most intense at a diameter of 2.29(1) mm. This profile is due to the  $e^+$  emitted from the neon moderator deposited on the source cone surface. The depleted center of the profile shows that there are little moderated  $e^+$  emitted from the window of the source capsule. The outermost edge of intensity is approximately at a diameter of 4.6(2) mm.

## 2.4 Penning Trap Theory

Charged particle traps are important tools to study the properties of a single charged particle and to store large numbers of charged particles. Examples include a precision measurement of the magnetic dipole moment of a single  $e^-$  in a

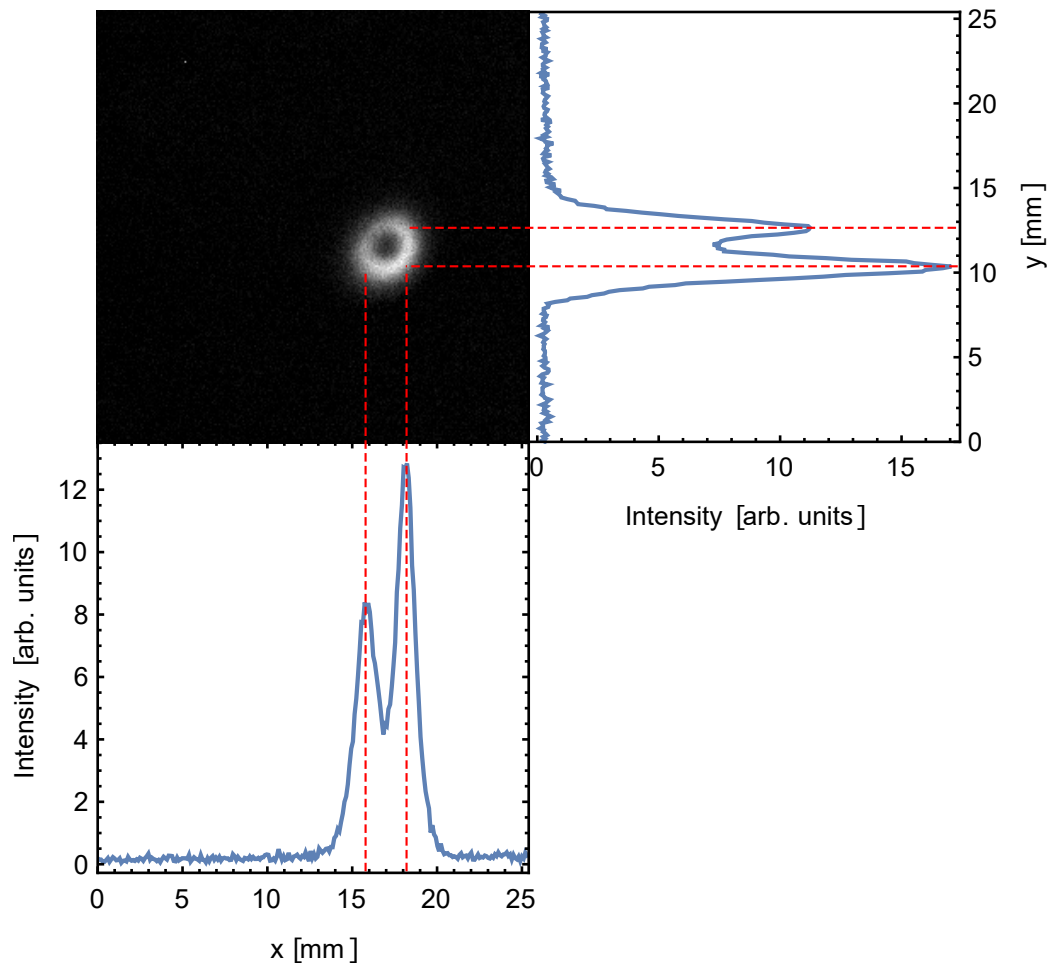


FIGURE 2.9: An image of the moderated  $e^+$  beam with a rate of  $6.5 \times 10^6 e^+/s$ . The toroidal profile represents the moderated  $e^+$  emitted from the conical copper surface of the source system. The X-Y profile is shown, where the pixels are calibrated to the 25.4 mm diameter of the phosphor screen.

cylindrical Penning trap has provided one of the most stringent tests of free-state QED [53]. Dense plasmas of  $e^+$  and anti-protons in nested Penning-Malmberg traps are used for antihydrogen synthesis to test charge, parity, and time-reversal (CPT) symmetry [54, 55].

A Penning trap employs a static magnetic field to radially confine a charged particle and an electrostatic quadrupole potential for axial confinement. The ideal Penning trap produces a harmonic electric potential via electrode geometries that are hyperboloids of revolution as shown in Figure 2.10. The electric potential generated by this geometry is

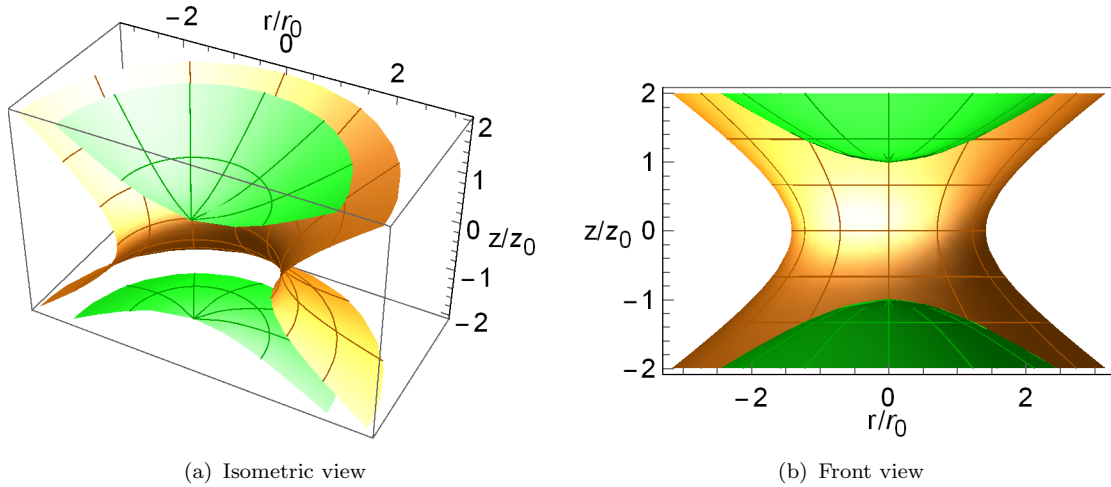


FIGURE 2.10: The electrodes for an ideal Penning trap. An electric quadrupole potential is generated by ring (orange) and end-cap (green) electrodes.

$$\phi(r, z) = \frac{V_0(2z^2 - r^2)}{r_0^2 + 2z_0^2} \quad (2.4)$$

where  $V_0$  is the applied voltage on the end-cap relative to the ring electrode. Along  $z$ , the electric potential is a harmonic well that is concave-up, thus providing axial confinement for a positively charged particle. Along  $r$ , the electric potential is harmonic and concave-down, which would radially eject a positively charged particle. To counteract this, a uniform magnetic field aligned with the  $z$ -axis provides an inwards force via the Lorentz force,  $\vec{F} = q\vec{v} \times \vec{B}$  for a charged particle of mass  $m$  and charge  $q$ . A charged particle in a magnetic field  $B$  undergoes cyclotron motion with a frequency

$$\omega_c = \frac{|qB|}{m} \quad (2.5)$$

The equations of motion within the fields of the ideal Penning trap lead to three distinct motions: the axial bounce, modified cyclotron orbit, and magnetron orbit. The axial motion from the confinement between the endcaps oscillates at a frequency

$$\omega_z = \frac{|qV_0|}{md^2} \quad (2.6)$$

where  $d = \sqrt{\frac{1}{2}(z_0^2 + r_0^2/2)}$  is the characteristic trap dimension. The magnetron motion is a radial orbit around the trap centre due to the  $\vec{E} \times \vec{B}$  drift, which has a frequency

$$\omega_m = \frac{\omega_c}{2} - \sqrt{\left(\frac{\omega_c}{2}\right)^2 - \frac{\omega_z^2}{2}} \quad (2.7)$$

The cyclotron motion is modified due to the axial and magnetron motion, which has a frequency of

$$\omega'_c = \frac{\omega_c}{2} + \sqrt{\left(\frac{\omega_c}{2}\right)^2 - \frac{\omega_z^2}{2}} \quad (2.8)$$

A stable bound-trajectory is achieved with the condition  $\omega_z \leq \omega_c/\sqrt{2}$ . The frequencies can be ranked by

$$\omega_m \ll \omega_z \ll \omega_c \quad (2.9)$$

The complex geometry of the ideal Penning trap electrodes presents several technical challenges such as little access to loading particles. A Penning-Malmberg (PM) trap uses a series of open-access cylindrical electrodes to produce the electric quadrupole potential. A set of electrodes with certain length and voltage ratios can be used to minimize trap anharmonicities [56]. The PM trap geometry has several advantages over the ideal Penning trap. For example, it is simpler to load particles in an open-ended cylinder.

## 2.5 Buffer-Gas Trap

The  $e^+$  buffer-gas trap (BGT) is based on the design by Clifford Surko at UCSD [57]. The moderated  $e^+$  are guided into a vacuum chamber containing a three-stage differentially-pumped trap. The electrodes are a modification of a PM trap that is a series of hollow gold-plated cylinders with various lengths and diameters to provide regions of successively lower pressure and lower electrostatic potential. The electrodes can be individually biased to generate electrostatic potential wells for axial confinement of the  $e^+$ . A 2 m long solenoid provides a homogeneous 0.12 T magnetic field over the length of the electrode stack for radial confinement. A buffer-gas injected into the first-stage distributes into the three-stages and removes kinetic energy from the moderated  $e^+$  beam via inelastic collisions. Successive inelastic collisions axially confine the  $e^+$  to the deepest electrostatic well in the third-stage. The third-stage has the lowest base pressure where  $e^+$  can be accumulated for extended lifetimes. A schematic of the system is shown in Figure 2.11.

The 2 m long solenoid is constructed from 1.27 cm  $\times$  1.27 cm square cross-section copper wire continuously wound over 2 m, with 4 layers of winding. At the each end of the 2 m long solenoid, an additional layer consisting of 15 turns extends the homogeneity of the magnetic field. The core of the copper wire is hollow with a 0.635 cm diameter hole such that chilled water can be circulated to provide cooling. Typically, 300 A is applied to the solenoid at 30 V, generating 9 kW of Joule heating. The current is monitored through a low-resistance shunt and the voltage across the magnet leads are monitored for diagnostics of the solenoid. The temperature of the solenoid is monitored on the outer surface of the epoxy insulation to initiate a shutdown of the current if it exceeds a threshold temperature of 55 °C. The constant current is provided by five high-current power supplies (TCR 10T500) connected in series in a primary-replica operation. The primary supply operates in a constant-current mode to provide 300 A. The replica supplies operate in constant-voltage mode to output the necessary voltage to draw 300 A.

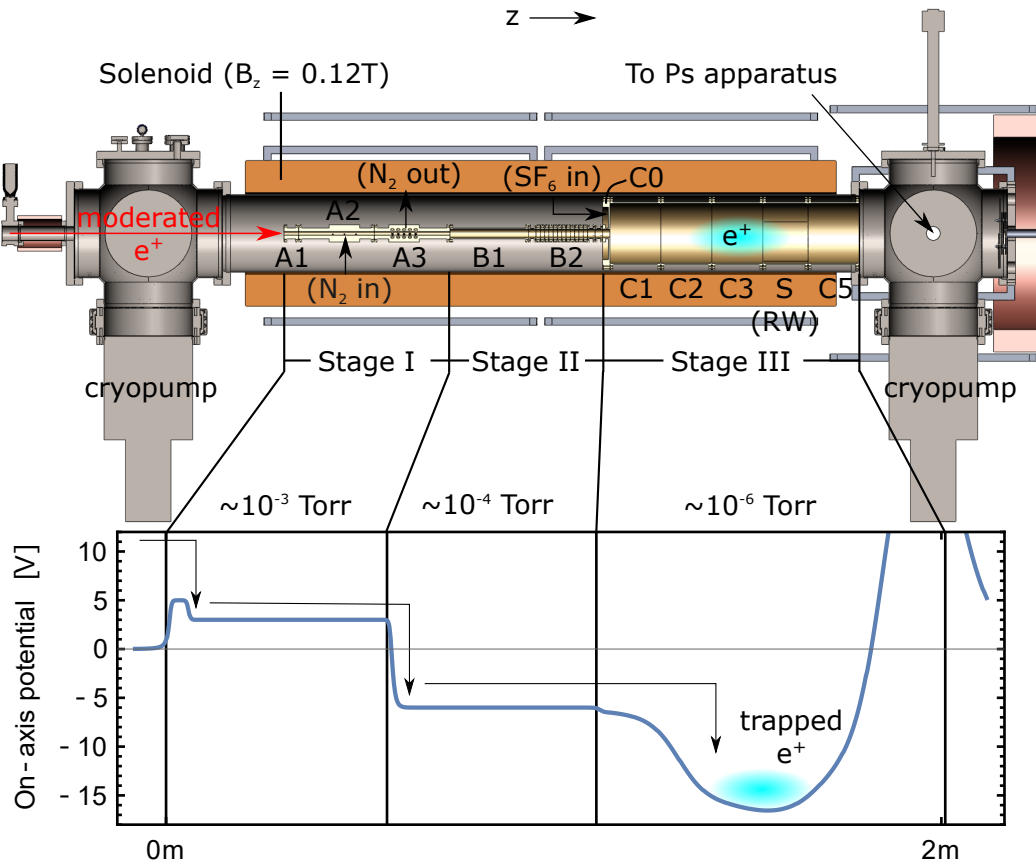


FIGURE 2.11: Schematic of the three-stage buffer-gas accumulator. Nitrogen buffer-gas is injected into the first-stage where the latter-stages are at lower pressure from differential pumping. The bottom plot represents the on-axis electric potential generated from the electrode stack to trap  $e^+$ . The  $e^+$  accumulate in stage III after three collisions with nitrogen molecules.

The vacuum chamber consists of a 2 m long, 0.254 m diameter stainless steel cylinder where each end is pumped by a 10 000 L/s cryopump (SHI Marathon CP12). This provides a clean hydrocarbon-free vacuum system with a  $5 \times 10^{-9}$  Torr base pressure suitable for trapping  $e^+$ . It is critical to minimize the amount of long-chain hydrocarbons since these lead to large  $e^+$ -annihilation rates due to large  $Z_{eff}$  [58].

### 2.5.1 Three-Stage Penning Trap Electrodes

The room-temperature three-stage Penning trap electrodes are shown in Figure 2.11. The A and B electrodes are machine from oxygen-free-high-conductivity

Electrode Parameters				
Stage	Electrode ID	Length (cm)	Inner $\phi$ (cm)	Note
I	A1	5	1.27	$A1 < (E_{e^+} - 9\text{V})$
	A2	26	1.27	N <sub>2</sub> input
	A3	26	1.27	N <sub>2</sub> output baffle
II	B1	27	3.05	
	B2	25.5	3.05	
III	C0	2.5	3.05	SF <sub>6</sub> input
	C1	17.5	20.5	
	C2	17.5	20.5	Ramp
	C3	17.5	20.5	Pulse
	S	17.5	20.5	Rotating Wall
	C5	17.5	20.5	Gate

TABLE 2.2: The dimensions of the electrodes comprising the three-stage Penning trap.

(OFHC) copper that is gold-plated. The C-electrodes are machined from aluminum that is plated with OFHC copper, and the copper is plated with gold. The copper provides high electrical conductivity while the gold is used for its non-reactive properties to avoid oxidation. Insulating patch potentials on the electrodes (from oxide layers for example) can charge up and distort the cylindrically-symmetric electric potentials that are used to trap  $e^+$ . The asymmetries lead to radial walk-off of the trapped  $e^+$  that results in less dense and larger diameter plasmas. The electrodes are electrically isolated, aligned, and separated by precision-machined Macor ceramic spacers to ensure that the electrodes are concentric to one another. The Macor spacers also align the entire electrode stack to the central magnetic field line generated by the 2 m solenoid. Table 2.2 lists the various electrodes used and their dimensions.

The electrodes are individually biased with custom electronics that are built by Jim MacArthur from Harvard University's electronics shop. A series of digital to analog converters (DACs) produce  $-10\text{V}$  to  $10\text{V}$  outputs with 16-bit resolution. The DAC outputs are amplified by a factor of 100 and low-pass filtered with an array of amplifiers, with a set limit of  $\pm 700\text{V}$  determined by the high voltage power supply limits.

Nitrogen gas ( $\text{N}_2$ ) is injected into Stage I through the A2 electrode, where the pressure is about  $1 \times 10^{-3}$  Torr measured with a convectron gauge. The A3 electrode contains a rotatable baffle to adjust the ratio of nitrogen flowed into Stage I and II by varying the amount of  $\text{N}_2$  pumped out of the baffle into the vacuum system. The baffle can be manually rotated by a series of gears controlled by a rotary feedthrough. The sulfur-hexafluoride ( $\text{SF}_6$ ) cooling gas for the rotating wall compression (discussed in Section 2.5.4) is injected into Stage III via a hole in the C0 plate electrode, where approximately  $3 \times 10^{-8}$  Torr is injected as measured by a nearby ion gauge. The flow of  $\text{N}_2$  and  $\text{SF}_6$  gas is controlled by a gas handling system and pneumatic switching of gas valves. The flow rate is precisely controlled with leak valves and is set to the position that generates the desired pressure as measured on the pressure gauges. When the gas flow to the accumulator is shut, the leak valve output flow is redirected to a path that is pumped by a scroll pump to avoid an initial large burst of gas flow into the accumulator when the valve is re-opened.

## 2.5.2 Moderated Positron Beam Energy

To efficiently trap  $e^+$  from the moderated beam, a mono-energetic beam is desired for inelastic collisions with the buffer-gas. The total energy  $E$  of the  $e^+$  is represented by

$$E = \underbrace{eV_o}_{\text{potential energy}} + \underbrace{\frac{1}{2}m_e v_{\perp}^2 + \frac{1}{2}m_e v_{\parallel}^2}_{\text{kinetic energy}} \quad (2.10)$$

where  $V_o$  is the electric potential at the  $e^+$  location,  $v_{\perp}$  is the transverse speed of the cyclotron orbit around a magnetic field line, and  $v_{\parallel}$  is the parallel speed along the direction of the magnetic field line. The magnetic dipole moment of a charged particle within a magnetic field is a conserved quantity, also known as an adiabatic invariant. The  $e^+$  magnetic dipole moment  $\mu$  is given by

$$\mu = \frac{m_e v_{\perp}^2}{2B} = \frac{m_e v_{\perp}'^2}{2B'} \quad (2.11)$$

where  $B$  is the magnetic field strength at the  $e^+$  location. From Eqn. 2.11, an increase in the magnetic field strength,  $B'$ , results in an increase in kinetic energy in the transverse speed,  $v_{\perp}'$ , in order to conserve the magnetic dipole moment. From energy conservation, if  $V_o$  remains constant and the  $e^+$  moves from a weak magnetic field,  $B$ , to a stronger magnetic field,  $B'$ , the increase in  $v_{\perp}'$  results in a decrease in  $v_{\parallel}'$ . Depending on the ratio of  $v_{\perp}/v_{\parallel}$  and  $B/B'$ , this can result in a case where  $v_{\parallel}' < 0$  where the  $e^+$  is reflected. This situation is called magnetic mirroring. The mirror ratio  $M$  is defined as

$$M = \frac{B'}{B} = \frac{1}{\sin^2(\theta)} = \left(\frac{|v|}{v_{\perp}}\right)^2 \quad (2.12)$$

where  $|v|$  is total speed and  $\theta$  is the angle between  $|v|$  and  $v_{\parallel}$ . These conditions define a loss cone where  $e^+$  with  $v_{\perp} > |v|/\sqrt{M}$  are reflected.

The energy distribution of the moderated beam is analyzed by guiding the beam through the electrode stack and annihilating the beam on the output valve before the Ps apparatus. The gamma count rate is monitored with a gamma detector that is positioned 13.5 cm away from the center of the valve. The moderator is biased to 12 V to set the beam energy to approximately 12 eV relative to the grounded gate valve. The retarding potential analyzer (RPA) used for this analysis is the B1 electrode where >99% of the applied potential is generated on-axis. As the RPA voltage is raised, the fraction of  $e^+$  with parallel kinetic energy less than  $eV_{RPA}$  become blocked by the potential barrier. The decreased amount of  $e^+$  guided to the output valve is observed by a reduction in the gamma count rate. The result of this scan is shown in Figure 2.12.

The transmitted fraction data is fit to an exponentially-modified Gaussian (EMG) distribution. The derivative represents the parallel energy distribution where the FWHM can be used to determine the energy width. The resulting FWHM energy

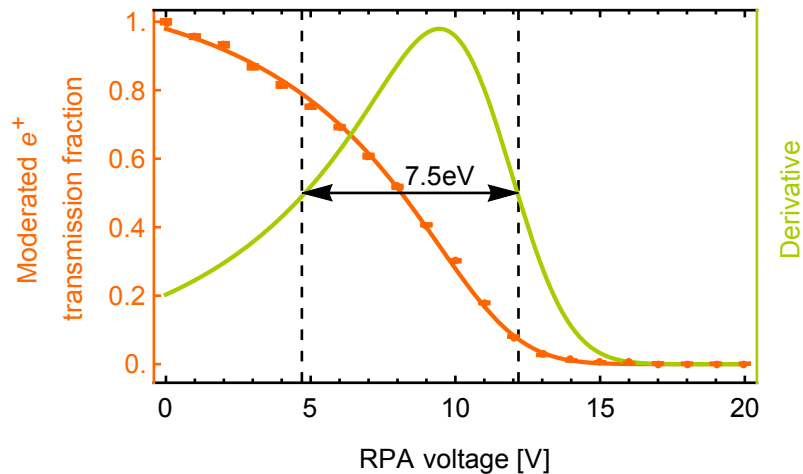


FIGURE 2.12: The blocking distribution (orange) for a 12 eV moderated beam using the B1 electrode as a RPA. The derivative of the curve (green) represents the energy distribution. Due to magnetic mirroring, the energy distribution is broadened and appears to peak at  $\sim 10$  eV.

width is 7.5 eV which is quite broad compared to distributions found by other groups with a minimal bias applied to the moderator [28]. However, a larger yield of  $e^+$  are extracted from the moderator with the 10 V to 40 V biases used in this experiment. The skew of the distribution is attributed to the transverse energy component and magnetic mirroring from the moderated beam reflecting from the  $B_R = 0.12$  T magnetic field at the location of the RPA [59]. The  $e^+$  are extracted from a  $B_S = 0.006$  T magnetic field at the moderator, resulting in a magnetic mirror ratio of  $M = B_R/B_S \sim 20$ .

An increase in the source magnetic field can reduce the mirror ratio to improve the number of  $e^+$  entering the buffer-gas accumulator for trapping by  $\sim 50\%$ , based on a purely Gaussian distribution without magnetic mirroring (see Figure 2.13). This leads to an expected width of 4 eV, where a larger fraction of the  $e^+$  can be efficiently trapped from buffer-gas collisions.

### 2.5.3 Inelastic Collisions with $N_2$ Buffer-Gas

The kinetic energy from the moderated  $e^+$  beam is removed via inelastic collisions with a buffer-gas. A commonly used buffer-gas is molecular  $N_2$ , where an inelastic collision with the molecule transfers approximately 9 eV of kinetic energy to the

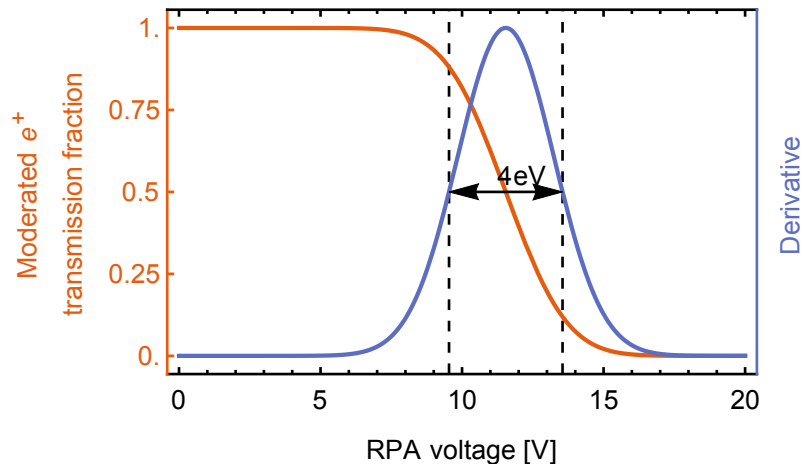


FIGURE 2.13: The expected blocking distribution (red) and energy distribution (blue) without magnetic mirroring of the moderated  $e^+$  beam. The energy distribution is peaked at  $\sim 12$  eV as expected. The fit parameters are identical to the parameters used for the fits in Fig. 2.12, with the exception of the exponential-modification term reduced to 0.

$N_2$   $a^1\Pi$  electronic state [60]. A  $e^+$ -impact on nitrogen molecules can also form Ps however there is a narrow window of a few eV centered at  $\sim 9$  eV where  $N_2$  electronic excitation is the dominant process over Ps formation. This range of energy is suitable for trapping a large fraction of the 7.5 eV-wide moderated  $e^+$  beam.

### 2.5.4 Rotating Wall

Several factors can lead to a radial expansion of the accumulated  $e^+$  plasma such as field asymmetries due to trap and magnetic field alignments and collisions with the nitrogen buffer-gas. This results in poor accumulation rates and storage lifetimes. A misalignment of the trap electrodes with the solenoid magnetic field can break the cylindrical symmetry required to trap the  $e^+$  efficiently. The necessary presence of low-pressure nitrogen in the stage III electrodes provides opportunities for elastic collisions with  $e^+$  that push them out radially.

A technique to radially compress the  $e^+$  plasma to increase the density,  $e^+$  number, and extend the storage lifetime is achieved via the “rotating wall” method in the weak-field regime [61]. The rotating wall technique generates a rotating radial

electric field that injects angular momentum into the trapped  $e^+$  plasma when the applied frequency coincides with a rotating Trivelpiece-Gould plasma mode [62]. For an uncompressed plasma to couple to the rotating wall, it has to be in a well-defined plasma state. A characteristic dimension for a plasma is the Debye length  $\lambda_D$ , which is defined as

$$\lambda_D = \sqrt{\frac{\varepsilon_0 k_B T}{n e^2}} \quad (2.13)$$

where  $\varepsilon_0$  is the permittivity of free space,  $k_B$  is the Boltzmann constant,  $T$  is the plasma temperature,  $n$  is the plasma density and  $e$  is the elementary charge. For a room-temperature, uncompressed plasma containing  $N_{tot} = 2 \times 10^6 e^+$  with a plasma radius  $R_p = 2$  mm, a plasma length of  $L_p = 15$  cm, a density of  $n = 5 \times 10^5 \text{ cm}^{-3}$ , the Debye length is  $\lambda_D = 0.5$  mm. The condition that  $\lambda_D \ll L_p, R_p$  and  $n\lambda_D^3 \gg 1$  is satisfied such that the uncompressed plasma is considered in the plasma regime.

An azimuthally segmented electrode with a time-varying voltage applied to each segment generates the rotating electric field. The plasma radius is much smaller than the electrode diameter such that it is within the region that produces the most ideal rotating electric field. For a four-segmented electrode, the ‘‘dipole drive’’ is a sinusoidal voltage where segments 1, 2, 3, 4 are offset in phase by  $0^\circ$ ,  $90^\circ$ ,  $180^\circ$ ,  $270^\circ$  as shown in Figure 2.14. The  $e^+$  plasma produces a radial electric field  $\mathbf{E}$  and has an  $\mathbf{E} \times \mathbf{B}$  drift rotation around the central magnetic field  $\mathbf{B}$ , where the total angular momentum would be conserved if the drag torque from field-asymmetries and background gas collisions were not present [63]. The total angular momentum is given by

$$P_\theta = \sum_j \left( m v_\theta r_j - \frac{e B r_j^2}{2c} \right) \quad (2.14)$$

The first part of the Eq. 2.14 represents the mechanical momentum for the  $j$ th particle and the second term represents the canonical momentum. In a strong magnetic field, the canonical momentum term dominates, resulting in

$$P_\theta \approx -\frac{eB}{2c} \sum_j r_j^2 \quad (2.15)$$

From Eq. 2.15, it can be seen that the total angular momentum is a negative quantity. The drag torque removes angular momentum from the plasma ( $\Delta P_\theta < 0$ ), resulting in plasma expansion where there is a net increase of  $r_j$ . Analogously, by adding angular momentum to the plasma with the rotating wall ( $\Delta P_\theta > 0$ ), the plasma compresses due to the decrease in  $r_j$ .

The plasma rotation frequency is dependent on the plasma density  $n$  and the strength of the magnetic field  $B$ , given by the equation

$$f_E = \frac{ne}{4\pi\epsilon_0 B} \quad (2.16)$$

For a plasma of  $2 \times 10^6 e^+$  in a  $\sim 10$  cm long well with a  $\sim 1$  mm diameter, the approximate rotation frequency is approximately in the kHz range. The applied frequencies used in this apparatus typically ranges from 200–1000 kHz. The amount of compression plateaus when the torque applied by the rotating wall is balanced by the drag torque applied by the field asymmetries and background gas collisions.

The work applied to the plasma by the rotating wall torque  $\tau_{RW}$  results in heating where the minimum heat is

$$W = 2\pi f_{RW} \tau_{RW} \quad (2.17)$$

The heating of the plasma results in an expansion that must be counteracted by a cooling mechanism. For the rotating wall applied to an  $e^-$  plasma in Ref. [63], the plasma was trapped in a strong 4 T magnetic field where the  $e^-$  cooled quickly by cyclotron radiation (0.18 s in 4 T). The time constant for cyclotron radiation damping is

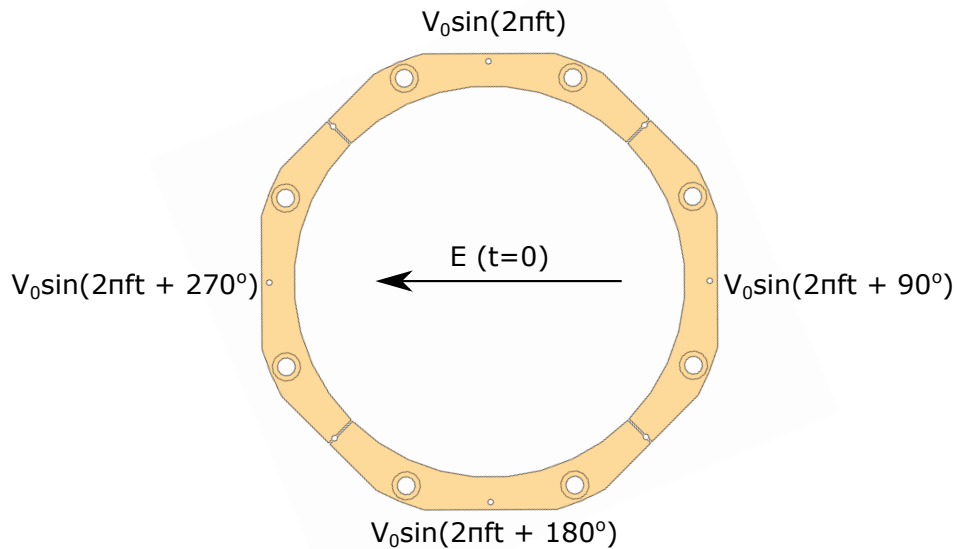


FIGURE 2.14: A schematic of the applied voltages to the segmented electrode for the rotating wall compression. Two synchronized generators produce sinusoidal waves phase-shifted by  $90^\circ$ .

$$\tau_c = \frac{3\pi\epsilon_0 m_e^3 c^3}{e^4 B^2} \quad (2.18)$$

The buffer-gas accumulator magnetic field is much weaker such that the timescale for cyclotron radiation is much longer (200 s in 0.12 T) and is not a practical cooling mechanism. An inelastic collision with a buffer-gas that has a long annihilation time constant and a short cooling time-constant is used to cool the plasma instead. Table 2.3 shows the cooling properties for various gases. Although there is nitrogen in the trap, the cooling time constant is long compared to SF<sub>6</sub>. The cooling gas used is SF<sub>6</sub>, which has a short  $e^+$  cooling time constant of 0.36 s and has a minimum vibrational excitation of 0.076 eV. This vibrational excitation quanta is comparable to the room-temperature thermal energy of 0.025 eV and sets the lower limit of the energy in the transverse motion. The smallest vibrational quanta is desired to limit the amount of transverse energy that can be transferred to axial energy during  $e^+$  transport.

The rotating wall voltages are generated by a pair of synchronized arbitrary waveform generators (Rigol DG4062) that each have two-channel outputs. The generator outputs the sinusoidal voltages with the  $90^\circ$  phase shift between channels.

$e^+$ Cooling Gases			
Gas	$\tau_a$ (s)	$\tau_c$ (s)	$E_v$ (eV)
SF <sub>6</sub>	2200	0.36	0.076, 0.19
CF <sub>4</sub>	3500	1.2	0.16
CO <sub>2</sub>	3500	1.3	0.29, 0.083
CO	2400	2.1	0.27
N <sub>2</sub>	6300	115	0.29

TABLE 2.3: The  $e^+$  annihilation time constant,  $\tau_a$ , and cooling time constant,  $\tau_c$ , with  $2 \times 10^{-8}$  Torr of various gases.  $E_v$  is the vibrational energy quanta of each gas. SF<sub>6</sub> is used as the cooling gas for the short cooling time constant and long annihilation time constant. Table is adapted from [61].

The voltages are capacitively coupled to the common DC voltage applied to the four quadrants of the S electrode. The  $e^+$  are accumulated in well centered on the C3 electrode and feel the effect of the rotating wall on one end of the plasma from the adjacent S electrode. Figure 2.15 shows the accumulated  $e^+$  as a function of the rotating wall frequency with a fixed amplitude setting of 8 V. It can be seen that the accumulation is broadband and peaks at 500 kHz, and the decay can be attributed to the drive frequency is out of resonance with a Trivelpiece-Gould mode. Figure 2.16 shows a scan of the rotating wall amplitude setting with a fixed frequency of 500 kHz. The accumulated number of  $e^+$  begins to plateau at 3 V, but an apparent peak at 8 V is observed. The capacitive-coupling of the rotating wall signal modifies the actual voltage applied at the electrode that depends on the applied frequency and voltage, so this apparent peak could be due to a coupling effect.

The radial compression of the  $e^+$  plasma can be observed by imaging the plasma on the phosphor screen. A sample image of a compressed  $e^+$  plasma is shown in Figure 2.17. In Figure 2.18, the rotating wall frequency is scanned and a CCD image of the plasma is captured for each frequency setting. The radial profile is image-analyzed and plotted. The rotating wall couples efficiently to the plasma after 300 kHz where the width is reduced, and increasing the frequency to 500 kHz leads to a more dense plasma by reducing the number of  $e^+$  that exit the trap radially.

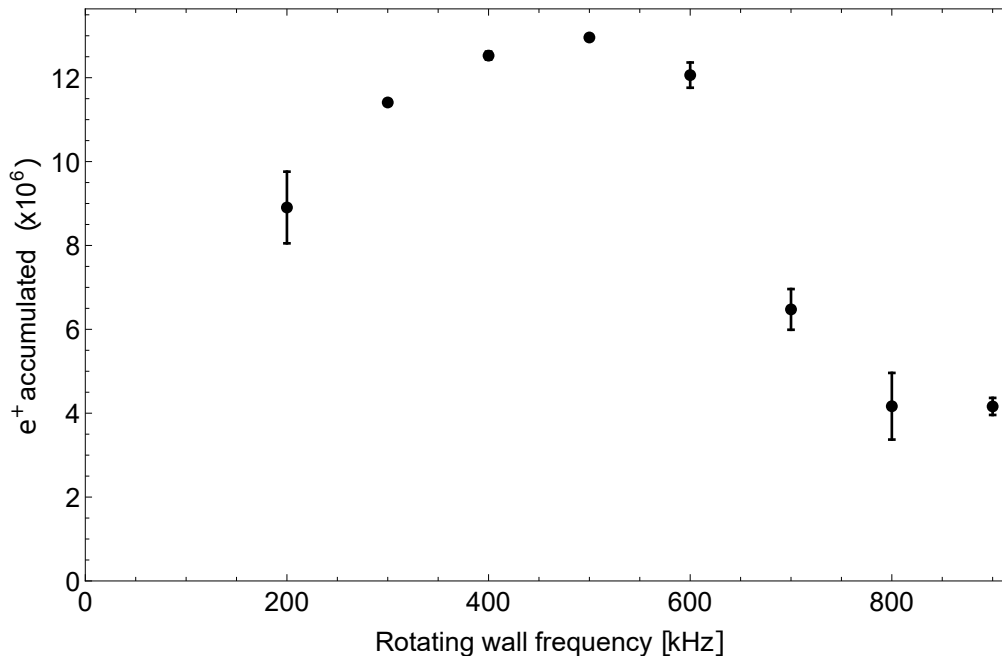


FIGURE 2.15: The number of accumulated  $e^+$  for various rotating wall frequencies. The rotating wall amplitude is fixed at 8 V, and the accumulation time is fixed to 30 s.

## 2.6 Positron Accumulation

The  $e^+$  are accumulated in stage III of the electrode stack and pulsed out of the trap for counting on a Faraday cup. The on-axis potential generated by the applied voltages to the electrodes varies throughout the procedure to accumulate  $e^+$ , to cool  $e^+$ , and to dump  $e^+$  out of the trap. The rotating wall is applied to the S-electrode throughout the procedure. A constant flow of  $\text{SF}_6$  is admitted into stage III to provide  $3 \times 10^{-8}$  Torr of cooling gas.

During the accumulation phase (shown in Figure 2.19(a)), the moderator is biased to 12 V to give the moderated  $e^+$  12 eV of kinetic energy. The optimal accumulation potentials has stages biased  $\sim 9$  V lower than the each stage. This is well matched to the 9 eV electronic excitation of  $\text{N}_2$ . Stage I is set to 3 V for the first inelastic collision, stage II is set to  $-6$  V for the second inelastic collision, and stage III forms the minimum of the electric potential well with a  $-15$  V depth to trap  $e^+$ . The electric potential well to trap  $e^+$  is centered on the C3 electrode, where the C5 gate electrode is held at 30 V to contain the trapped  $e^+$  and to reflect  $e^+$  that did not experience three inelastic collisions. The A1 entrance electrode is set a few

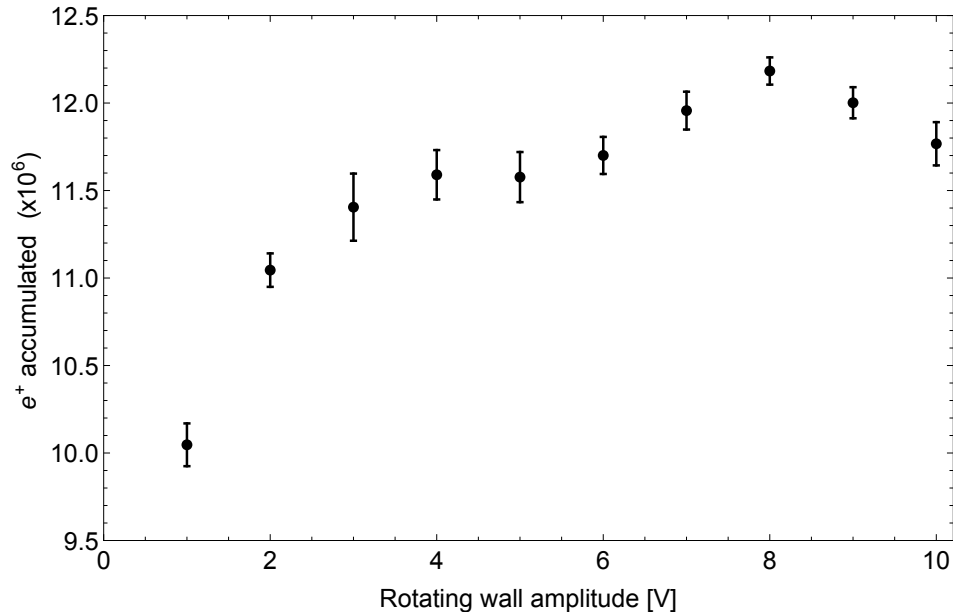


FIGURE 2.16: The number of accumulated  $e^+$  for various rotating wall amplitudes. The rotating wall frequency is fixed at 500 kHz, and the accumulation time is fixed to 30 s.

volts lower ( $A1 = 5$  V) than the moderator bias to narrow the energy distribution of the admitted  $e^+$  and to contain the  $e^+$  between A1 and C5 if it experienced an inelastic collision in transit. The nitrogen flows into the A2 electrode for a chosen accumulation time and the well begins to fill with  $e^+$ . The A1 entrance electrode is then raised to 80 V to block the incident moderated  $e^+$ , and the nitrogen flow is shut. The nitrogen is quickly pumped out of the system and the trapped  $e^+$  are radially compressed and cool with the  $\text{SF}_6$ . The  $e^+$  cool with  $\frac{1}{2}k_B T$  per degree of freedom and are expected to have a thermal energy width on the scale of  $\sim 40$  meV [64].

After the cooling phase, the  $e^+$  are prepared for ejection out of the trap with two different methods. For the “pulsed beam”, the  $e^+$  are quickly dumped out of the trap as a collective plasma with a short temporal width. For the “ramped beam”, the  $e^+$  slowly exit the trap in the single-particle regime by ejecting the  $e^+$  out of the trap on a time scale much longer than the axial bounce time. The two techniques are discussed in the following subsections.

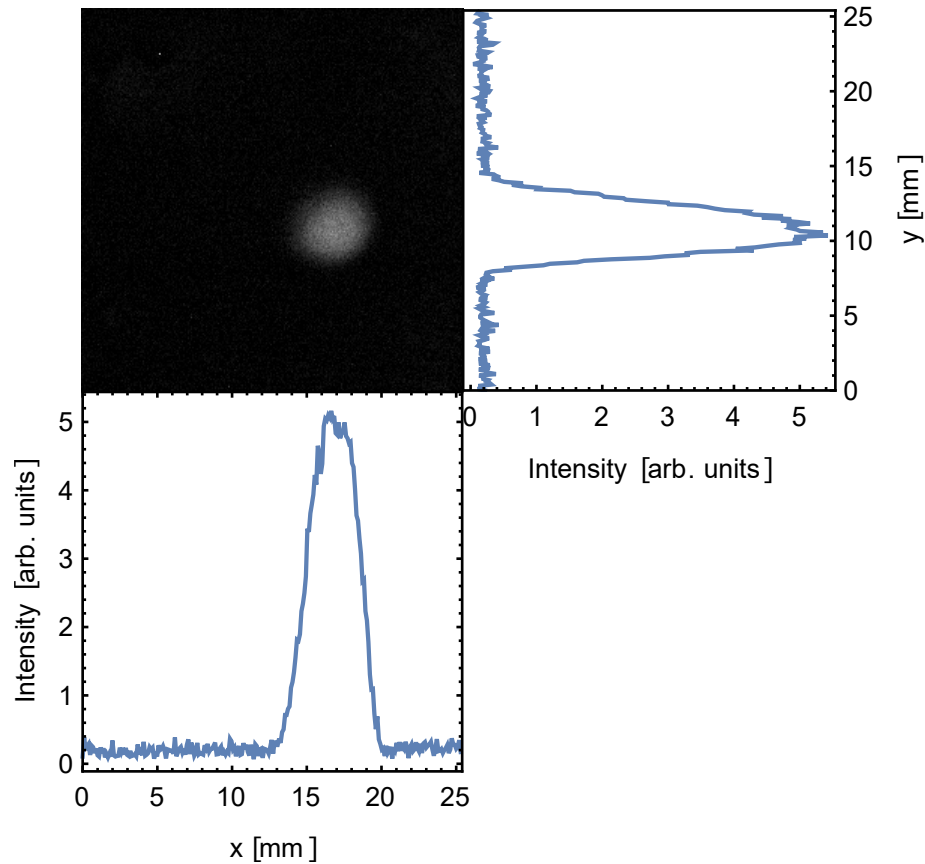


FIGURE 2.17: An image of a plasma of 2 million  $e^+$  over the 2.54 cm diameter phosphor screen. The  $e^+$  are compressed with the rotating wall operating at 500 kHz at 2 V amplitude.

### 2.6.1 Pulsed Beam

To approach the dump-out phase for the pulsed beam (shown in Figure 2.19(c)), the  $e^+$  potential well is lifted to a two-electrode long “dump-out well” centered between C1 and C2 with a 40 V minimum. Electrodes C0 and C3 are held at 80 V and 60 V respectively. The on-axis potential is formed in several steps to gently move the  $e^+$ , where the total time to transition to the dump-out well is approximately 0.5 s. A negative voltage pulse (DEI HV1000) is coupled to the C3 electrode through a bias tee to pulse down the electrode by 30 V, to dump the  $e^+$  out of the trap (shown in 2.19(c)). The pulse is triggered by an SRS DG645 digital delay generator. The 6 ns pulse rise time is short compared to the axial bounce time and the pulse is held for 10  $\mu$ s which is longer than the axial bounce time. This condition ensures that all of the  $e^+$  exit the trap as a plasma in  $\sim 20$  ns. This temporal width is much smaller than the decay constant of the

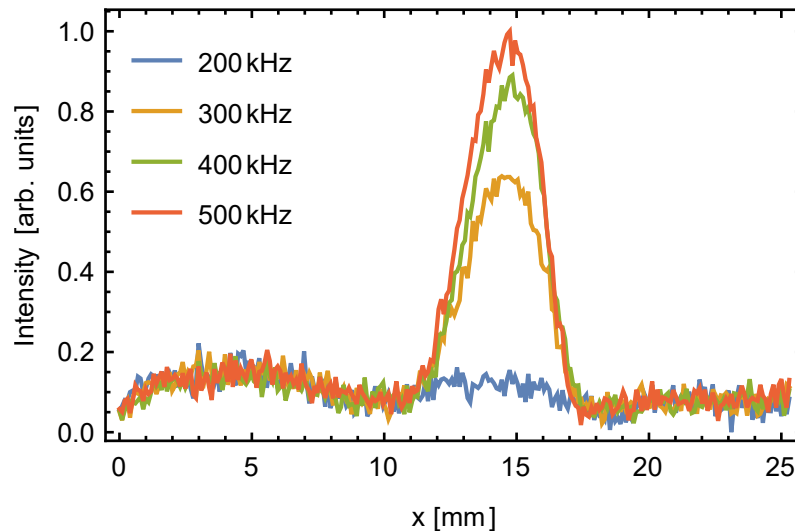


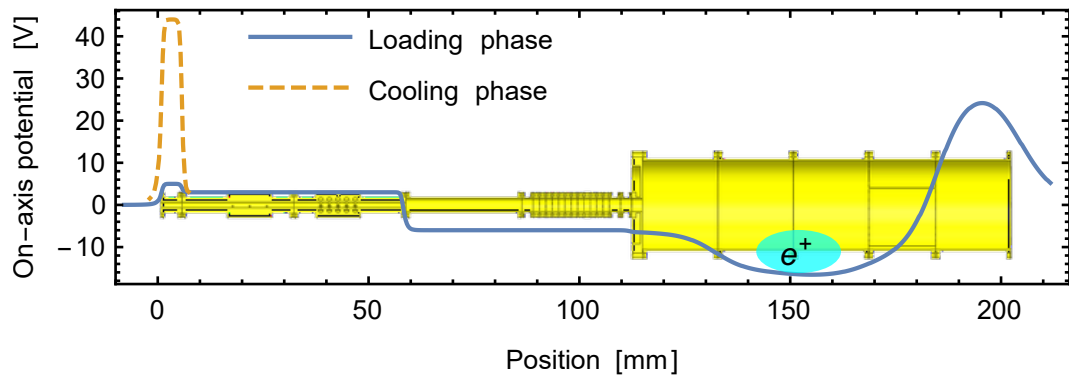
FIGURE 2.18: The radial profile along the  $x$  dimension for a  $e^+$  plasma up to 2 million  $e^+$ , with a constant accumulation time for each trial. The rotating wall amplitude is set to 2.5 V.

Faraday cup charge preamplifiers ( $\tau = 140 \mu\text{s}$ ) such that the total charge can be counted.

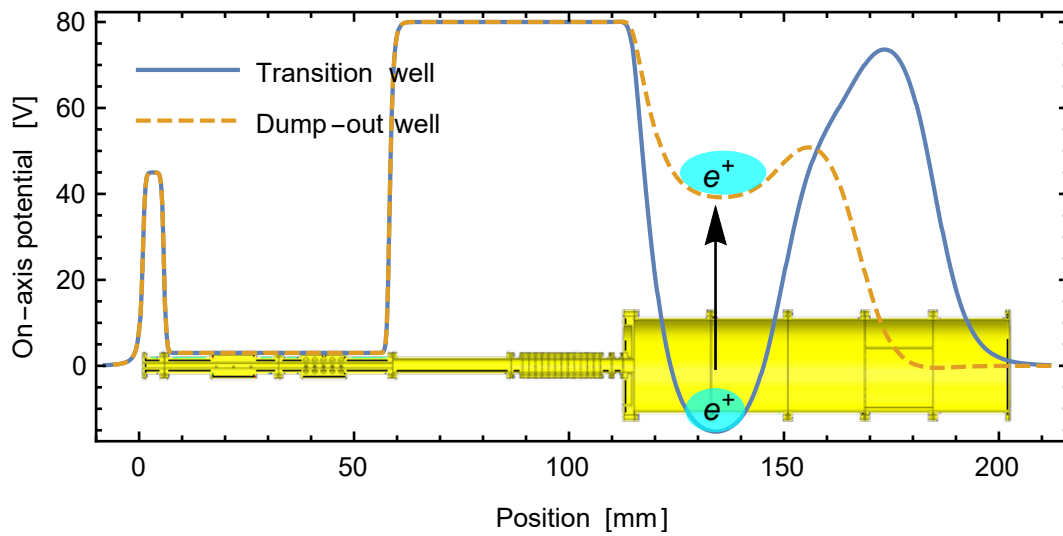
A plot of the number of  $e^+$  accumulated is shown in Figure 2.20 where the accumulation grows linearly and eventually plateaus due to the balance of  $e^+$  annihilation and accumulation. A linear fit to the initial data points gives a linear loading rate of approximately  $10^4 e^+/\text{s/mCi}$ . For the  $\text{Ps}^*$  experiment, the largest linear loading rate is desirable to accumulate  $e^+$  in the shortest amount of time. The loading rate is tuned by the amount of nitrogen pressure injected into the trap as seen in Figure 2.21. For these experiments, it is determined that 5 mTorr of nitrogen provided the optimal loading rate.

To study the lifetime of the trapped  $e^+$ , the  $e^+$  are accumulated for a fixed amount of time and held in the cooling phase for a variable amount of time before being dumped out. As it can be seen from Figure 2.22, the number of  $e^+$  exponentially decays with a long time constant of 540 s.

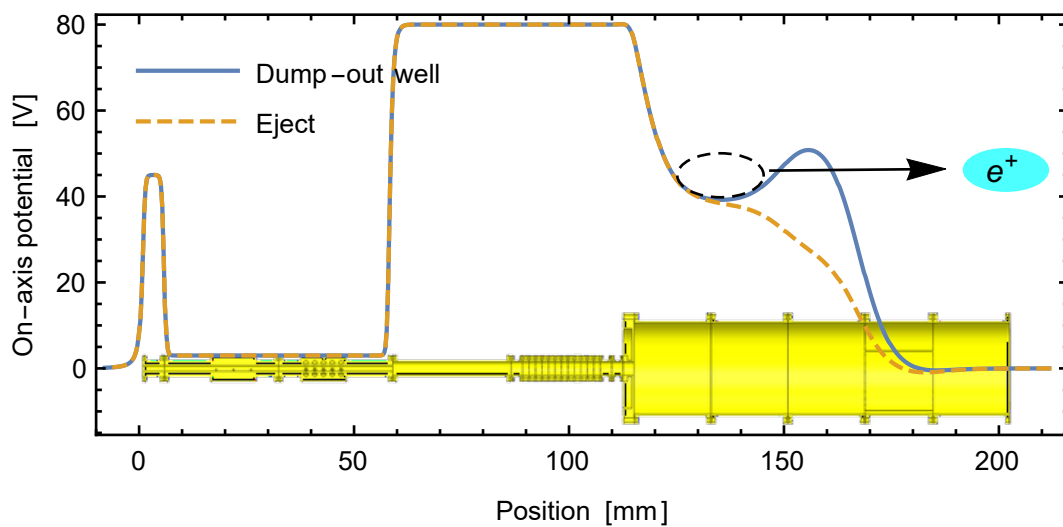
The plasma profile is studied by dumping the  $e^+$  plasma onto the MCP-phosphor screen system. The  $1/e^2$  beam diameter is measured for small accumulations as shown in Figure 2.23. The magnetic field at the imaging system is 66 G and is



(a) Loading/Cooling phase.



(b) Transition to dump-out well.



(c) Dump-out phase for pulsed beam.

FIGURE 2.19: A plot of the on-axis potential during a  $e^+$  accumulation cycle. a) The  $e^+$  become trapped, accumulate and cool in the stage III electrodes. b) The  $e^+$  potential well is raised to prepare for the dump out. c) The  $e^+$  are pulsed out of the trap by pulsing down the exit barrier potential.

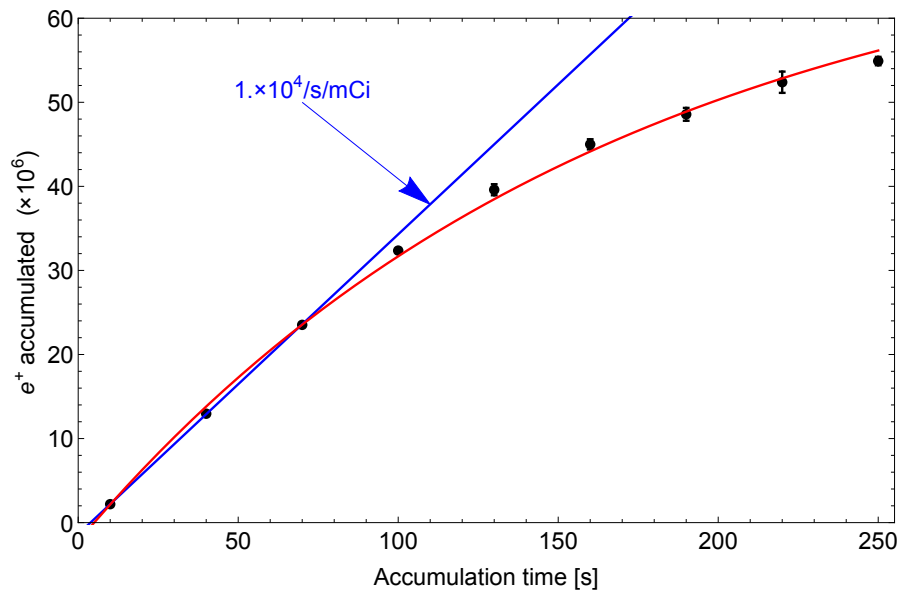


FIGURE 2.20: The number of accumulated  $e^+$  for varying accumulation times. A linear fit (blue) between 10s to 70s gives an accumulation rate of  $10^4 e^+/\text{s/mCi}$ . An exponential trend (red) predicts a maximum of  $75 \pm 4 \text{ M } e^+$  accumulated, with a time constant of  $(170 \pm 14) \text{ s}$ .

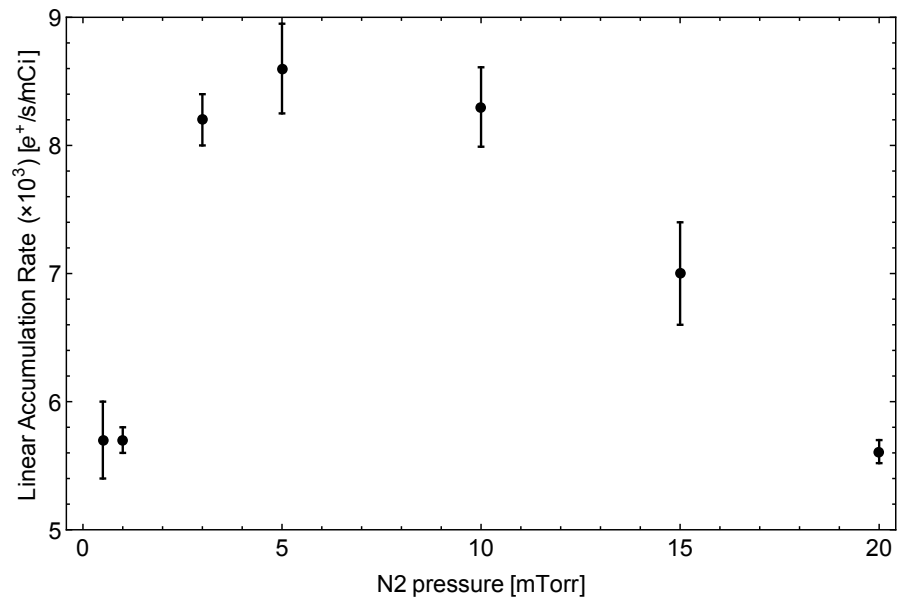


FIGURE 2.21: The linear accumulation rate for various  $\text{N}_2$  buffer-gas pressures. For each pressure, the  $e^+$  are accumulated between 10s to 30s to extract the linear rate.

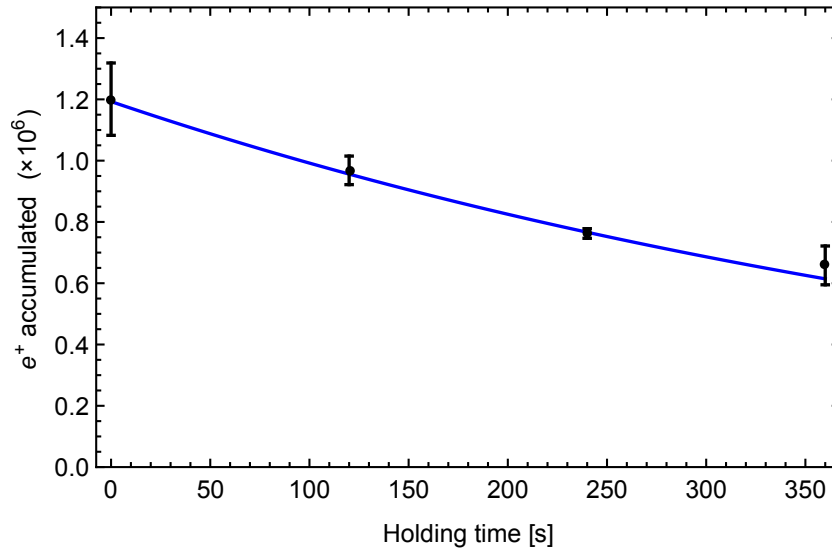


FIGURE 2.22: A scan of the number of accumulated  $e^+$  after holding the  $e^+$  in the cooling phase for a varying amount of time. The data points are the average of 4 trials. The blue curve is an exponential decay fit that has a 540 s time constant.

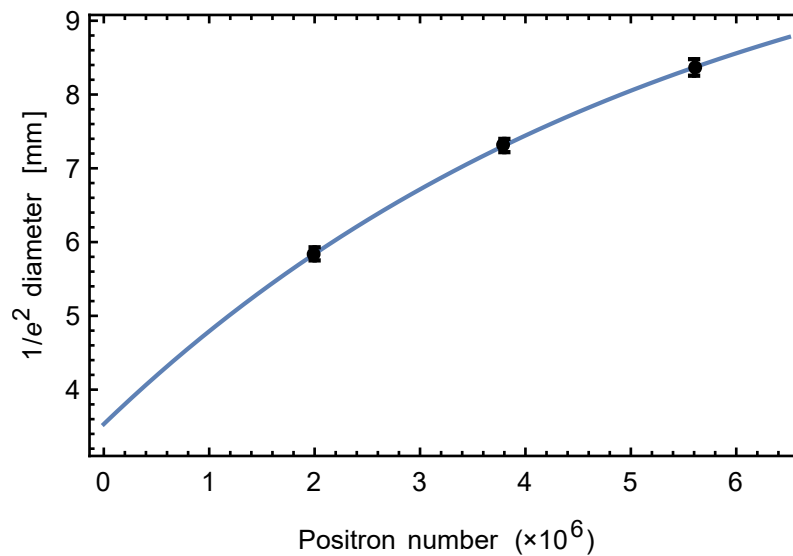


FIGURE 2.23: The diameter of the  $e^+$  plasma as a function of the number of particles contained. The  $e^+$  number count is based on Faraday cup measurements, and the diameter measurements are based on plasma-imaging measurements.

used to estimate the beam diameter along the trajectory towards the Ps apparatus for charge-exchange.

## 2.6.2 Ramped Beam

The electric potentials are modified in several steps to gently shift the  $e^+$  to a well that is centered on electrode C2 to prepare the ramped beam. The C2 electrode is biased to 34 V, with a barrier set by C1 biased to 80 V, and with electrodes C3–C5 biased to 40 V. The electrode C2 is linearly ramped from 34 V to 44 V over 3 s and the  $e^+$  slowly leak out over the 37.9 V on-axis barrier set by electrodes C3–C5. The on-axis potential at this step is shown in Figure 2.24. The  $e^+$  are ramped out of the trap in the single-particle regime where the ramp time is much longer than the axial bounce time. The most energetic  $e^+$  leave the trap earlier than the least energetic  $e^+$ , which results in a low-density beam that forms for less than 3 s. This is in contrast to the pulsed beam, where the  $e^+$  exits the trap as a single plasma. The low-density of the ramped beam makes Faraday cup counting measurements not possible since the charge is spread out in time much longer than the 140  $\mu$ s charge preamplifier time constant. The number of  $e^+$  in the ramped beam is expected to be the same as the pulsed beam since they share a common accumulation phase. With the ramped beam, single-photon counting of  $e^+$  annihilation events is possible and preserves the narrow energy width from buffer-gas cooling. A study of the energy width of the ramped beam is discussed in Section 3.3 where the  $e^+$  are adiabatically transferred through a guide and annihilated onto a gate valve.

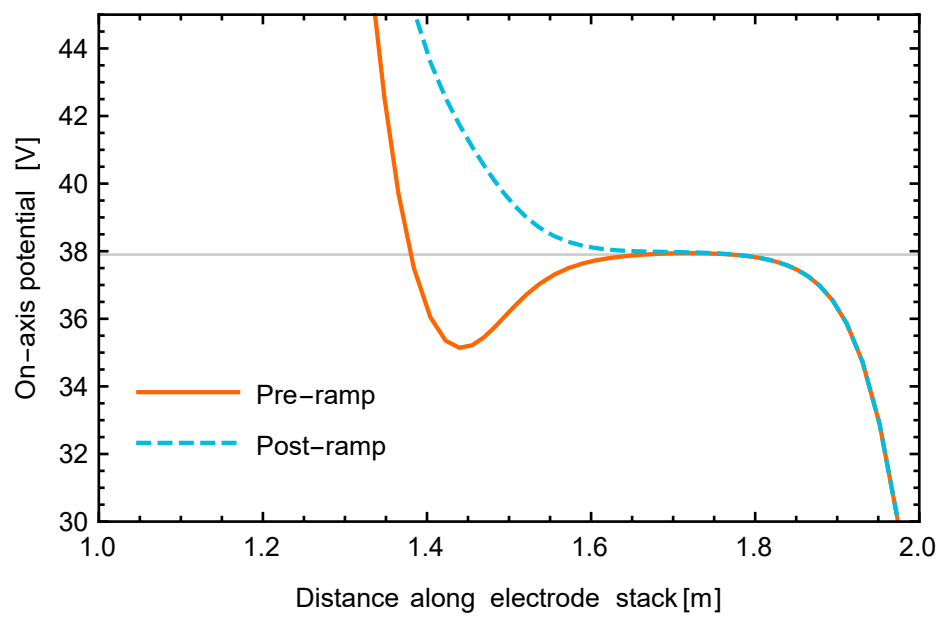


FIGURE 2.24: The on-axis potential before and after the ramp is complete. The on-axis exit potential barrier of 37.9 V sets the kinetic of the  $e^+$  that exit the trap.

# Chapter 3

## Magnetic Transfer Guide

The  $e^+$  accumulator delivers  $e^+$  to two experimental sections. Another experiment unrelated to this work is located directly downstream from the accumulator. Due to limited laboratory space,  $e^+$  are adiabatically guided through a  $90^\circ$  turn towards the Ps apparatus.

The  $e^+$  are ejected into a spherical chamber of radius 23 cm. The  $e^+$  are steered  $90^\circ$  towards a 1 m long solenoid with an inner diameter of 1.3 cm. A large hoop coil applies a magnetic field to counteract the axial field due to the accumulator, while a pair of circular transverse coils apply a magnetic field directed towards the 1 m solenoid.

To correct for transverse magnetic fields along the 1 m solenoid, pairs of rectangular coils provide local left/right and up/down corrections.

### 3.1 Magnetic Field Model

A magnetic field model was created using the Radia package in Mathematica to aid in the design of magnet coils. Three-dimensional coil geometries are generated and the magnetic field is computed based on the Biot-Savart law and the current density flowing through each coil. The magnetic field due to a combination of coil

Transfer Magnet Coils							
Coil ID	Geometry	DIM1	DIM2	DIM3	DIM4	I (A)	Turns
Big Hoop	Circular	66.0	81.3	15.9		57	300
DS Transverse	Circular	35.6	38.8	7.6		6.75	600
1 m-Solenoid	Circular	5.1	6.5	93.8		8	3300
LR4/LR5	Rectangular	38.1	6.6	1.9	1.3	0.15/0.91	110
UD4/UD5	Rectangular	38.1	6.6	1.9	1.3	0/0	110
Axial 1+2	Circular	9.4	11.2	13.3		7	600
Axial 3	Circular	7.6	8.8	8.8		5.5	260

TABLE 3.1: A list of the magnet coils used to guide  $e^+$  to the Ps apparatus. The dimensions quoted are in centimeters. Circular coils: (DIM1, DIM2, DIM3)=(inner radius, outer radius, depth), Rectangular coils: (DIM1, DIM2, DIM3, DIM4)=(inner length, inner width, depth, thickness). The actual current applied is noted, along with the approximate number of turns in each coil.

geometries and coil currents is used to simulate the trajectory of a  $e^+$  exiting buffer-gas trap. A cross-sectional view of the layout of the coils and the  $e^+$  trajectory is shown in Figure 3.1. The coils used in addition to the 2 m buffer-gas trap solenoid are listed in Table 3.1.

For low-energy  $e^+$  ( $\lesssim 100$  eV), the trajectory is modelled from an approximation that it follows a magnetic field line, ignoring the small cyclotron orbit around the field line. A  $e^+$  cooled in the trap has approximately  $k_B T$  of kinetic energy in the transverse motion. In a typical guiding magnetic field of 0.01 T, this corresponds to a cyclotron radius  $< 0.1$  mm centered on the field line. The distance travelled per cyclotron period ( $\sim 1$  cm for 40 eV) is also much shorter than characteristic dimensions of the required trajectory, such as the  $\sim 25$  cm bend radius into the 1 m-solenoid. The strength of the magnetic field along the  $e^+$  trajectory is shown in Figure 3.2. The smallest magnetic field strength experienced by the  $e^+$  beam is located in the  $90^\circ$  bend vacuum chamber and at the output valve, however, the beam diameter remains under 8 mm to avoid annihilation on the vacuum chamber surfaces.

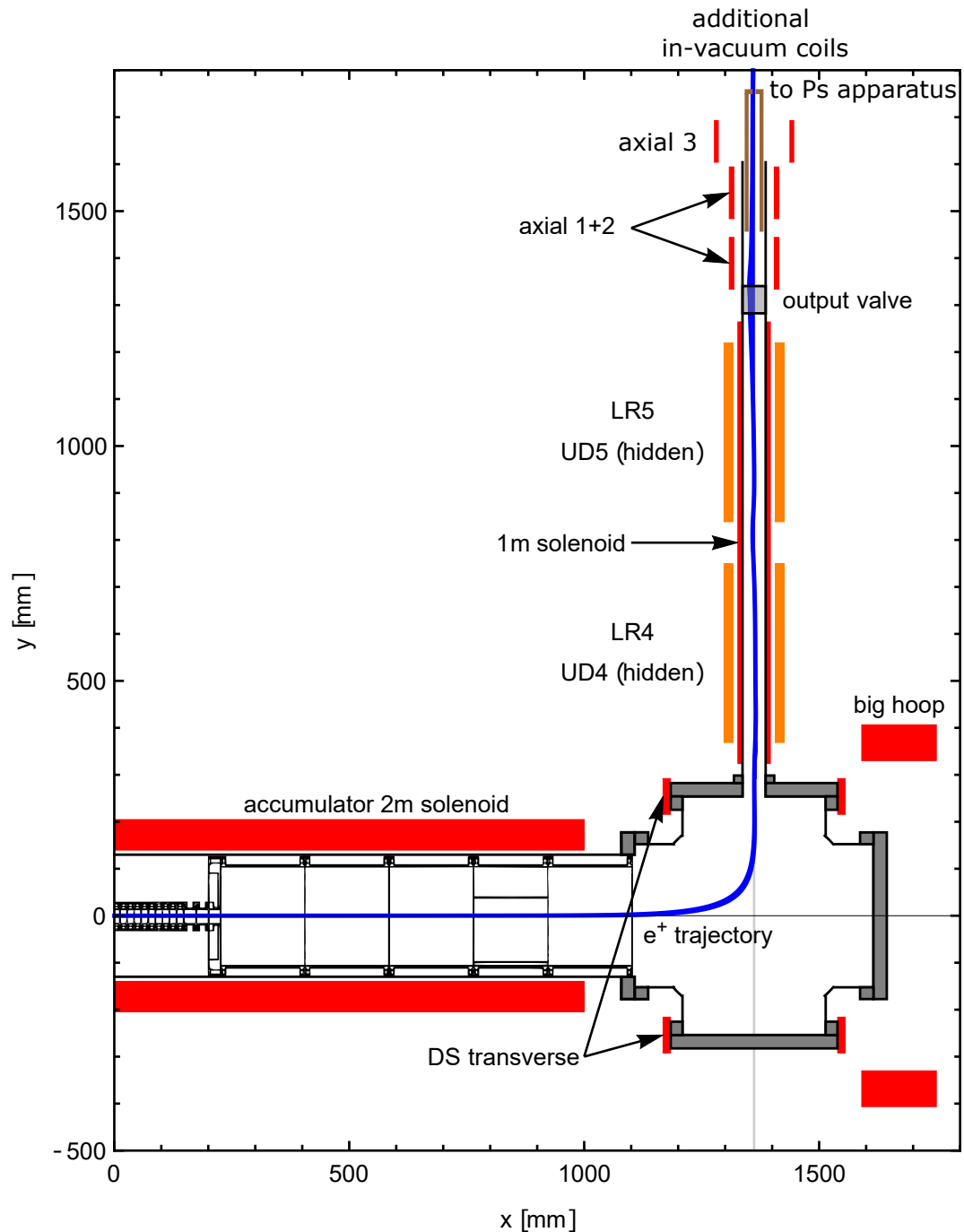


FIGURE 3.1: A cross-section view of the magnetic field generating coils (red = circular coils, orange = rectangular coils) and the  $e^+$  trajectory (blue). The width of the  $e^+$  trail represents the field-dependent beam diameter. Field direction of selected coils: Accumulator solenoid  $+\hat{x}$ , Big hoop  $-\hat{x}$ , DS transverse pair  $+\hat{y}$ , 1 m-Solenoid  $+\hat{y}$ , LR4/LR5  $-\hat{x}$ , UD4/UD5  $+\hat{z}$ . After the  $e^+$  are guided to the Ps apparatus, a pair of in-vacuum magnetic field coils (out of view) modify the trajectory within the apparatus (later discussed in Section 5.5).

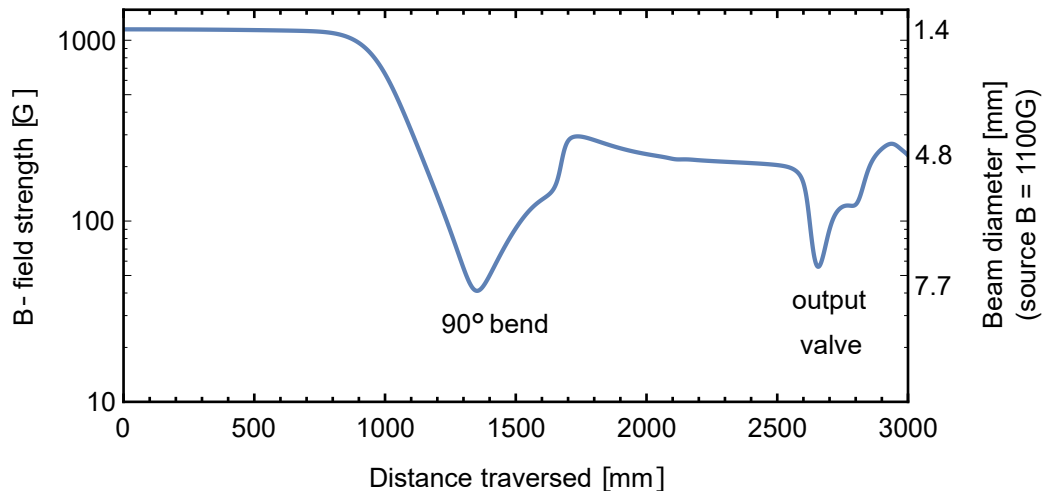


FIGURE 3.2: The magnetic field strength along the  $e^+$  trajectory shown on a logarithmic scale. The smallest magnetic field is within the spherical chamber where the  $90^\circ$  bend takes place. The magnetic field strength along the entire trajectory is sufficient to maintain a beam diameter that does not intersect with any chamber walls. The righthand axis represent the  $e^+$  beam diameter starting from the 1100 G magnetic field of the accumulator 2 m solenoid.

## 3.2 Transfer Detection and Optimization

A gate valve (identified as the “output valve”) located at the end of the 1 m-solenoid is used to isolate the buffer-gas accumulator from the Ps apparatus and for diagnostics of the  $e^+$  transfer efficiency. A gamma detector located 13.5 cm away from the output valve center (identical to the setup at the input valve) detects gamma rays from  $e^+$  that annihilate on the valve. With the buffer-gas trap electrodes set to 0 V, the moderated beam (at energies ranging from 10 eV to 40 eV) has been guided through the accumulator, around the bend, and onto the output valve with 100 % efficiency. The continuous annihilation detection of the moderated beam is used to quickly optimize the magnetic fields settings for guiding the moderated, ramped, and pulsed beam.

The moderated, ramped, and pulsed  $e^+$  beams follow a similar trajectory if they have a common kinetic energy and if the moderated beam traverses near the center of the  $e^+$  trap electrode. The trapped  $e^+$  follow the magnetic field line that connects to the trap electrode center, so the moderated beam trajectory has to be manipulated to traverse the center. This condition is achieved with

measurements from the plasma imaging system. By noting the center position that the pulsed plasma is imaged on the phosphor screen, the moderated beam is aligned to the same position using correction magnets before the trap location. Since the magnetic fields at the trap and beyond are identical, the moderated beam follows the same trajectory as the ramped and pulsed beam through the transfer guide and Ps apparatus.

As discussed in Section 2.3.2, the moderated beam profile in standard operating conditions has a toroidal radial profile. The profile is large in diameter and provides challenges to align the beam to the location of the pulsed plasma on the phosphor screen. To account for this, a reduction of the source Helmholtz coils current by 55 % reduces the beam size measured at the phosphor screen as expected. The size reduction is due to the conservation of the  $e^+$  magnetic dipole moment, where the radius scales as

$$r' = r_o \sqrt{\frac{B_o}{B'}} \quad (3.1)$$

and a  $\sim 30\%$  reduction is expected. The local magnetic field at the source also modifies the radial distribution of the moderated beam. By lowering the source field, the moderated beam radial profile approaches a Gaussian distribution at the expense of the beam intensity. The CCD image of the Gaussian beam is shown in Figure 3.3 and the change in the spatial profile from the toroidal beam is shown in the pair of 1D diametric slices.

The Gaussian profile also has advantages for optimizing the steering through apertures in the Ps apparatus. Additional details of the Ps apparatus are discussed in Chapter 5. An optimization algorithm measures the annihilation gamma rate beyond the apertures, and optimizes the magnet coil settings to maximize the rate. The toroidal beam is larger than the apertures such that the beam is clipped. The algorithm scans the beam across the apertures in the X and Y direction, and permits the region with the largest intensity. From Figure 3.3, it can be seen that the toroidal moderated beam has two local maxima in X and Y, and they are

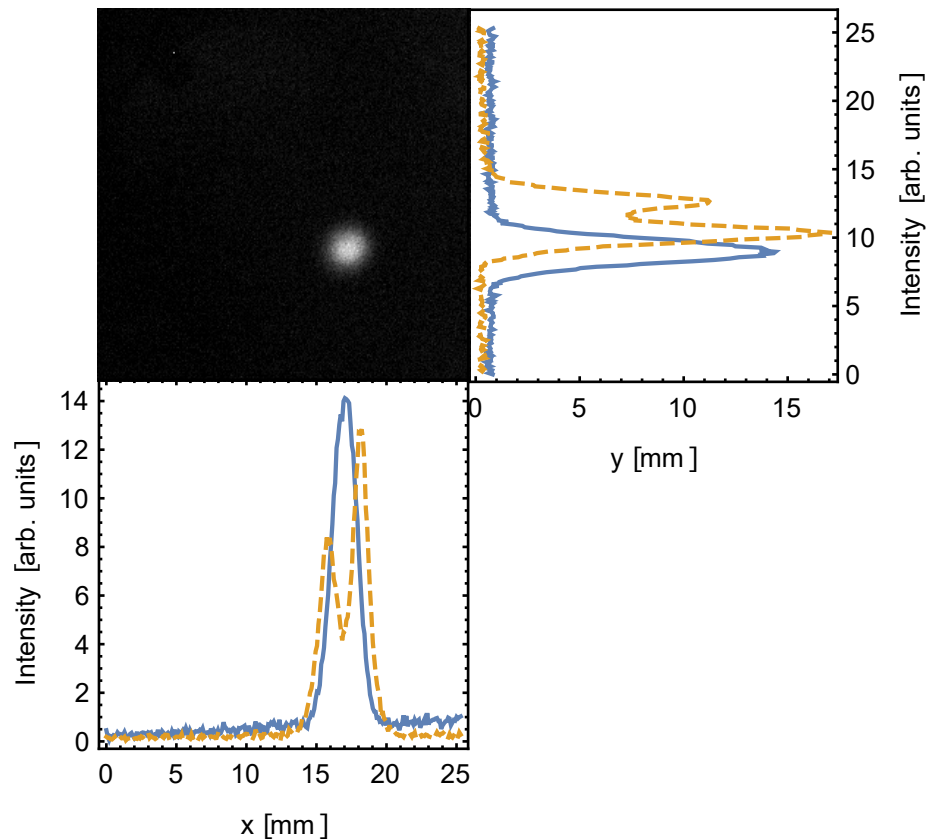


FIGURE 3.3: An image of the moderated  $e^+$  beam at a reduced source magnetic field strength with XY profiles. The toroidal distribution (dashed, orange) changes to a Gaussian distribution (solid, blue) when the source magnetic field strength is reduced by 55%.

radially offset from the actual beam center. This leads to an optimized magnet coil setting that does not center the overall beam through the apertures. Using the Gaussian beam eliminates this issue, where there is a global maximum along X and Y, and it represents the true center of the beam.

### 3.3 Ramped $e^+$ Beam Energy Distribution

The energy distribution of the ramped  $e^+$  is measured with a different approach than the moderated beam (discussed in Section 2.5.2). The gamma detector output is connected to a 2-channel digitizer (Agilent L4532A) that samples at 20 MSa/s and triggers the acquisition based on a rising-edge threshold of the input signal. The second channel is connected to the voltage monitor on the ramped

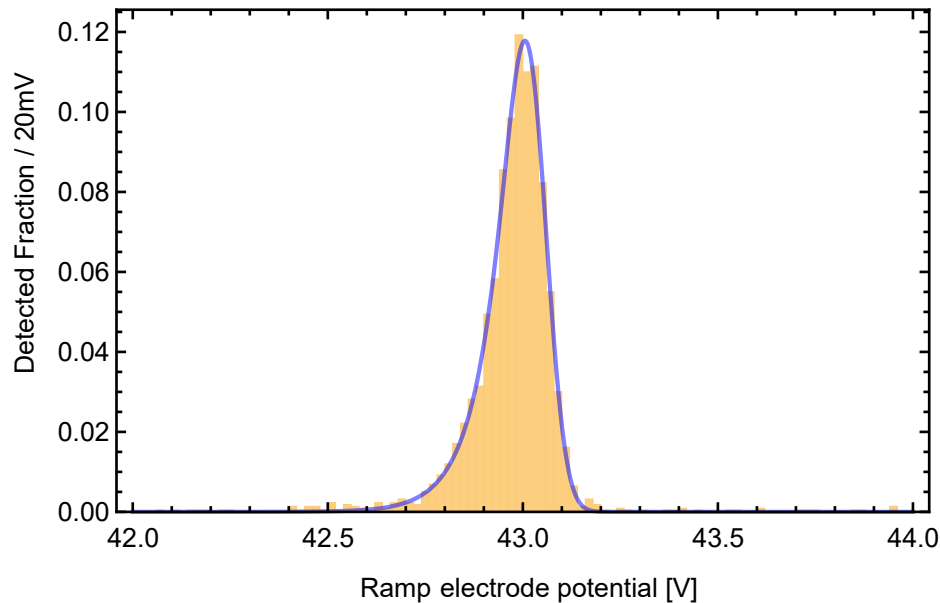


FIGURE 3.4: The detected fraction of gamma rays as the C2 electrode is ramped beyond the 42.7 V barrier. The number of gamma rays detected are binned in 20 mV increments, and the total count is normalized to unity.

electrode C2, where the  $e^+$  are held. As the C2 electrode voltage is ramped beyond the three-electrode long exit barrier potential, the most energetic  $e^+$  leak over the barrier followed by the cooler  $e^+$ . These  $e^+$  are guided towards the output valve and the single-event annihilations are digitized along with the C2 voltage, timestamped relative to the start of the ramp. By binning the timestamp distribution of the triggers, the time that  $e^+$  are released from the trap can be studied. By binning the distribution of the ramp electrode voltages, the amount of  $e^+$  released per Volt contains the energy distribution information.

An example of the voltage distribution for a 42.7 V applied barrier is shown in Figure 3.4, with the C2 voltage ramped from 36 V to 47 V. The majority of the  $e^+$  overcome the barrier at  $\sim 43$  V as expected. The distribution is fit to an EMG distribution, where the fit has a full width at half maximum of 200 mV that also corresponds with a parallel energy width of 200 meV. The broad width compared to the expected  $\sim 25$  meV is due to heating mechanisms during the dynamic ramp. A detailed study of the dynamics of the ejection of  $e^+$  plasmas from a PM trap was conducted by Surko *et al* showed that narrow parallel spreads can be achieved with slow ramp rates, a long exit potential barrier length, and a short well length

[65].

For this charge-exchange experiment, the 200 meV  $e^+$  energy distribution is well matched to the random momentum distribution of the Rydberg  $e^-$  in the Cs atom. The typical speed of the Rydberg  $e^-$  is  $v_e \approx 120\,000$  m/s. A 200 meV spread in energy corresponds to an approximate speed spread of  $\sigma_v \approx 270\,000$  m/s. A normal distribution characterized by a width of  $\sigma_v$ , integrated from  $-v_e$  to  $v_e$  has a significant coverage, where  $\sim 30\%$  of the  $e^+$  can charge-exchange.

# Chapter 4

## Laser Systems

A schematic of the laser system is shown in Figure 4.1, where the 852 nm distributed Bragg reflector (DBR) laser is locked with a sub-Doppler dichroic atomic vapour laser lock (SD-DAVLL). This laser drives the  $6S_{1/2}(F = 4) \rightarrow 6P_{3/2}(F' = 5)$  transition. The 520 nm extended cavity diode laser (ECDL) is frequency stabilized by an electromagnetically induced transparency (EIT) signal. This is the Rydberg-excitation laser that drives the  $6P_{3/2}(F' = 5) \rightarrow nD_{5/2}(F'' = 4, 5, 6)$  transition. A discussion of the locking methods is described in the following sections.

### 4.1 852 nm Laser System

The 852 nm laser system is shown in the top section of Figure 4.1. The diode (Photodigm PH852DBR) outputs up to 120 mW of power, but is attenuated by neutral density filters since it provides an abundant quantity than needed. After attenuation,  $\sim 10$  mW is used for frequency stabilization and about 0.1 mW is sent towards the experiment. The temperature and current of the diode are controlled and stabilized by a Melles-Griot 06DLD203 precision diode driver. A Faraday isolator (Thorlabs IO-5-850-VLP) is placed at the output of the diode

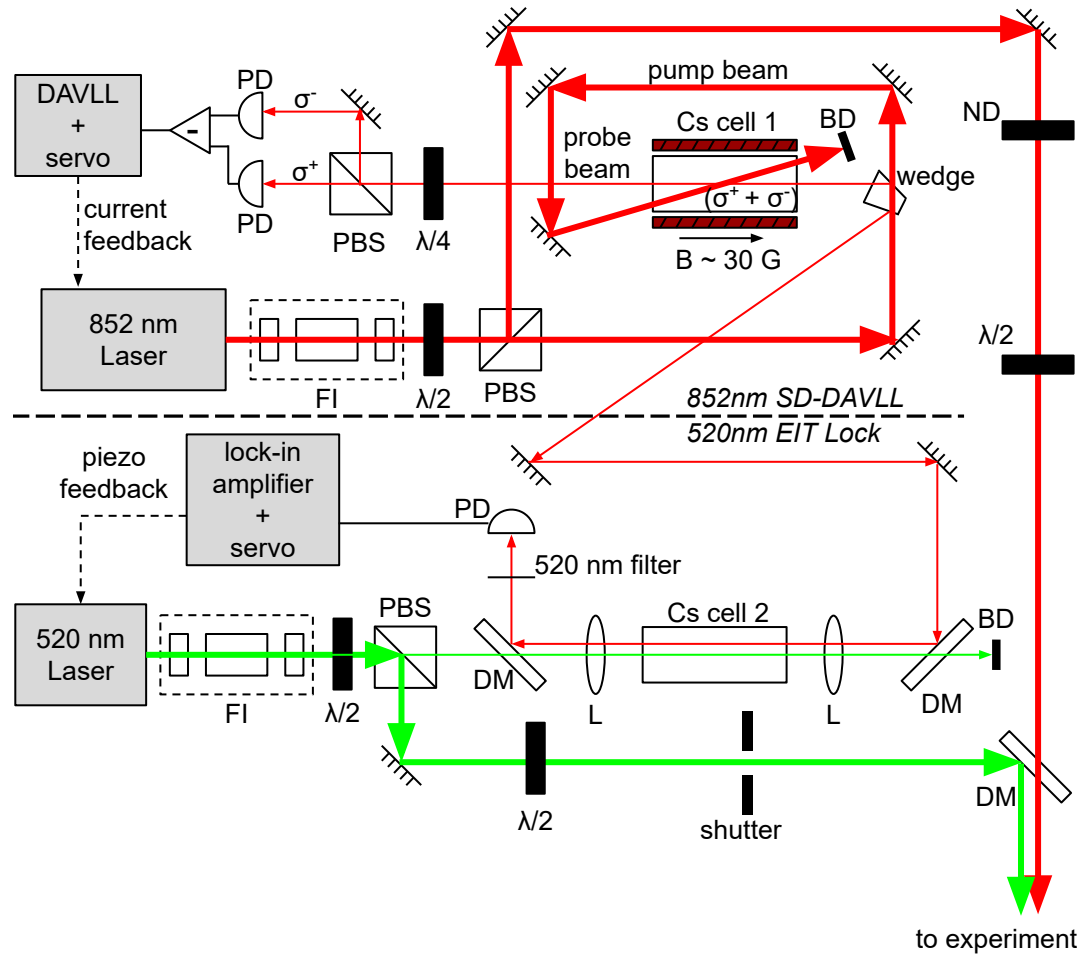


FIGURE 4.1: An overview of the laser locking system for the 852 nm and 520 nm lasers. The 852 nm laser is frequency-stabilized with a sub-Doppler dichroic-atomic-vapour-laser-lock (SD-DAVLL) method. A small fraction of the 852 nm laser power is used to generate an electromagnetically induced transparency (EIT) signal to frequency-stabilize the Rydberg-excitation laser. FI: Faraday isolator,  $\lambda/2$ : half-waveplate,  $\lambda/4$ : quarter-waveplate, PD: photodiode, DM: dichroic mirror, PBS: polarizing beam splitting cube, L: lens, BD: beam dump, ND: neutral density filter.

to protect the diode from back-reflections with  $>35$  dB of attenuation. A combination of a  $\lambda/2$ -waveplate and a polarizing beam splitting cube (PBS) is used to divide the laser power, where the transmitted portion (to laser locking) is linearly polarized in the horizontal direction, and the reflected portion (to experiment) is linearly polarized in the vertical direction. The laser is frequency stabilized with a sub-Doppler dichroic-absorption-vapour-laser-lock (SD-DAVLL) technique that provides a wide capture range without frequency modulation [66].

The foundation for SD-DAVLL is a typical saturated absorption spectroscopy

(SAS) setup, where the laser power is split into a high-power pump beam and a low-power probe beam and counter-propagate in a Cs vapour cell. A solenoid around the vapour cell generates a uniform magnetic field along the axis of the laser beams and lifts the degeneracy of the  $m$  magnetic sub-levels of the Cs atoms. The magnetic field defines the quantization axis for the Cs atoms, where linear polarization along the quantization axis is an equal combination of  $\sigma^+$  and  $\sigma^-$  circular polarization. The  $\sigma^+$  polarization drives  $\Delta m = +1$  transitions and the  $\sigma^-$  drives  $\Delta m = -1$  transitions. The Zeeman shift due to the magnetic field  $B$  shifts the transition energy by

$$\Delta E = h\Delta\nu = \pm g\mu_B B \quad (4.1)$$

where  $h$  is the Planck constant,  $\Delta\nu$  is the frequency shift,  $g$  is the Landé  $g$ -factor and  $\mu_B$  is the Bohr magneton. When the laser frequency is on resonance with a  $6S_{1/2}(F = 3, 4) \rightarrow 6P_{3/2}(F' = 3, 4, 5)$  hyperfine transition, the pump beam saturates the transition ( $I_{pump} \gg (I_{sat} = 2.7 \text{ mW/cm}^2)$ ) and the probe beam transmits through the vapour cell. A  $\lambda/4$ -waveplate and polarizing beam splitting cube separates the opposite-handed circular polarization components of the probe beam, and the components are detected on a subtraction photodiode system. A scan of the laser frequency below and above resonance generates a dispersion (error) signal with a zero-crossing at the atomic resonance in zero magnetic field. This error signal is used to provide feedback current corrections to stabilize the laser frequency to the atomic resonance. A proportional-integral (PI) controller based on a LabJack U3 device and LabVIEW provides corrections every 0.1 s and can lock the laser for week-long time scales.

The laser is capable of scanning over all  $6S_{1/2} \rightarrow 6P_{3/2}$  hyperfine transitions by simply tuning the diode current. A scan of the Doppler-free spectrum in zero magnetic field for the  $F = 4 \rightarrow F' = 3, 4, 5$  transitions are shown in Figure 4.2. It is locked to the  $F = 4 \rightarrow F' = 5$  cycling transition since it has the largest dipole moment and the Cs atoms cannot be optically pumped into the  $F = 3$  ground state.

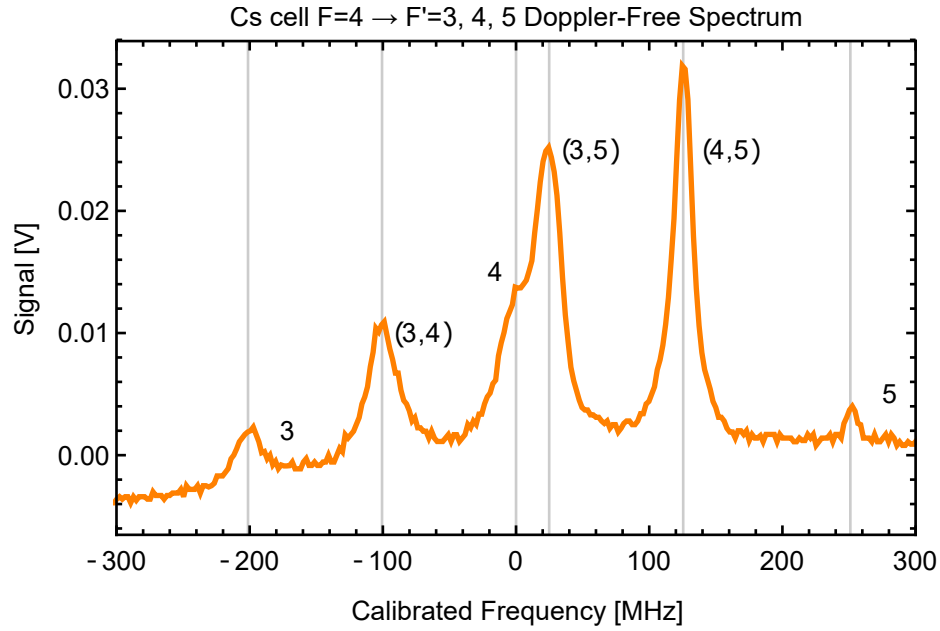


FIGURE 4.2: The Doppler-free spectrum within a vapour cell. The frequency axis is calibrated to known energy splittings and the zero is referenced to the  $F = 4 \rightarrow F' = 4$  transition. The labels denote the  $F'$  state and the enclosed in parentheses correspond to cross-over transitions.

## 4.2 Rydberg-Excitation Laser System

The Rydberg-excitation laser system is shown in the bottom section of Figure 4.1. The laser is an ECDL (Sacher Lasertechnik Lynx) in a Littrow configuration. The diode outputs between 513–520 nm onto a diffraction grating, where the first-order diffraction is seeded back into the diode for a narrow wavelength selection. The selected wavelength is tuned by the angle of the diffraction grating, which can be precisely controlled by a piezoelectric transducer. The diode current, temperature, and piezo voltage are controlled by a Sacher PilotPZ 500 controller. Up to 10 mW of laser power is available after wavelength-selection. A Faraday isolator placed at the output of the laser head (Thorlabs IO-3-532-LP) provides 40 dB of attenuation against back-reflections to protect the diode. A combination of a half-waveplate and polarizing beam splitting cube splits the laser power for frequency stabilization (2 mW) and the experiment (8 mW).

The laser is frequency stabilized to a  $6P_{3/2} \rightarrow nD_{5/2}$  transition by implementing a ladder-type electromagnetically induced transparency (EIT) setup. EIT is a

non-linear optics process within a 3-level system due to a quantum interference effect [67]. A probe beam addresses the ground state to intermediate state,  $|1\rangle \rightarrow |2\rangle$ , transition. A coupling beam addresses the intermediate to Rydberg state transition,  $|2\rangle \rightarrow |3\rangle$ . To obtain an EIT signal, the condition

$$\Omega_p \ll \Omega_c \quad (4.2)$$

is satisfied where  $\Omega_p$  is the Rabi frequency of the probe beam, and  $\Omega_c$  is the Rabi frequency of the coupling beam. The Rabi frequency is proportional to the intensity of the laser. When the condition is satisfied, the state  $|2\rangle$  becomes transparent to the probe beam, where an increased probe transmission can be detected. For this setup, the 852 nm beam is the probe beam, and the 520 nm beam is the coupling beam. The beams are counter-propagated through a Cs vapour cell, and the transmission of the probe beam is monitored on a photodiode.

A small amount of 520 nm laser power ( $\sim 2$  mW) is transmitted through the polarizing beam splitting cube with a 1 mm diameter. A minimal amount of 852 nm power ( $\sim 5$   $\mu$ W) is picked off from the glass wedge in the DAVLL system with a 1 mm diameter. A Cs vapour cell (cell 2) is placed between a pair of  $f = 15$  cm lenses separated by 30 cm. The two beams are overlapped and counter-propagated through the vapour cell using a long-pass dichroic mirror as shown in Figure 4.1. The lenses focus the laser beams at the center of the cell to maximize the intensity of the coupling beam. At the focus, the 852 nm beam waist is approximately 50  $\mu$ m and the 520 nm beam waist is 30  $\mu$ m. This corresponds to a probe Rabi frequency,  $\Omega_p = 2\pi \times 30$  MHz, and a coupling Rabi frequency,  $\Omega_c = 2\pi \times 40$  MHz. The transmitted probe beam is separated from the coupling beam with a short-pass dichroic mirror and is collected onto a photodiode. Figure 4.3 shows a simultaneous scan of the EIT resonance and SAS signal through vapour cells 1 and 2. The 852 nm laser is scanned over the  $F = 4 \rightarrow F' = 3 - 5$  transitions while the Rydberg-excitation laser is tuned to drive a  $6P_{3/2}(F' = 5) \rightarrow nD_{5/2}$  transition. The EIT scan shows the Doppler-broadened absorption, with a narrow transmission aligned to the SAS  $F = 4 \rightarrow F' = 5$  hyperfine transition. Note that the resonances are not

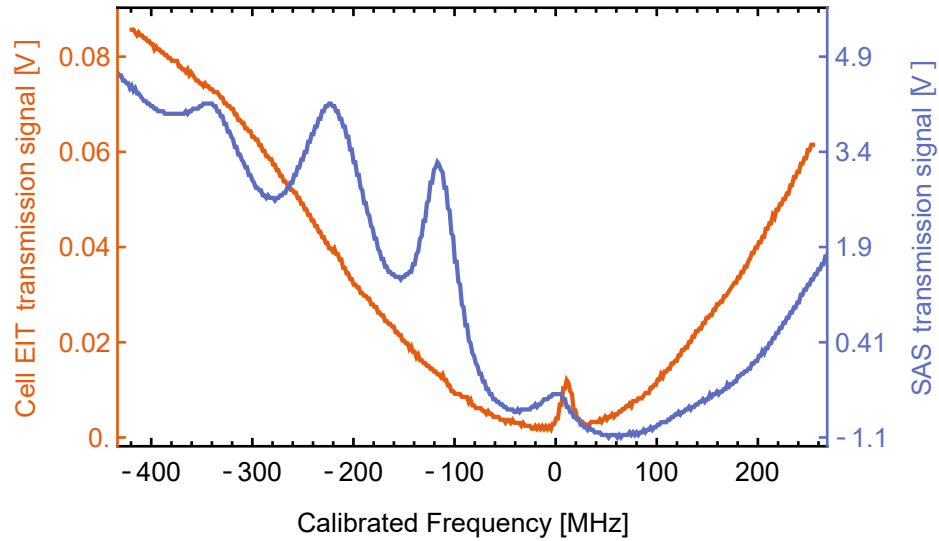


FIGURE 4.3: The electromagnetically induced transparency (EIT) signal produced with the Rydberg-excitation laser resonant with a  $6P_{3/2}(F' = 5) \rightarrow nD_{5/2}$  transition while the 852 nm laser is scanned over  $F = 4 \rightarrow F' = 3 - 5$  spectrum (shown in red). The frequency axis is calibrated to a simultaneous saturated absorption spectroscopy (SAS) scan of the  $D_2$ -line hyperfine transitions (shown in blue).

precisely aligned due to the Rydberg-excitation laser operating in a free-running mode, therefore laser frequency drifts are not corrected.

With the 852 nm laser system locked to the  $6S_{1/2}(F = 4) \rightarrow 6P_{3/2}(F' = 5)$  transition, the laser communicates with Cs atoms in the  $v = 0$  m/s velocity group along the beam direction. As the 520 nm laser frequency is tuned across a Rydberg transition, this velocity group of Cs atoms is excited to the Rydberg state and an EIT resonance signal is observed from the increased transmission of the 852 nm probe beam.

The 520 nm laser is frequency stabilized to the EIT signal by a standard technique using a lock-in amplifier and frequency modulation [68]. The frequency of the 520 nm laser is dithered by a small amount relative to the width of the Lorentzian resonance. The dither is produced by a 1 kHz sinusoidal voltage capacitively coupled to the DC voltage applied to the piezo. The EIT signal is the signal input of the lock-in amplifier (SRS SR830), and the reference signal is the piezo dither. The lock-in amplifier uses phase-sensitive detection to extract the EIT signal at the reference frequency and a particular phase. When the 520 nm laser frequency

is scanned across the EIT resonance, the lock-in output is proportional to the derivative of the curve. This results in a dispersion signal with a zero-crossing at the center of the resonance. The phase of the lock-in amplifier is set to maximize the amplitude of the output.

This dispersion signal provides an error feedback correction to the DC piezo voltage to correct the laser frequency to the Rydberg resonance. A PI-loop based on a LabJack U3 device and LabVIEW reads the lock-in output and provides corrections to the DC piezo voltage every 0.5 s. The laser is locked to the  $6P_{3/2} \rightarrow 18D_{5/2}$  with a wavelength of 520.3 nm, measured on a wavemeter (Burleigh Wavemeter Jr WA-2000).

Fluorescence from the decay of the Rydberg state can be visibly seen from the vapour cell as shown in Figure 4.4. A spectrum of discrete wavelengths is present due to the multiple pathways that a Rydberg state can take to decay to the ground state. The dominant transition is the reverse process  $18D_{5/2} \rightarrow 6P_{3/2}$  which re-emits the 520 nm photon. Decays from  $18D_{5/2} \rightarrow 7P_{3/2}$  is the next most-probable transition, which can be detected from the emission of a blue 455 nm photon from the  $7P_{3/2} \rightarrow 6S_{1/2}$  decay. Collisional processes between Cs atoms in the vapour cell and the presence of Cs ions cause a redistribution of the Rydberg states to nearby  $n$ -states with a mixture of  $l$ -states [69]. Red fluorescence is observed from  $nF_j/nP_j \rightarrow 5D_j$  decays due to  $n, l$ -changing collisions. A study of the fluorescence spectrum is shown in Ref. [70] shows the mixture of Rydberg states after excitation to the  $21S_{1/2}$  state.

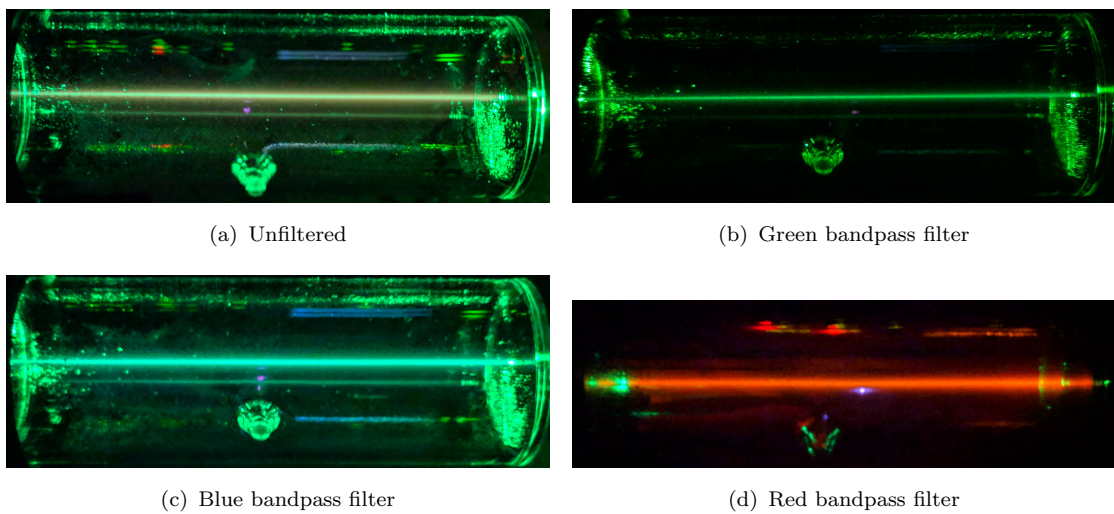


FIGURE 4.4: Fluorescence of  $\text{Cs}^*$  atoms in a vapour cell viewed through various colour (bandpass) filters. A discrete spectrum is observed due to multiple decay paths to the ground state.

# Chapter 5

## Positronium Experimental System

The previous chapters discussed the formation of different types of  $e^+$  beams and the magnetic transfer guide to adiabatically transfer the  $e^+$  up to the output valve. Beyond the output valve is the Ps apparatus. The apparatus to produce Ps\* atoms by charge-exchange with laser-excited Cs\* is described in detail.

### 5.1 Ps Apparatus Vacuum System

The Ps apparatus vacuum system is isolated from the buffer-gas accumulator with the output valve. A bellows immediately after the output isolates the Ps apparatus from mechanical vibrations due to the accumulator cryopumps. The chamber is pumped by a turbomolecular pump (Agilent Varian Twisstorr FS84), which is backed by a scroll pump (Agilent Varian SH110). The system contains a liquid nitrogen dewar that is insulated by the surrounding vacuum and also acts as a 77 K cryopump. The liquid nitrogen dewar cools several components to capture Cs emitted from the thermal Cs oven. A cold trap surrounds the Cs oven nozzle to collect the majority of the atoms. The base pressure in the system is maintained

at  $3 \times 10^{-9}$  Torr. During  $e^+$  accumulations, the output valve is shut during the loading stage to minimize the amount of nitrogen buffer-gas entering the system.

## 5.2 Cesium Oven

The Cs oven emits a thermal beam of ground state Cs atoms where the emission rate is dependent on the temperature of the liquid reservoir of Cs. A diagram of the system is shown in Figure 5.1. It is mounted to the vacuum system through a ceramic electrical isolator and a bellows. The isolation of the oven from the grounded vacuum allows a positive electric potential to be applied, slowing the  $e^+$  at the charge-exchange location. The bellows is used to adjust the height of the oven and for adjustment of the tilt. The oven is suspended within the vacuum chamber, with the nozzle centered within the cold trap. Liquid Cs is fed into the reservoir by a 48 cm long, 4.5 mm inner diameter stainless steel tube that is vertically orientated and heated to 70 °C.

The oven is composed of a stainless steel reservoir that contains 25 g of liquid Cs and a downward-directed nozzle from which the vapour of atoms are emitted. Figure 5.2 shows the cross-section of the oven depicting the liquid Cs reservoir and the path for Cs vapour to travel towards the nozzle. The nozzle has a  $D = 1$  mm diameter and  $L = 3$  mm length that also acts as a pumping restriction. A metal “cage” surrounding the output of the nozzle modifies the electric potential to be more uniform at the charge-exchange position and to provide  $e^+$  and laser access. Heat is applied to various locations on the oven with Lakeshore HTR-50 cartridge heaters, where each heater can provide up to 50 W of power to distribute heat around the reservoir and nozzle. The temperatures at several locations are monitored with type T thermocouples that are insulated with low-outgassing ceramic beads. The oven is typically operated with the nozzle held at a higher temperature than the reservoir such that Cs vapour does not condense in the nozzle.

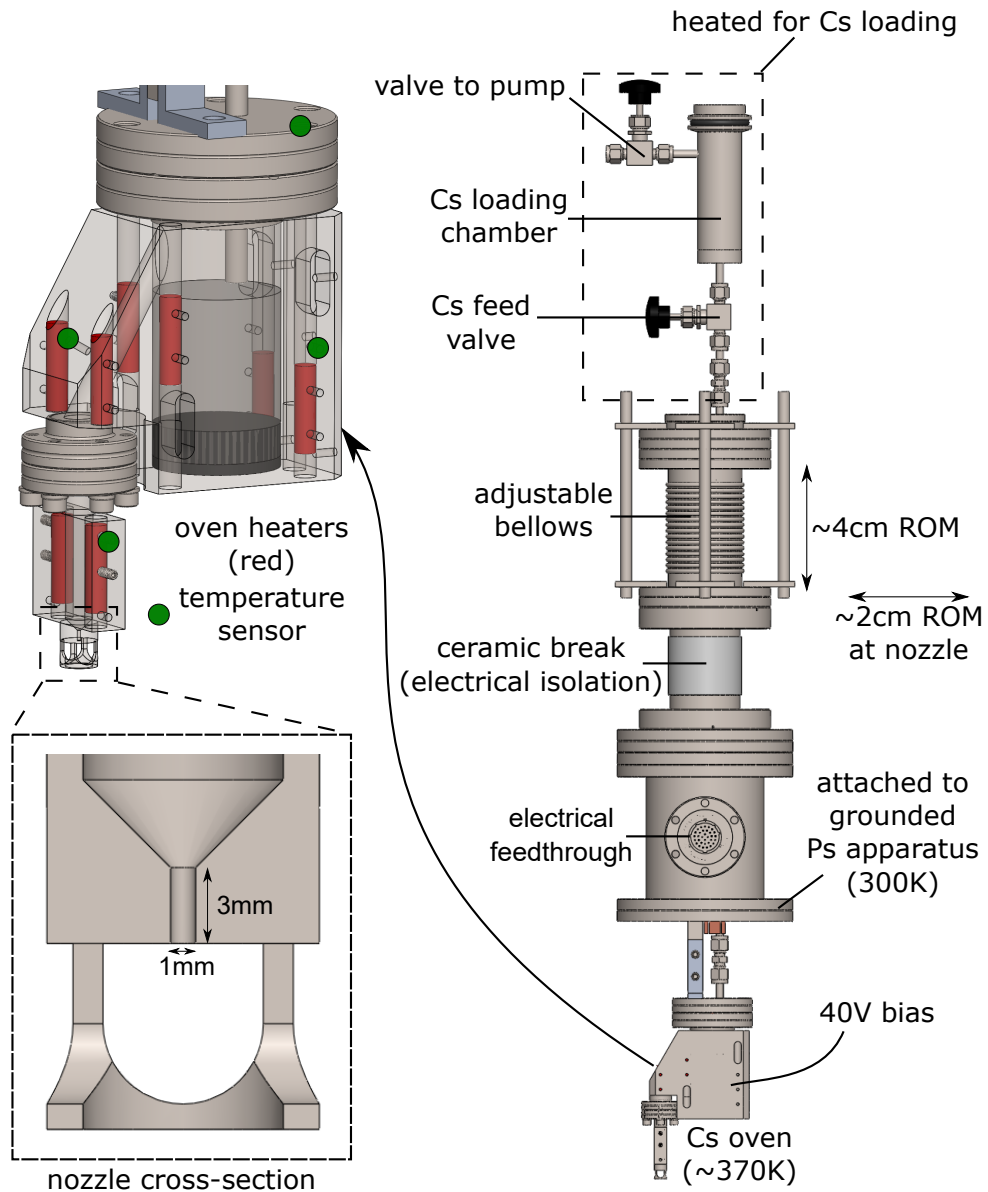


FIGURE 5.1: A diagram of the Cs oven, a cross-sectional view of the nozzle and the location of the cartridge heaters and temperature sensors. A 25 g ampoule of Cs drains from the loading chamber, flows through a heated stainless steel tube into the Cs oven reservoir. A bellows provides up/down, forward/backward, and side-to-side range of motion (ROM) for the oven. The ceramic break provides electrical isolation to bias the oven and nozzle for slowing  $e^+$ . The electrical feedthrough provides connections to the cartridge heaters and thermocouples. For a larger view of the Cs nozzle, see Figure 1.2.

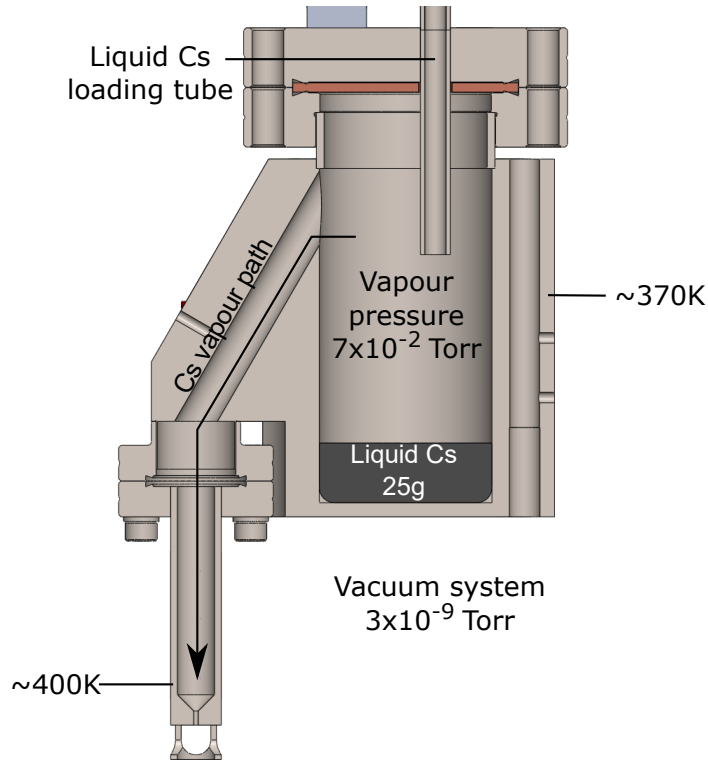


FIGURE 5.2: A cross-section view of the oven and nozzle showing the liquid Cs loading tube, liquid Cs reservoir and vapour path. The liquid Cs is fed through the liquid Cs loading tube and accumulates in the reservoir. The oven is held at  $\sim 370$  K, producing a Cs vapour pressure of  $7 \times 10^{-2}$  Torr. The Cs vapour atom travel through a path and exit the  $\sim 400$  K nozzle. The Cs atoms enter the vacuum system that is maintained at  $3 \times 10^{-9}$  Torr.

Cs has a low melting point of  $25^\circ\text{C}$  and produces a large vapour pressure dependent on the temperature (see Figure 5.3). In the liquid phase, the vapour pressure dependency on the temperature follows the equation:

$$\log_{10} P_v = 8.22127 - \frac{4006.048}{T} - 0.00060194T - 0.19623 \log_{10} T \quad (5.1)$$

The oven operates in the molecular flow regime where the mean free path of the Cs,  $\lambda_l$ , is greater than the characteristic dimension of the nozzle tube,  $D = 1$  mm. The mean free path represents the average distance that an atom travels before a collision with another atom. The mean free path can be defined as

$$\lambda_l = \frac{k_B T}{\sqrt{2} \pi d_{Cs}^2 p} \quad (5.2)$$

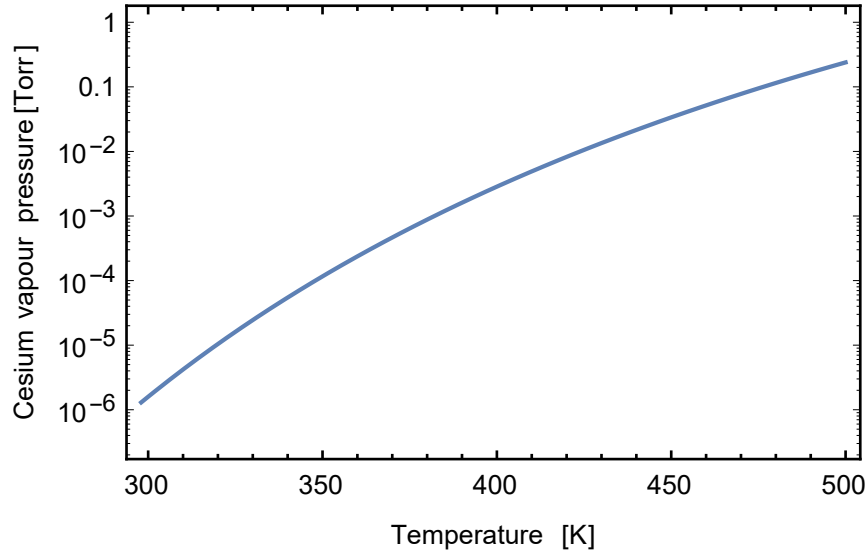


FIGURE 5.3: The vapour pressure of liquid Cs as a function of temperature. This is the expected pressure of vapour Cs in the oven based on the oven temperature.

where  $k_B$  is the Boltzmann constant,  $T$  is the oven temperature,  $d_{Cs}$  is the Cs atom diameter and  $p$  is the pressure. At a typical operating temperature of 400 K, the mean free path  $\sim 50$  mm. The Knudsen number define the flow regime,

$$Kn = \frac{\lambda_l}{D} \quad (5.3)$$

where  $Kn > 1$  represents molecular flow. From this estimate, the oven operates in the molecular flow regime where the Cs atoms travel in straight line trajectories through the tube or collide with the wall, and flow independently from other atoms.

The angular distribution of the emitted Cs is dependent on the tube dimensions and scattering rate. In the limit of low scattering rate (molecular flow), the angular intensity of the beam is approximated by

$$j(\theta) = \begin{cases} \frac{2}{\pi} \cos(\theta) \left( \arccos(q) - q\sqrt{1-q^2} + \frac{2}{3q} \left( 1 - \sqrt{(1-q^2)^3} \right) \right), & \tan(\theta) < \frac{D}{L} \\ \frac{4 \cos(\theta)}{3\pi q}, & \tan(\theta) \geq \frac{D}{L} \end{cases} \quad (5.4)$$

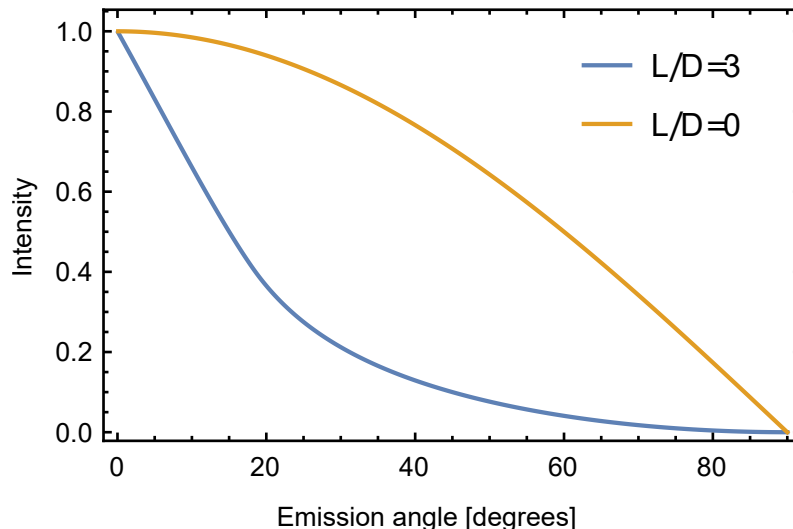


FIGURE 5.4: The angular distribution of the emitted Cs. The intensity is shown for the  $L/D = 3$  nozzle tube geometry (blue). The cosine distribution for  $L/D = 0$  (orange) for  $L/D = 0$  is shown for reference.

where  $q(\theta) = \frac{L}{D} \tan(\theta)$ ,  $\tan(\theta) < \frac{D}{L}$  is the contribution from atoms that travel straight through the tube, and  $\tan(\theta) \geq \frac{D}{L}$  is the contribution from atoms that scatter from the walls [71]. In the limit of  $L/D \rightarrow 0$ , the distribution converges towards Knudsen's cosine emitter distribution for a thin-walled orifice. The distribution for the geometry used in the nozzle  $L/D = 3$ , the distribution is shown Figure 5.2, where the angular FWHM is  $30^\circ$ . This produces a more forward-directed beam.

The flux of atoms emitted into a solid angle  $d\Omega$ , is represented by

$$I(\theta)d\Omega = \frac{nv_{avg}D^2}{16}j(\theta)d\Omega \quad (5.5)$$

where  $n$  is the Cs vapour density that is dependent on the oven temperature and  $v_{avg}$  is the average Cs speed. At 400 K, the oven liquid Cs reservoir produces a Cs vapour with number density  $n = 7 \times 10^{13}$  Cs/cm<sup>3</sup> and the atoms travel with an average speed of  $v_{avg} = 250$  m/s determined from the Maxwell-Boltzmann distribution. The amount of Cs emitted within the  $30^\circ$  FWHM angle is  $5 \times 10^{14}$  Cs/s under normal conditions.

## 5.3 Liquid Nitrogen-Cooled Components

### 5.3.1 Dewar

A home-built 13 L liquid nitrogen ( $\text{LN}_2$ ) dewar attached to the apparatus cools the Cs cold trap and apertures. Figure 5.5 shows the dewar that is mounted to a 10" Conflat vacuum flange by stainless steel standoffs. Cs emitted from the oven is deposited on cryogenic surfaces to minimize the vapour pressure and to trap Cs from migrating throughout the various vacuum systems. Cs is a highly-reactive, conductive metal that could potentially cause electrical shorts and insulating patches in critical components. Without the dewar, critical components such as the three-stage Penning trap electrodes would be at risk. The liquid nitrogen level is measured with an American Magnetics capacitance-based liquid level sensor in the dewar. The dewar is filled through a 1.27 cm diameter stainless steel tube located at the bottom which extends up, 77 cm, into the tank. Another tube extends 78 cm into the tank that acts as a vent for boil-off gas. The height of the vent tube also limits the maximum liquid level.

The liquid level is automatically refilled from a bulk 200 L liquid nitrogen tank. An American Magnetic Model 1700 Liquid Level Instrument auto-refills the dewar at programmed setpoints. The instrument opens an ASCO solenoid valve to flow liquid nitrogen into the dewar when the tank reaches the lower setpoint. The solenoid valve shuts when the level reaches the upper setpoint. The instrument is programmed to begin the fill when the level reaches 30 % and stops at 100 %. The auto-fills typically begin every 15 hours and requires user operations to change the 200 L tank every 6 days.

The dewar cools the bottom of an 87 cm long, 3.2 cm diameter copper rod thermally anchored to the bottom of the dewar and extends upwards through the center of the dewar. The cold components within the Ps apparatus are thermally connected to this copper bar. The top of the bar is designed to split the cooling along a low thermal conduction path to the cold trap where a majority of Cs is collected. A high thermal conduction path cools the large assembly that collects diffuse Cs

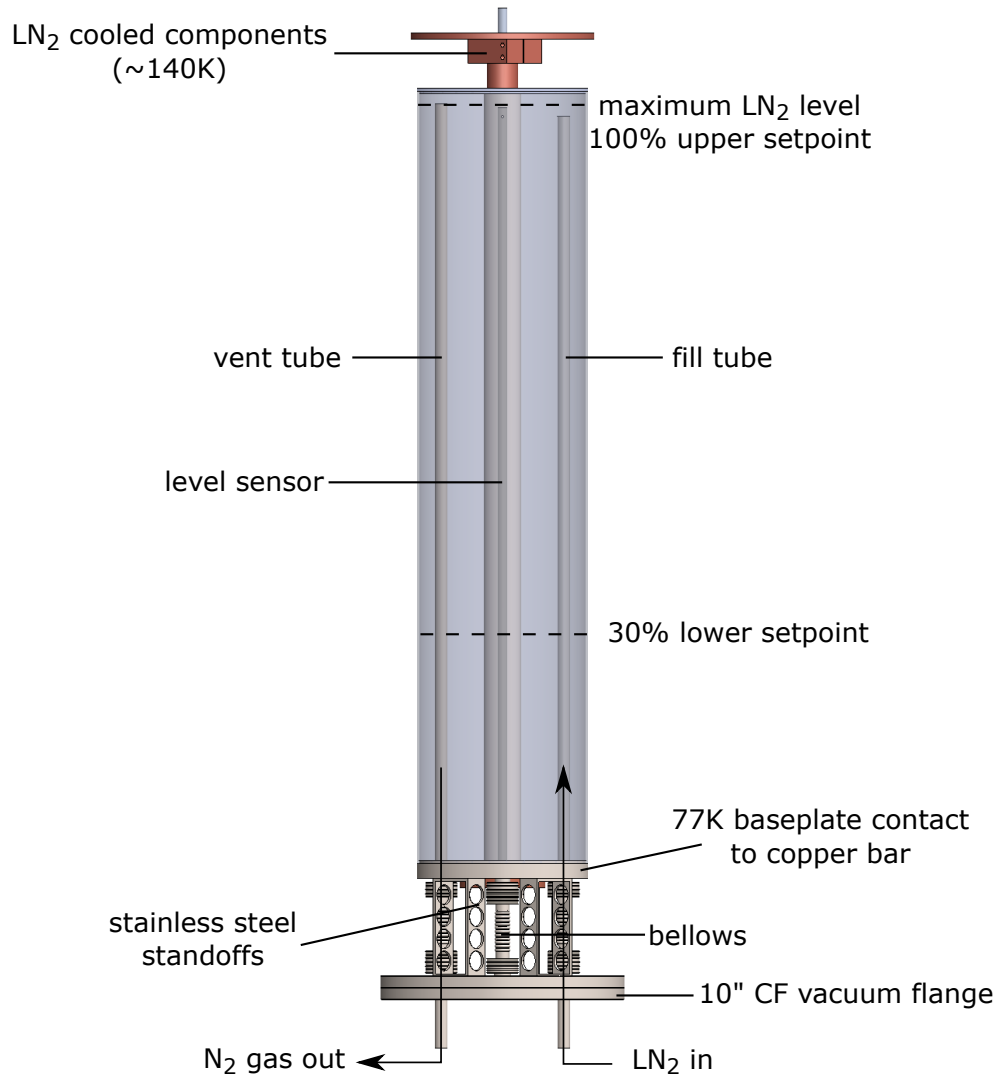


FIGURE 5.5: A diagram of the liquid nitrogen dewar system. The dewar is mounted to a 10" Conflat (CF) flange by stainless steel standoffs. The dewar contains two tubes that extend through the baseplate and flange where liquid nitrogen is filled, and boil-off gas is vented. The volume of liquid nitrogen is measured by a level sensor.

residuals. A 1.2 cm diameter, 2.54 cm deep bore is machined out of the top of the copper bar with a tapped hole at the bottom surface. A 1 cm diameter, 8.3 cm long aluminum post is connected here (see Figure 5.6). The poor thermal conduction path between the aluminum path and copper path allows for heat flowing down the aluminum to be drained into the copper bar instead of flowing into the copper path.

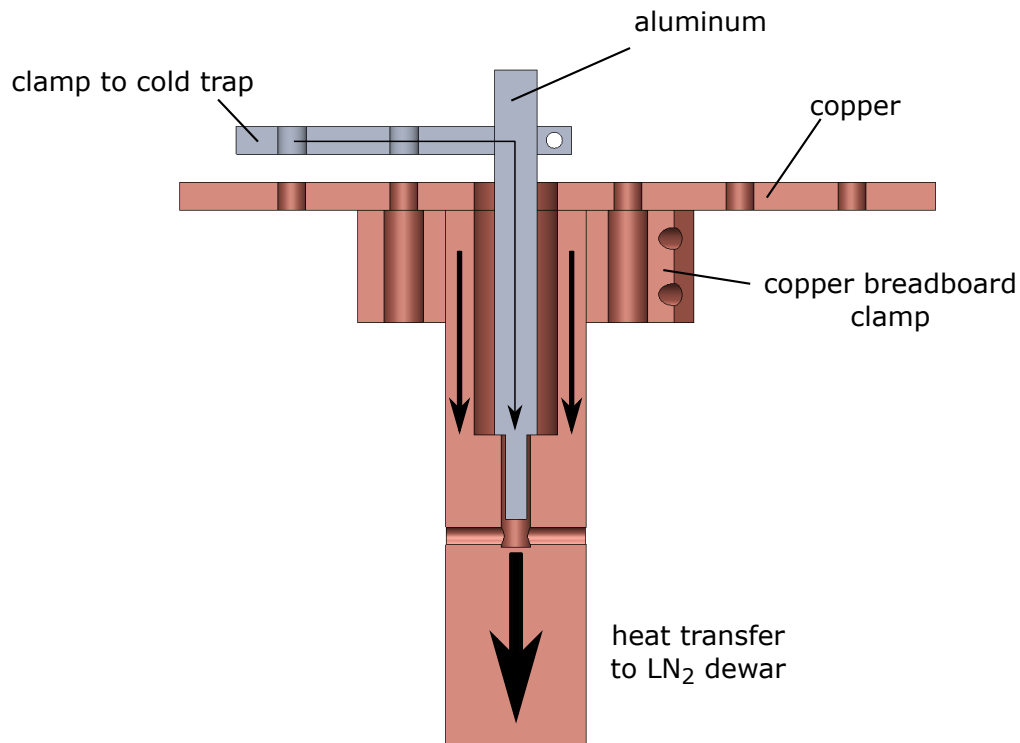


FIGURE 5.6: Heat transfer to the liquid nitrogen dewar from the aluminum thermal path and copper breadboard thermal path. The aluminum thermal path connects to the Cs cold trap and the copper breadboard thermal path connects to other components that capture residual Cs atoms. In the event that the cold trap is heated to room-temperature to drain the collected Cs, the copper breadboard components are not significantly affected due to the thermal isolation between the paths.

### 5.3.2 Cold Trap and Surrounding Components

The cold trap is a copper component designed to capture the majority of Cs atoms emitted from the oven. It has a 4 mm diameter hole for  $e^+$  to enter, and a 7.5 mm diameter hole for Ps to travel towards the detector region and electrostatic quadrupole. Two laser access holes of 9.5 mm in diameter are located on the sides. A 6.35 mm diameter copper tube at the bottom of the cold trap acts as a drain for liquid Cs. This allows for continuous maintained vacuum after the cold trap fills beyond 350 g of Cs. The cold trap is cooled to 140 K through the aluminum thermal connection to the dewar. The connection to the aluminum post is electrically isolated with insulating alumina oxide washers as an additional thermal restriction to evenly distribute the heat on the cold trap. The electrical isolation allows for biasing to tune the  $e^+$  kinetic energy that can enter the cold

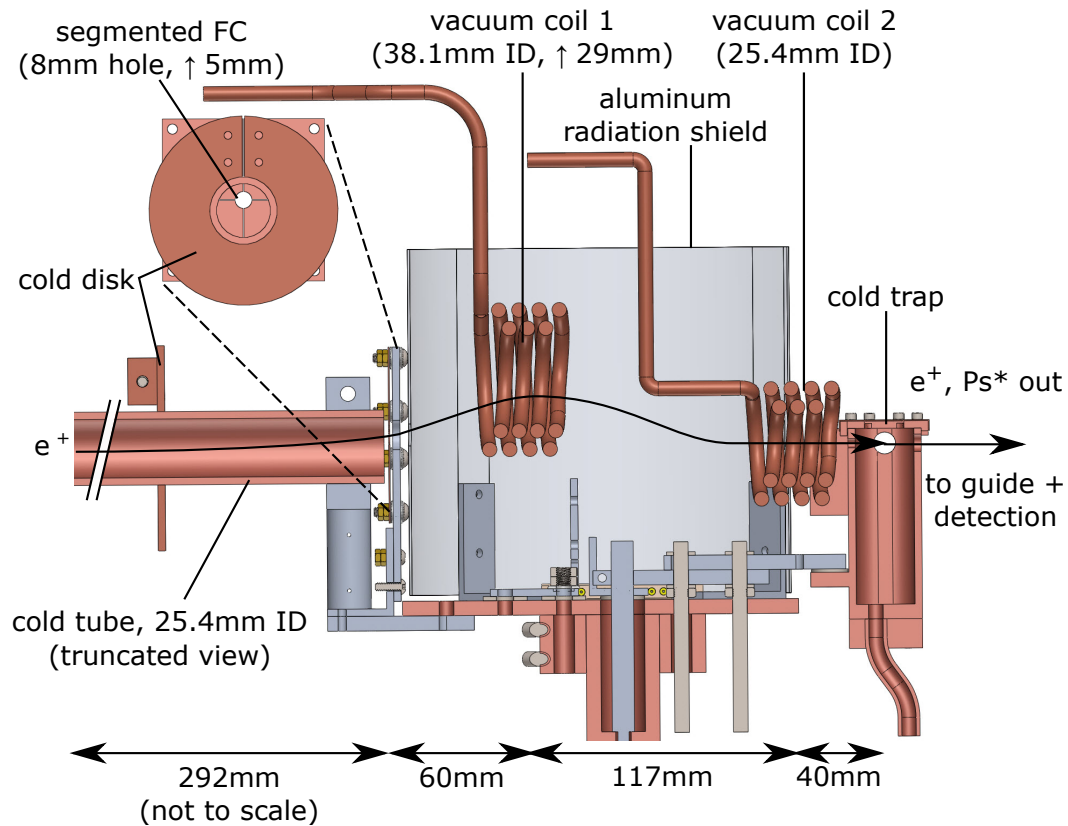


FIGURE 5.7: A cross-section view of the liquid nitrogen-cooled components. The cold tube is truncated in this view. The segmented Faraday cup (FC) is also shown from the perspective of the incident  $e^+$ . The diameters and vertical offsets are denoted for the cold tube, segmented FC, vacuum coil 1 and vacuum coil 2. The in-vacuum coils are at room temperature. The FC offset-hole acts a collimator to stop ballistic Cs from travelling towards the buffer-gas accumulator. The  $e^+$  are guided through the FC hole with magnetic fields generated by vacuum coils 1 and 2. Vacuum coil 2 re-centers the  $e^+$  to enter the cold trap where  $e^+$  can charge-exchange with Cs\* to produce Ps\*. A fraction of the Ps\* travel towards the guide and detection region. ID: inner diameter.

trap input hole, and for tuning the electric potential distribution in the cold trap and nozzle region. To empty the cold trap, heat can be applied to the cold trap with four Lakeshore HTR-50 cartridge heaters, while all other cold components remain cold and do not get affected due to the poor thermal connection. A test of this heating was performed prior to installing the Cs oven where the cold trap was warmed to 40 °C while the surrounding cold components temperature was raised by only 5 °C.

A copper breadboard is thermally connected to the better conducting path, directly by a clamp on the copper rod. The breadboard is tapped with 1/4"-20

holes to accommodate future apparatus expansion. The present system contains an aluminum outer shield near the vacuum chamber walls, a segmented Faraday cup system with an axially offset hole, and a copper tube extending towards the accumulator. These components are designed to capture stray Cs atoms that did not adsorb to the cold trap. The 8 mm hole on the segmented Faraday cup is offset from the axis by 5 mm such that there is no direct line of sight for the Cs to travel towards the accumulator without intersecting a cold surface.

## 5.4 Cesium Laser Excitation to Rydberg States

The 852 nm and Rydberg-excitation laser beams are overlapped and focused to a thin horizontal sheet at the charge-exchange location using a cylindrical lens system. The lasers are linearly polarized in the horizontal direction using half-waveplates. The lasers enter the vacuum chamber through an input laser window and intersect the thermal Cs beam at a right angle to minimize the Doppler shift. The detection of ground state Cs emitted from the nozzle is studied with laser spectroscopy. From laser spectroscopy, the hyperfine structure can be observed with broadening mechanisms, and the density of ground-state atoms can be studied as a function of the oven temperature. A fraction of the atoms that are populated in the first excited state is driven to the Rydberg state with the Rydberg-excitation laser, where spectroscopy of the Rydberg state is used to determine the density of Cs\* atoms that can charge-exchange. The Cs atoms absorb a fraction of the laser power, and the unabsorbed photons are transmitted. The transmission of the laser beams through the Cs beam exit the vacuum system through an output laser window. The 852 nm and  $\sim 520$  nm transmission laser beams are separated onto separate photodiodes using a dichroic mirror to monitor the absorption. The fluorescence from radiative decays is imaged with a CCD camera and some fluorescence is focused onto a photodiode to quantify the fluorescence.

### 5.4.1 $6S_{1/2}$ to $6P_{3/2}$ Excitation

#### 5.4.1.1 Laser absorption

The 852 nm sheet laser is aimed  $\sim 3$  mm below the nozzle. The transmission of the laser through the Cs beam is monitored on the photodiode while scanning the laser frequency. Figure 5.8 shows a scan of the laser absorption, scanned across the  $6S_{1/2}(F = 4) \rightarrow 6P_{3/2}(F' = 3, 4, 5)$  hyperfine transitions. The frequency axis is calibrated to the known splittings. The spectrum is fit to three Lorentzians with amplitudes scaled to the relative oscillator strengths. As it can be seen, the  $F = 4 \rightarrow F' = 5$  transition has the most absorption since it is a closed cycling-transition with the largest oscillator strength. The electric dipole selection rules allows for  $\Delta F = 0, \pm 1$  transitions. A Cs atom in the  $6P_{3/2}(F' = 5)$  state can only decay and repopulate the  $6S_{1/2}(F = 4)$  state, where the laser excitation can be repeated. However, a Cs atom in the  $6P_{3/2}(F' = 3, 4)$  state can radiatively decay to the  $6S_{1/2}(F = 3)$  state, becoming transparent to the laser frequency. There are a total of 16 ground state magnetic sublevels, with 9/16 in the  $F = 4$  manifold, and 7/16 are in the  $F = 3$  manifold. In the present system, only 56 % of the ground state atoms can be laser addressed, and at most 50 % of these states can be excited to the  $6P_{3/2}(F' = 5)$  state, a net efficiency of 28 %. To improve upon this in the future, a second 852 nm laser stabilized to the  $F = 3 \rightarrow F' = 4$  transition can be used to optically pump the atoms into the  $F = 4$  ground state, a net efficiency improvement of 50 %.

The observed transitions are Doppler-broadened due to the effusive distribution from the tubular nozzle. The natural linewidth of the transition is 5.2 MHz whereas the observed transition is  $\sim 200$  MHz broad. The Cs beam is emitted with a  $30^\circ$  angular FWHM (see Section 5.2). The Doppler broadened width for a gas that can move uniformly in all degrees of freedom (like in a vapour cell) is given by

$$\Delta\nu_D = 2\sqrt{\frac{2k_B T \ln 2}{mc^2}}\nu_o \quad (5.6)$$

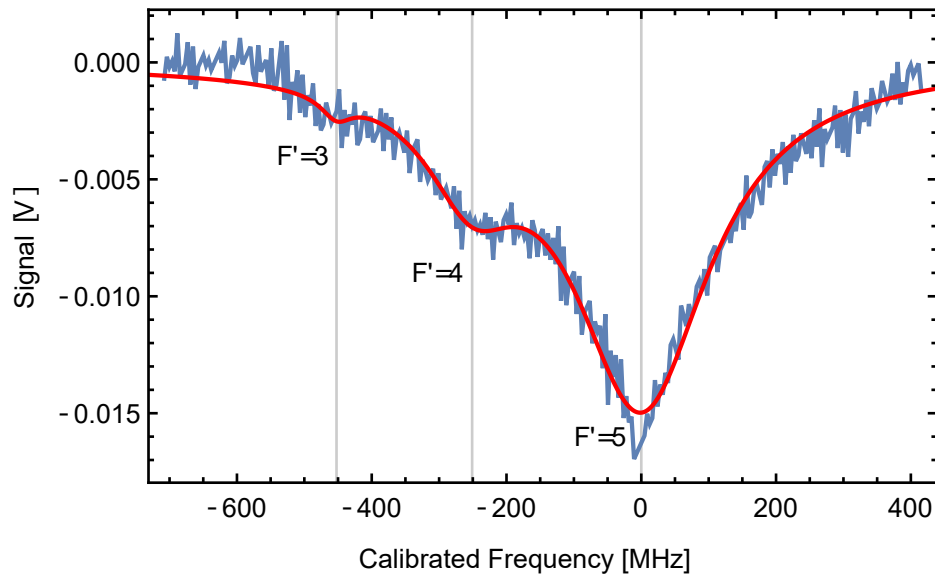


FIGURE 5.8: A laser absorption scan of the  $6S_{1/2}(F = 4) \rightarrow 6P_{3/2}(F' = 3, 4, 5)$  transitions in the ground state thermal Cs beam. The DC level of the signal is subtracted, and the data is fit to the sum of three Gaussian distributions. The frequency axis is calibrated to the known transition frequency difference for each transition. The frequency axis is referenced to the  $F = 4 \rightarrow F' = 5$  transition. The  $F = 4 \rightarrow F' = 5$  transition has the most absorption since it is a cycling transition.

At a temperature of 400 K, this corresponds to a width of approximately 400 MHz. A Monte-Carlo simulation of Cs atoms emitted in an angle following the probability distribution shown in Figure 5.4, with a speed governed by the Maxwell-Boltzmann (MB) distribution at 400 K was conducted to find the 1D speed distribution along the laser direction. The result is shown in Figure 5.9 along with the 1D MB distribution to show the narrowed velocity spread. The simulated data is fit to a Lorentzian with a FWHM of 140 m/s compared to 370 m/s for the 1D MB distribution. This corresponds to an effective temperature of  $T_{eff} = 230$  K along the laser direction and an effective Doppler width of 230 MHz, consistent with observations.

This broad width motivates transit-time broadening of the laser frequency to communicate with the largest fraction of atoms. For a Gaussian beam focused to a waist  $w_o$ , the transit-time broadening FWHM is

$$\Delta\nu_{transit} = \frac{\sqrt{2\ln(2)}}{\pi} \frac{v}{w_o} \quad (5.7)$$

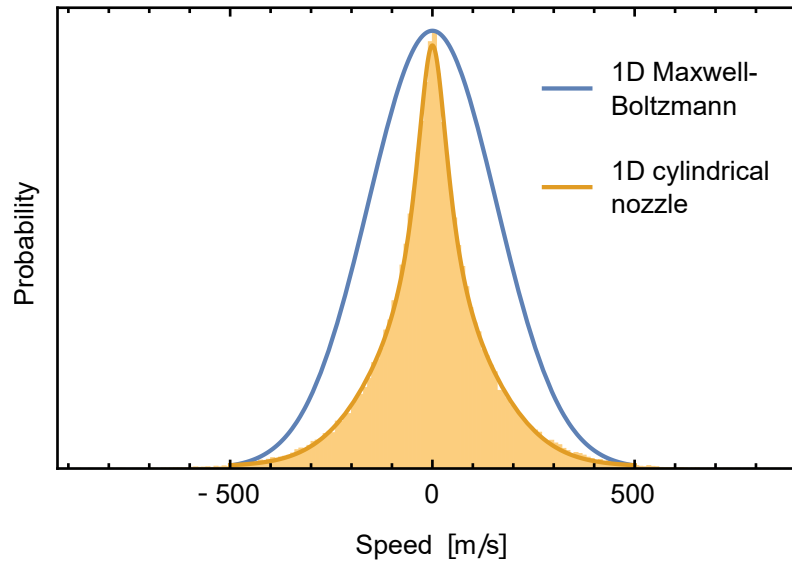


FIGURE 5.9: The simulated 1D speed distribution for Cs atoms emitted from the  $L/D = 3$  nozzle tube (orange) along the direction of the laser. The 1D Maxwell-Boltzmann distribution is shown for comparison (blue).

To communicate with the  $\sim 200$  MHz broad Doppler width, the laser waist should be focused to  $2w_o \approx 1 \mu\text{m}$ .

The 9.5 mm diameter laser access hole of the cold trap puts a limit on the spot size that can be achieved. The spot size is determined by the lens focal length  $f$ , the wavelength  $\lambda$ , and the input beam diameter  $D$ , and can be calculated by

$$2w_o = \frac{8\lambda f}{\pi D} \quad (5.8)$$

The lens used has a focal length of  $f = 250$  mm with a height of  $D = 6$  cm. For an 852 nm beam expanded to a height of 6 cm, the diffraction limited beam waist diameter is  $2w_0 = 10 \mu\text{m}$ . This corresponds to a transit-broadening of 20 MHz which is not large enough to communicate to the 200 MHz Doppler broadened distribution. The sheet laser setup still has the advantage of creating a volume of Cs\* below the laser where the lifetime of the Rydberg state can be studied by fluorescence imaging.

### 5.4.1.2 Fluorescence Imaging

To evaluate the laser focusing and positioning, the fluorescence is imaged on a CCD camera. A sample image of the fluorescence is shown in Figure 5.10(a) where the laser is positioned 3 mm below the exit of the nozzle. The thickness of the fluorescence is calibrated to known dimensions of the nozzle and a thickness of  $<100\ \mu\text{m}$ , limited by the CCD pixel resolution of the fluorescence. The transit-time broadening is only 20 MHz which is small compared to the Doppler-broadening. To improve upon this technique, a closer view of the fluorescence is needed to evaluate the laser thickness with higher resolution, and from this, the focusing lens position could be optimized further.

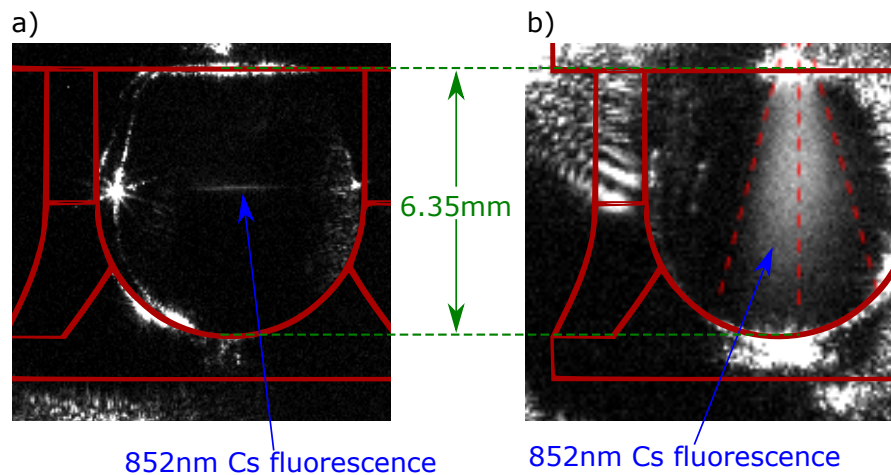


FIGURE 5.10: A CCD image of the 852 nm fluorescence with a) the laser focused to  $\sim 100\ \mu\text{m}$  b) the 4 mm diameter Gaussian laser beam. In these images, the Rydberg-excitation laser is blocked by the optical shutter at the optics table. An outline of the nozzle is shown. For the Gaussian beam, the angular distribution is shown by the dashed lines with the expected  $30^\circ$  angular full-width at half-maximum (FWHM).

The angular beam profile of the Cs beam emitted from the nozzle is observed by removing the cylindrical focusing lens and expanding the beam to a 4 mm diameter Gaussian waist. This is shown in Figure 5.10(b) with an outline of the  $30^\circ$  angular FWHM distribution.

### 5.4.1.3 Density of ground state Cs

The density of ground state Cs atoms can be determined from laser absorption spectroscopy. This method has been described for the characterization of a Cs oven by Barbisan *et al* [72]. The density of Cs atoms in a particular  $F$  hyperfine ground state  $n_k$  is given by

$$n_k = \frac{8\pi c}{A_{ik} l \lambda_o^4} \frac{g_k}{g_i} \int \ln \left( \frac{I(\lambda, 0)}{I(\lambda, l)} \right) d\lambda \quad (5.9)$$

where  $A_{ik} = 3.26 \times 10^7 \text{ s}^{-1}$  the spontaneous emission coefficient,  $l = 1.6 \text{ mm}$  is the absorption length through the vapour beam,  $g_k/g_i = 4/2$  is the statistical weight for the  $6P_{3/2}$  and ground state,  $I(\lambda, 0)$  is the wavelength-dependent intensity without laser absorption, and  $I(\lambda, l)$  is the intensity after absorption. This is valid at low laser intensities where the ground state depopulation is negligible, whereas high-laser intensities underestimate the density and require a correction term. The  $I(\lambda, l)$  term is the standard absorption spectrum, and the  $I(\lambda, 0)$  is the background level that is linearly dependent on wavelength for this laser. The laser frequency is scanned over the  $F = 4 \rightarrow F' = 3, 4, 5$  transition which accounts for 9/16 of the total ground state atoms. The frequency scan is controlled by tuning the laser current over time and the spectrum is fit to a multi-Lorentzian trend. The time axis is converted to wavelength by calibrating the time location of the  $F = 4 \rightarrow F' = 4$  and  $F = 4 \rightarrow F' = 5$  peaks to the known  $6.0826 \times 10^{-4} \text{ nm}$  separation (sample scan shown in Figure 5.11).

The study was performed with  $4 \mu\text{W}$  of laser power with an intensity of  $2 \text{ mW}/\text{cm}^2$ . At  $400 \text{ K}$ , the estimated ground state density based on the laser absorption is  $3 \times 10^{11} \text{ cm}^3$  (including both  $F$  ground states). The density is measured at different oven heater settings while monitoring the temperature with a sensor located on the front side of the oven. The nozzle temperature is maintained at temperature  $40 \text{ K}$  higher than the oven temperature. Figure 5.12 shows this scan for oven temperatures  $370 \text{ K}$  to  $400 \text{ K}$  where the hyperfine structure could be resolved for the wavelength calibration. The ground state density is linearly proportional to

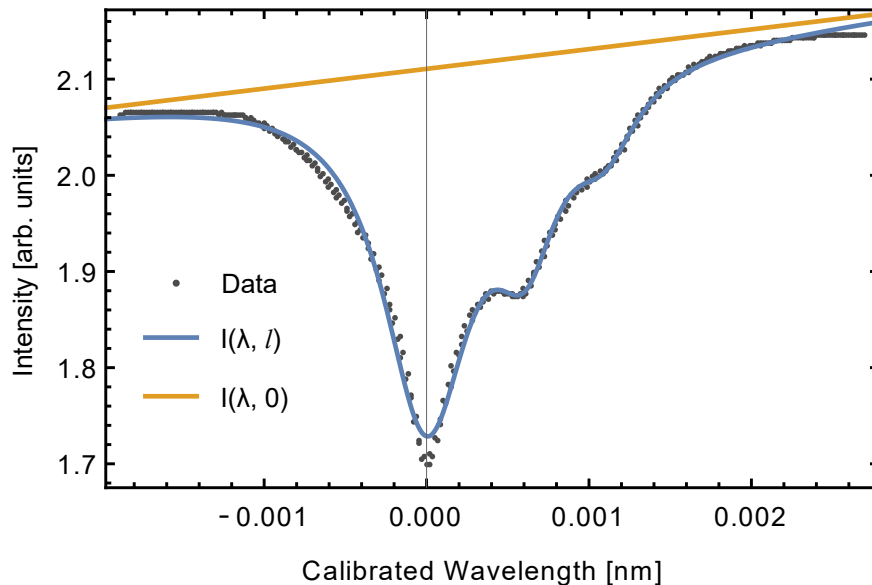


FIGURE 5.11: The 852 nm laser absorption scan calibrated to wavelength for calculating the density of ground state Cs. The  $I(\lambda, 0)$  background term is determined from a linear fit. The  $F = 4 \rightarrow F' = 5$  is referenced to  $\lambda = 0$  nm. The data is fit to the sum of three Gaussian distributions to determine  $I(\lambda, l)$ .

the vapour pressure. The estimated density at high temperatures is extrapolated based on the vapour pressure scaling as a function of temperature.

## 5.4.2 $6P_{3/2}$ to $nD_{5/2}$ Excitation

The excitation to the Rydberg state is studied by locking the 852 nm laser to the  $6S_{1/2}(F = 4) \rightarrow 6P_{3/2}(F = 5)$  transition and opening the optical shutter to combine the Rydberg-excitation laser beam with the 852 nm laser beam to co-propagate towards the thermal Cs beam.

### 5.4.2.1 EIT detection

The initial detection of the Rydberg transition was observed using the EIT technique used to lock the Rydberg-excitation laser. The transmission of the unabsorbed 852 nm photons through the Cs beam are separated from the 520 nm photons by a dichroic mirror and detected by a photodiode. An 852 nm line filter on the photodiode transmits a narrow wavelength range of  $852 \pm 10$  nm. With

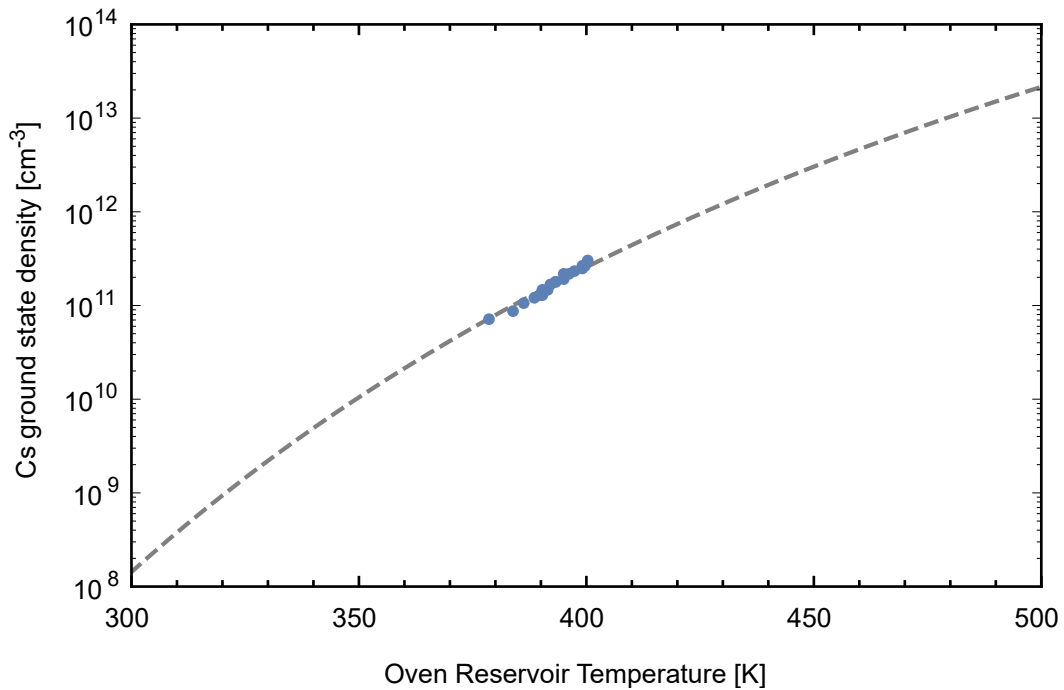


FIGURE 5.12: The measured Cs ground state density measured by laser absorption for various oven temperature. The density is extrapolated at high temperatures based on the vapour pressure scaling.

the Rydberg-excitation laser resonant with a transition, an increased transmission of the 852 nm laser occurs due to EIT. The Rydberg-excitation laser frequency is scanned and the EIT signal on the laser locking vapour cell is simultaneously monitored with the Cs beam EIT. A trace of this signal due to Rydberg excitation of the thermal Cs beam is shown in Figure 5.13. The 852 nm power is set to 200  $\mu$ W and the 520 nm power is set to 5.8 mW. The EIT signal is a useful indicator of the transition occurring but provides challenges to determine the Cs\* density due to the non-linear nature of this effect.

#### 5.4.2.2 Fluorescence measurements for Rydberg Density and Lifetime

A Rydberg fluorescence signal is collected onto an antireflective (AR) coated lens and focused onto a photodiode (Thorlabs DET36A2). The AR coated lens has a reflectance of less than 0.5% for wavelengths 650 nm to 1050 nm, and a reflectance of 11% at  $\sim$ 520 nm. A 2.54 cm diameter,  $f = 150$  mm lens is placed

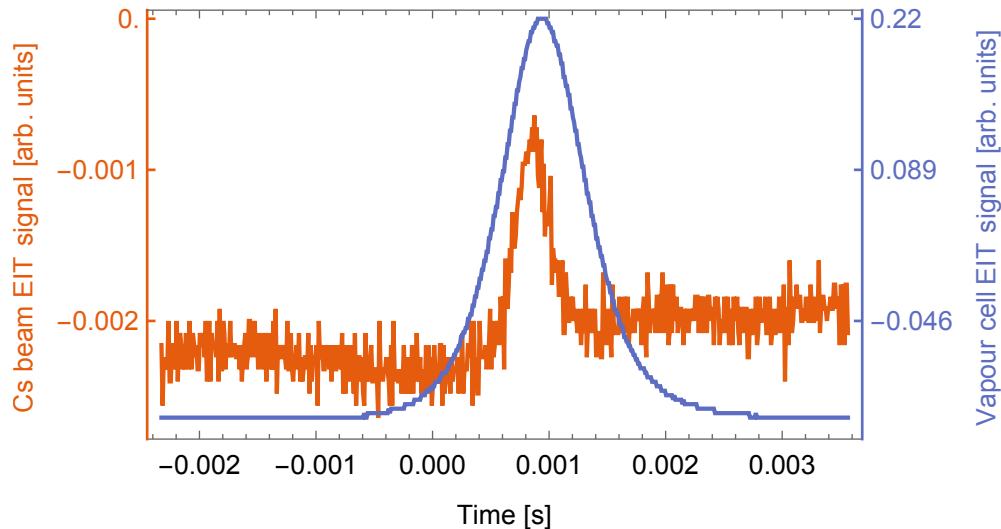


FIGURE 5.13: The EIT signal from the thermal Cs beam and from the vapour cell as the Rydberg-excitation laser frequency is scanned over time. The amplitude of the Cs beam EIT signal is dependent on the oven temperature and beam density.

30.0(5) cm away from the Cs beam fluorescence. This small solid angle of fluorescence (0.0056(2) sr, 0.045 % of  $4\pi$ ) is focused onto a photodiode that filters 852 nm photons and transmits the Rydberg fluorescence. The Rydberg-excitation laser frequency stabilization is momentarily unlocked and the 852 nm laser frequency is dithered across the resonance. The photodiode output is amplified (Femto DLCPA-200) and sent to a lock-in amplifier (SRS SR510) referenced at the dither frequency. The extracted lock-in output  $V_{lockin}$  is used to interpret the rate of Rydberg fluorescence photons emitted, following the equation

$$N_{Ryd} = \frac{4\pi C_{cal} V_{lockin}}{\varepsilon \Omega Gr} \quad (5.10)$$

A table of values for the parameters are listed in Table 5.1. A Cs atom excited to the Rydberg state leaves the sheet laser before decaying, such that each photon emitted represents a Rydberg Cs atom. With the oven temperature at 400 K, the fluorescence photon rate emitted is  $N_{Ryd} \approx 10^{13}$  Cs\*/s. The atoms travel with an average speed of 250 m/s and enter laser excitation area with a 0.8 mm radius, such that the density of Rydberg atoms is

Rydberg Fluorescence Rate Calculation Parameters		
Parameter	Value	Description
$C_{cal}$	$\frac{152(1) \text{ mW}}{32(1) \text{ mW}}$	Ratio of oscilloscope and lock-in output signal
$\Omega$	0.0056(2) sr	Solid angle collected
$G$	$10^8 \text{ V/A}$	Current amplifier gain
$r$	0.188 A/W	Photodiode responsivity at 520 nm
$\varepsilon$	(0.96)(0.89)(0.85)	Efficiency losses

TABLE 5.1: A list of parameters to calculate the rate of Rydberg fluorescence photons collected.  $C_{cal}$  is determined from a calibration of the 852 nm fluorescence measured on an oscilloscope and lock-in amplifier.  $\varepsilon$  is the efficiency losses due to laser window and lens reflection losses, and colour filter loss.

$$\rho^* = \frac{N_{Ryd}}{(250 \text{ m/s})\pi(0.8 \text{ mm})^2} \approx 10^{10} \text{ Cs}^*/\text{cm}^3 \quad (5.11)$$

This represents  $\sim 3\%$  laser excitation efficiency from the first excited state. For unit efficient charge-exchange the required Rydberg density is expected to be 10 times higher. This can be achieved by increasing the ground state density by a factor of 10 by heating the oven to  $\sim 430 \text{ K}$  and nozzle to  $\sim 470 \text{ K}$  for example. The  $\text{Ps}^*$  production experiments conducted to this point were with oven held at  $370 \text{ K}$  to  $400 \text{ K}$  for a cautious approach, with an estimated charge-exchange efficiency of  $1\%$ . Over the 1 year period that the oven has been operated, approximately  $0.6 \text{ g}$  of Cs has been used out of the  $25 \text{ g}$  of loaded.

The fluorescence from the Rydberg state is imaged onto a CCD camera as shown in Figure 5.14. The CCD is focused on the Rydberg fluorescence with an  $852 \text{ nm}$  filter to attenuate the  $6\text{P}_{3/2} \rightarrow 6\text{S}_{1/2}$  fluorescence. The optical image of the photodiode active area that is used for fluorescence measurements is also in focus, indicating the positioning of the collection lens and photodiode are optimally placed. The Rydberg fluorescence is captured within the  $13 \text{ mm}^2$  active area to ensure maximum collection. The image of the Rydberg fluorescence shows a large area of fluorescence as opposed to the thin sheet  $852 \text{ nm}$  fluorescence. The Rydberg state has an approximate lifetime of  $2 \mu\text{s}$  and travels downwards, which is shown by the exponential decay in intensity. Figure 5.15 is a measure of the pixel intensity along the vertical direction that intersects the fluorescence.

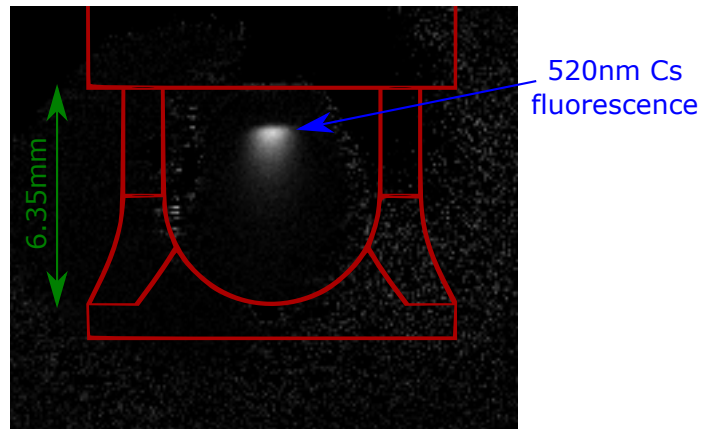


FIGURE 5.14: The fluorescence from Rydberg Cs decay captured on a CCD camera. The 852 nm and  $\sim 520$  nm laser beams are overlapped and focused to a thin beam ( $\sim 100 \mu\text{m}$  thin in the vertical direction). The CCD is filtered to attenuate the 852 nm fluorescence and transmit the  $\sim 520$  nm fluorescence. Because of the long lifetime of the Rydberg states and the 250 m/s speed of  $\text{Cs}^*$ , the  $\text{Cs}^*$  traverse a distance scale much larger than the laser thickness before decaying. An outline of the nozzle is shown.

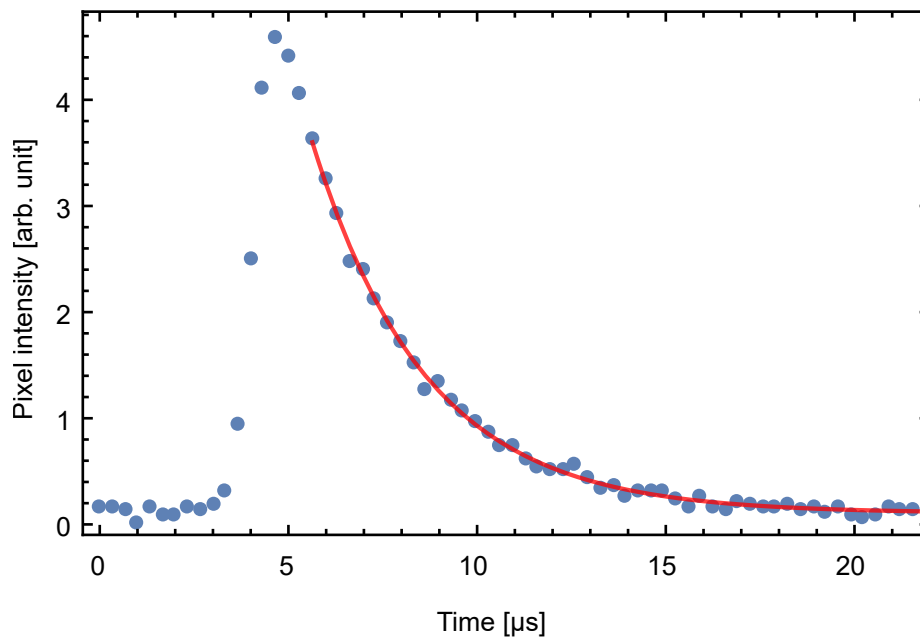


FIGURE 5.15: The intensity profile of the Rydberg fluorescence along the Cs beam direction. The pixel distance is converted to time based on nozzle reference dimensions and the average Cs speed.

The pixel length scale is calibrated to distance using known dimensions of the nozzle, and the distance scale is converted to time by the 250 m/s average speed of the atoms. From this profile, an exponential decay is fit to the data to extract the lifetime of the Rydberg atom. The lifetime of the Rydberg state is  $3.02(5) \mu\text{s}$  where the dominant uncertainty is from the pixel calibration. This indicates a Cs  $19D_{5/2}$

state ( $\tau = 3.05 \mu\text{s}$ ) driven with a 518.9 nm photon, resonant with Ps  $12^3\text{S}_1$ . The measured lifetime is consistent with the  $n^3$  lifetime scaling in a magnetic field-free region.

## 5.5 In-Vacuum Magnetic Field Coils

A magnetic field is required to guide the  $e^+$  towards the charge-exchange position. The  $e^+$  are guided past the output valve by a series of axial magnetic field coils that transfer the  $e^+$  through the cold tube and segmented Faraday cup. A pair of high-current, hand-wound coils from 6.35 mm diameter solid-core OFHC copper steers  $e^+$  through the cold Cs apertures. The coils are wound with 2 layers with 4 turns per layer and with a  $\sim 5$  mm gap between turns and layers. The first coil, “vacuum coil 1” with a 3.81 cm inner diameter, is  $\sim 2.9$  cm vertically off-axis to raise the  $e^+$  through the 7.9 mm diameter, 5 mm vertically-offset hole in the segmented Faraday cup. The second coil, “vacuum coil 2” with a 2.54 cm inner diameter, re-centers the  $e^+$  on-axis to pass through the 4 mm diameter hole in the cold trap towards the Cs nozzle.

The coils are mounted and electrically connected to 6.35 mm diameter copper power feedthroughs (Lesker EFT0523253). The heat generated from Joule heating is conducted out of vacuum through the feedthroughs, air-cooled to 40 °C. To minimize the power generated during an experiment cycle, the coils are powered 5 s prior to the ramp out and are turned off after the 3 s ramp, a 44 % duty cycle. These feedthroughs and coils are mounted on adjustable bellows to adjust the position and orientation of each coil. The physical realization of the coils and the oven is shown in Figure 5.16.

The measured on-axis magnetic field for each coil is shown in Figure 5.17 measured with a Gaussmeter (Lakeshore 460). The typical operating currents for vacuum coils 1 and 2 are 120 A and 18 A. The desired current for vacuum coil 2 is much higher to provide a stronger magnetic field at the charge-exchange. The stronger magnetic field would further increase the  $e^+$  beam diameter compression.

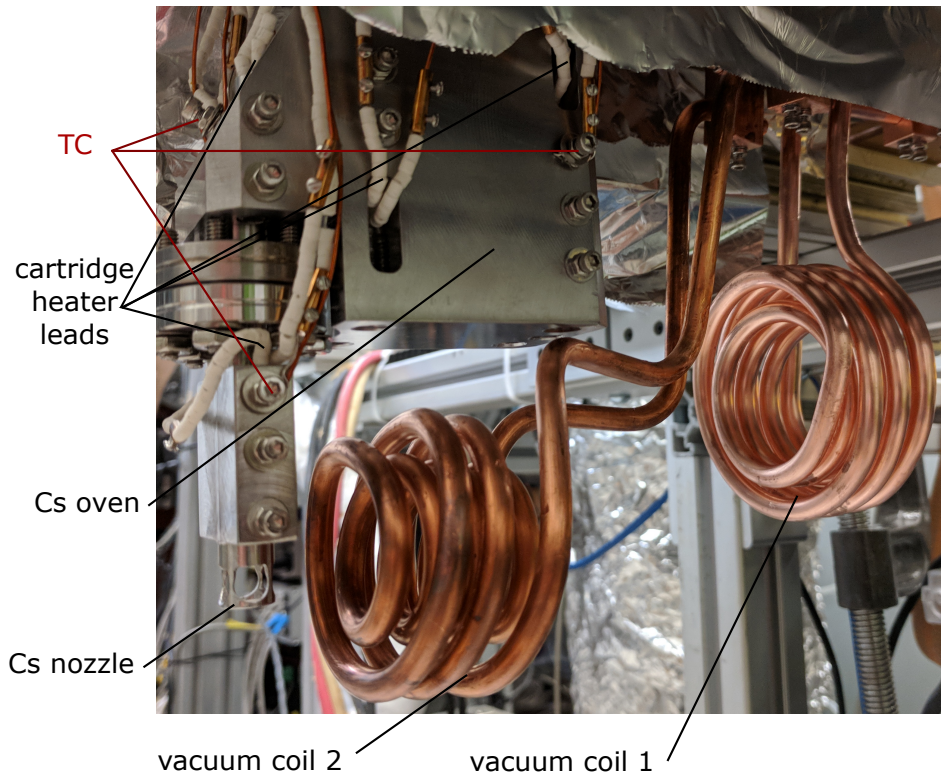


FIGURE 5.16: The in-vacuum magnetic field coils and the Cs oven. The locations of the cartridge heater pairs and thermocouples (TC) are also denoted.

Technical challenges to produce connecting field lines at higher currents, and by adjusting the relative position and angles of the two vacuum coils have limited further improvement. The  $e^+$  are inefficiently compressed through the 4 mm diameter input hole of the cold trap with 15% of the  $e^+$  beam clipped on the hole. An external coil located after the charge-exchange boosts the magnetic field at the charge-exchange region to 60 G. Approximately 30% of the  $e^+$  beam is within a 1 mm diameter, corresponding to  $\sim 400\,000$   $e^+$  for charge-exchange per 13 s trial. The current settings for each coil are optimized by guiding the moderated and ramped beams through the nozzle and into the detection region, where the  $e^+$  annihilation is monitored.

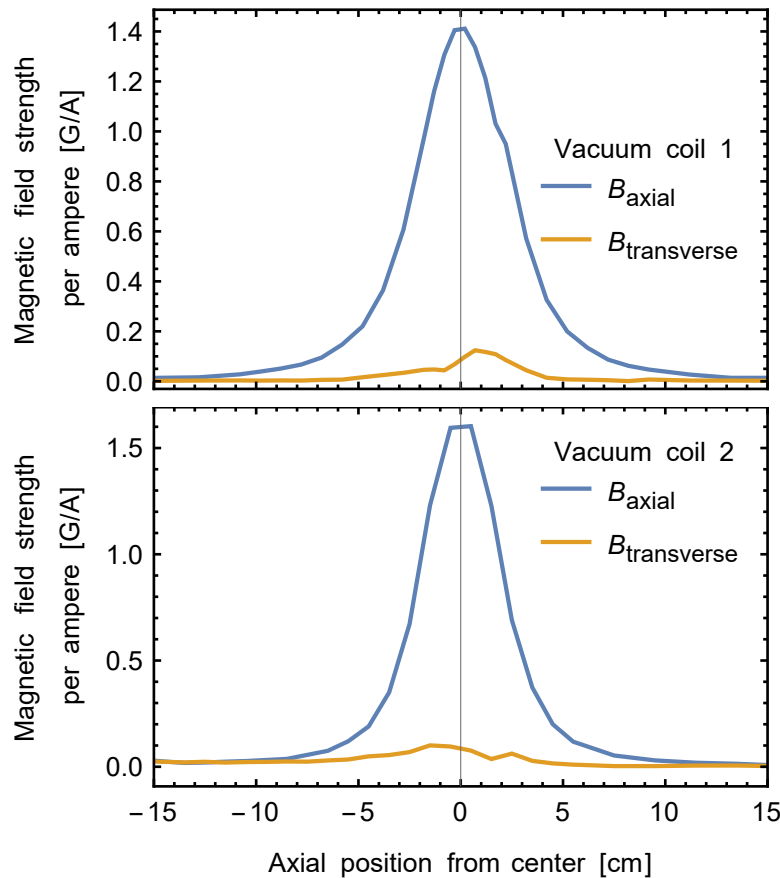


FIGURE 5.17: The axial and transverse magnetic field generated for each vacuum magnetic field coil. The magnetic fields are measured along the axis relative to the center, with 1 A flowing through the coils.

## 5.6 Detection Region and Quadrupole Guide

The detection region is used to detect the coincident back-to-back  $e^+$  annihilation from  $e^+$ , Ps, and Ps\* atoms that make it into the region. An electrostatic quadrupole guide for neutral Ps\* atoms guides the atoms over a 48 cm path, towards the detection region. It has the capability to guide atoms entering from a large solid angle (up to a  $13^\circ$  half-angle cone) with a compact system. It also allows for Ps\* state filtering where state-selective experiments can be performed. An overview of the system is shown in Figure 5.18. A 1.2 cm diameter aperture located 2.1 cm after the nozzle separates the entrance of the quadrupole guide from the charge-exchange. This aperture is electrically isolated such that a bias can be applied to reflect the charged  $e^+$  and transmit only the neutral Ps\*. When the bias is set to a potential below the  $e^+$  energy, the  $e^+$  are transmitted through. A

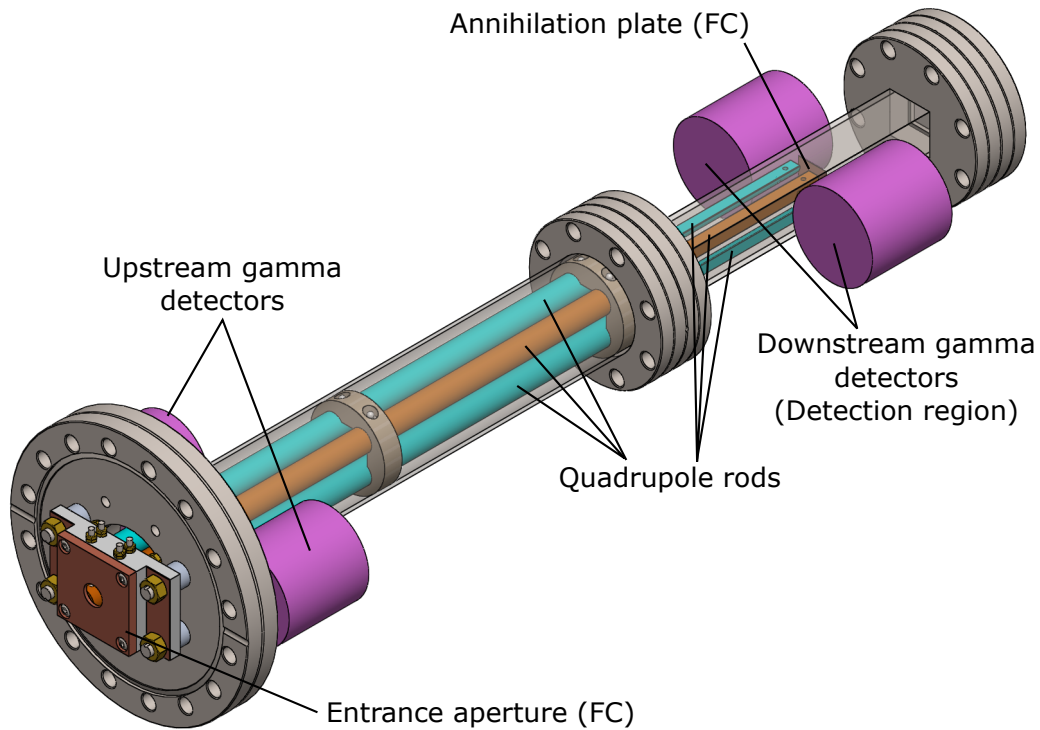


FIGURE 5.18: An overview of the quadrupole guide and the detection region. The entrance aperture and annihilation plate are electrically isolated for  $e^+$  blocking. These can also be used for Faraday cup (FC) detection of pulsed plasmas of  $e^+$ . Parts of the vacuum chamber are shown as transparent to view the quadrupole rods. The oppositely coloured rods represent the opposite voltage polarity applied to the rods. The 5 cm-thick lead shielding before the downstream gamma detectors are hidden in figure.

series of external magnetic field coils produce an axial magnetic field to guide the  $e^+$  to optimize the  $e^+$  steering.

The detection region is a  $2.54\text{ cm} \times 2.54\text{ cm}$  square cross-section vacuum region that is 20 cm long. A copper plate located at the midpoint of the region annihilates a  $e^+$  or  $\text{Ps}^*$  atom that strikes the surface. A pair of gamma detectors (NaI(Tl)-SiPM) is located outside of the square vacuum region at the annihilation plate. This “downstream” two-detector geometry has a large solid-angle of detection, with 60% of the solid angle collected.

The electrostatic quadrupole guide is designed to capture a large solid angle of the  $\text{Ps}^*$  and provide radial confinement. The internal energy structure of an atom within an electric field is perturbed by the Stark effect, where the  $l$ -states within an  $n$ -manifold shift differently with the electric field. The spread of these states as a

function of the electric field strength is known as the Stark fan. The energy states that shift higher in potential energy are termed as “low-field seeking state” and the states that shift lower in potential energy are termed as “high-field seeking states”. An atom in a low-field seeking state can be radially confined in an electrostatic quadrupole field and the high-field seeking states are forced radially out. The structure of  $\text{Ps}^*$  has an S-state at the highest potential energy within an  $n$ -manifold and this state experiences the largest force as a low-field seeking state. In ordinary atoms, the S-state is the lowest energy state in an  $n$ -manifold and is a high-field seeking state. Figure 5.19 shows that the  $\text{Ps } n^3\text{S}_1$  states are low-field seeking and that the  $\text{Ps } n^3\text{P}_j$  states are high-field seeking such that the  $\text{Ps}$  guided are not in P-states. A possible RF transition that drives the  $\text{Ps } n^3\text{S}_1$  atoms to the P-state before entering the guide would be observed as a loss of S-state atoms. As an example for the  $n = 11$  states, the  $11^3\text{P}_j$  state atoms have a  $0.5 \mu\text{s}$  lifetime compared to the  $5 \mu\text{s}$  lifetime of the  $11^3\text{S}_1$ . Over time, the P-states become less populated relative to the S-state, and a RF transition that transfers the S-state atoms to the P-state would put the atoms in a state that cannot be guided and detected.

The force  $\mathbf{F}$  on a particle of mass  $m$  is defined as

$$\mathbf{F} = -\nabla U = m\mathbf{a} \quad (5.12)$$

where  $U$  is a position-dependent potential energy,  $\nabla$  is the spatial gradient operator, and  $\mathbf{a}$  is the acceleration. From this, one can see that an electric potential geometry that generates an inhomogeneous electric field produces a spatially-varying Stark shift, represented by  $U(|\mathbf{E}(\mathbf{x})|)$ . An electric quadrupole geometry consists of four cylindrical poles positioned in the corners of a square, where the adjacent poles alternate between positive and negative voltage polarity. The strength of the electric field is the strongest between adjacent poles and becomes weaker towards the center. A  $\text{Ps}^*$  atom moving radially away from the center experiences a progressively stronger electric field that has a quadratic growth. In a low-field seeking state, the force vector points inwards for radial confinement.

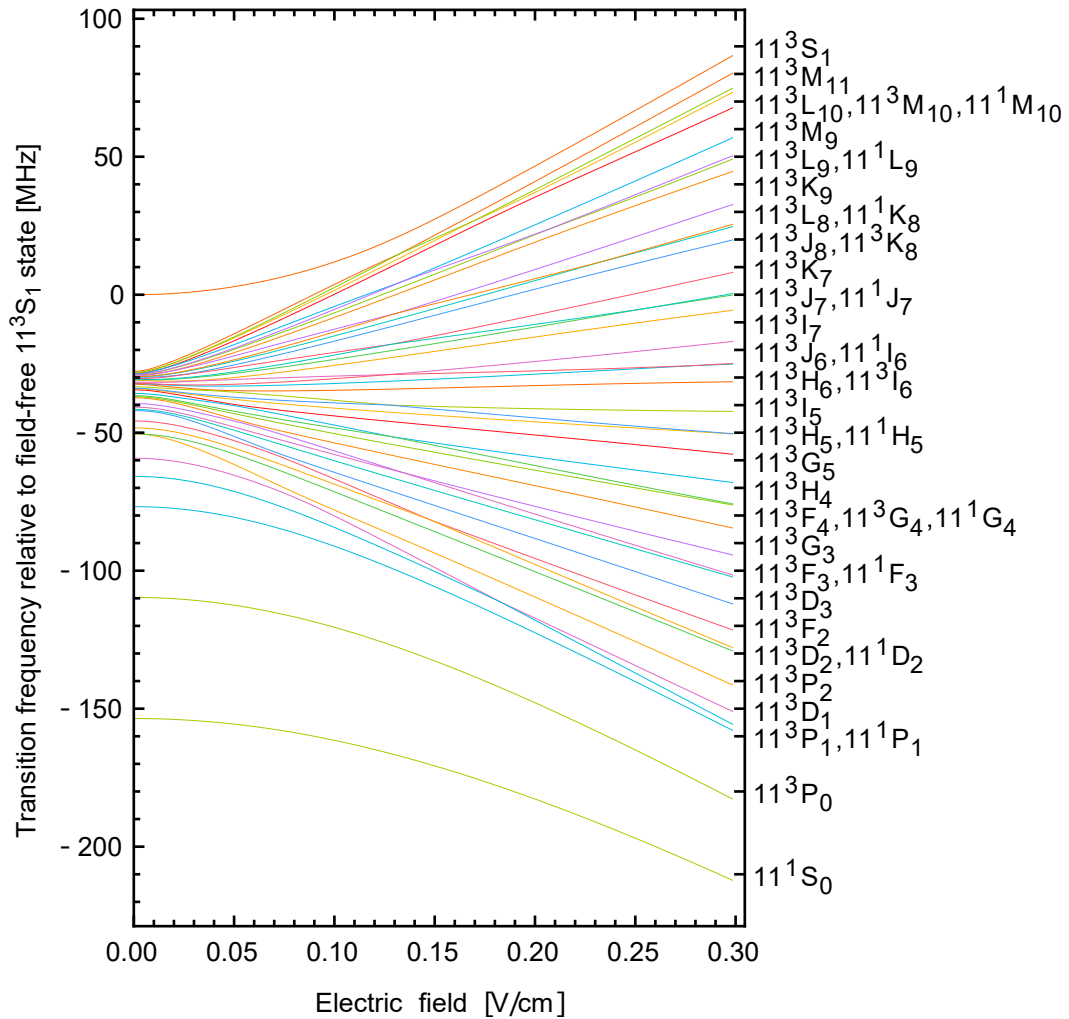


FIGURE 5.19: The low-field Stark fan. The left-hand axis represents the transition frequency between each state, where the zero is relative to the field-free Ps  $11^3S_1$  state. The right-hand axis denotes the Stark-shifted states. At low electric field strengths, the states initially shift in a quadratic form.

This system is realized with 1.27 cm diameter copper rods that are 1.80 cm apart from adjacent rods, and distanced 1.27 cm from the center. The total length of each rod is 45.72 cm, where the last 7.62 cm is modified to fit within the 2.54 cm  $\times$  2.54 cm square detection region vacuum component. For each rod, material is removed such that the quadrant closest to the guide axis remains. The system is shown in Figure 5.18 where the colour represents opposite voltage polarities. PEEK insulators electrically isolate and position the rods within the system.

The electric potential generated by the rods and the grounded chamber is modeled using a successive over-relation (SOR) method to numerically solve the Laplace

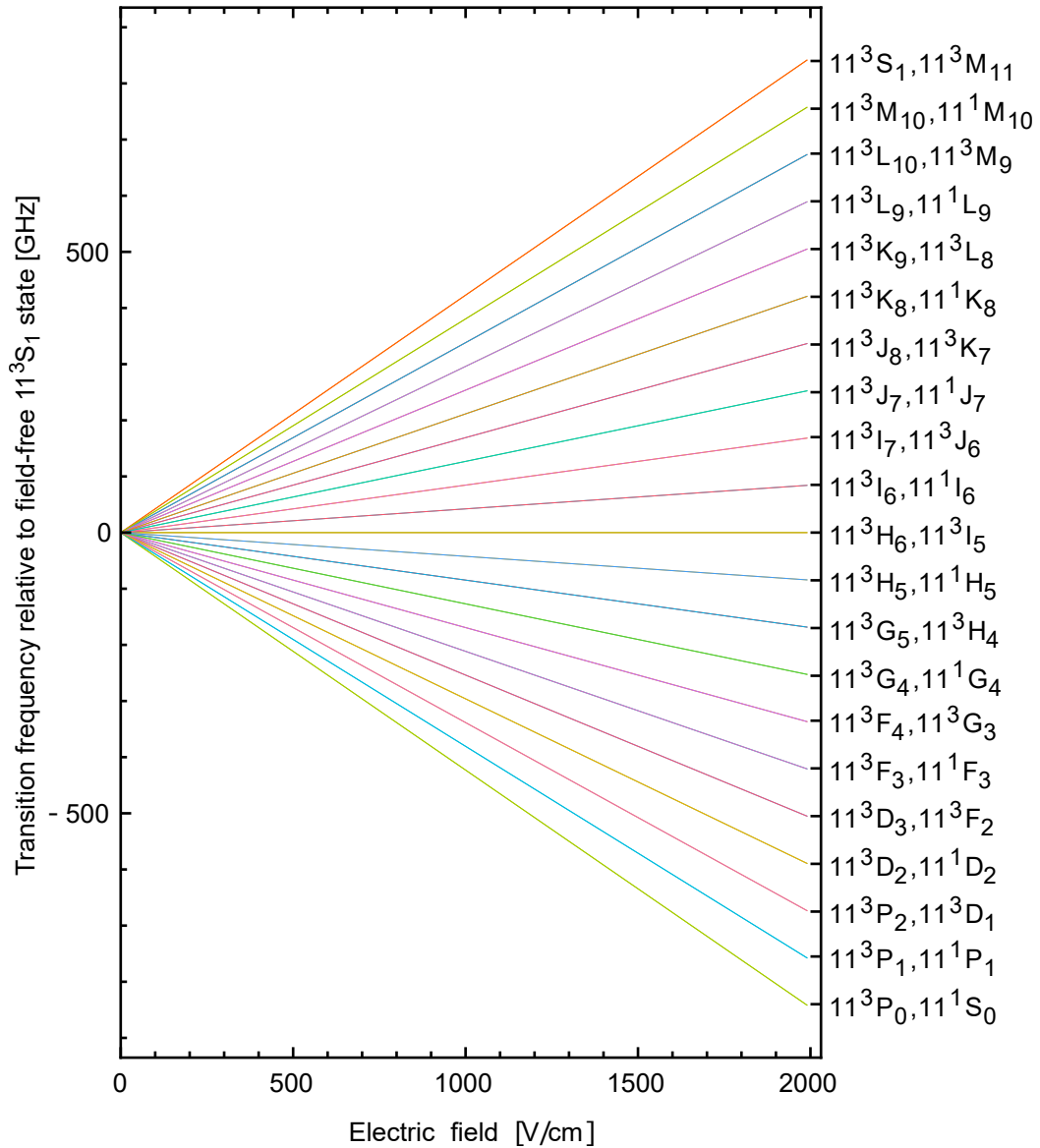


FIGURE 5.20: The high-field Stark fan. The left-hand axis represents the transition frequency between each state, where the zero is relative to the field-free Ps  $11^3S_1$  state. The right-hand axis denotes the Stark-shifted states. At high electric field strengths, the states shift linearly.

equation. For a particular  $n$ -manifold Stark fan, the Stark shift is approximately linear where the slope can be obtained for each  $n^3l_j$  state. The  $11^3S_1$  state has a Stark shift of  $2.8 \times 10^{-27}$  J/(V/m). The goal is to capture Ps  $11^3S_1$  with  $<100$  meV of kinetic energy. The aperture clips Ps\* from entering the quadrupole guide if it has a  $\theta > 13^\circ$  half-angle trajectory. A Monte-Carlo simulation that follows the trajectories of Ps\* atoms emitted within a  $0^\circ < \theta < 13^\circ$  half-angle cone is used to evaluate the guiding efficiency as a function of the applied quadrupole voltage and

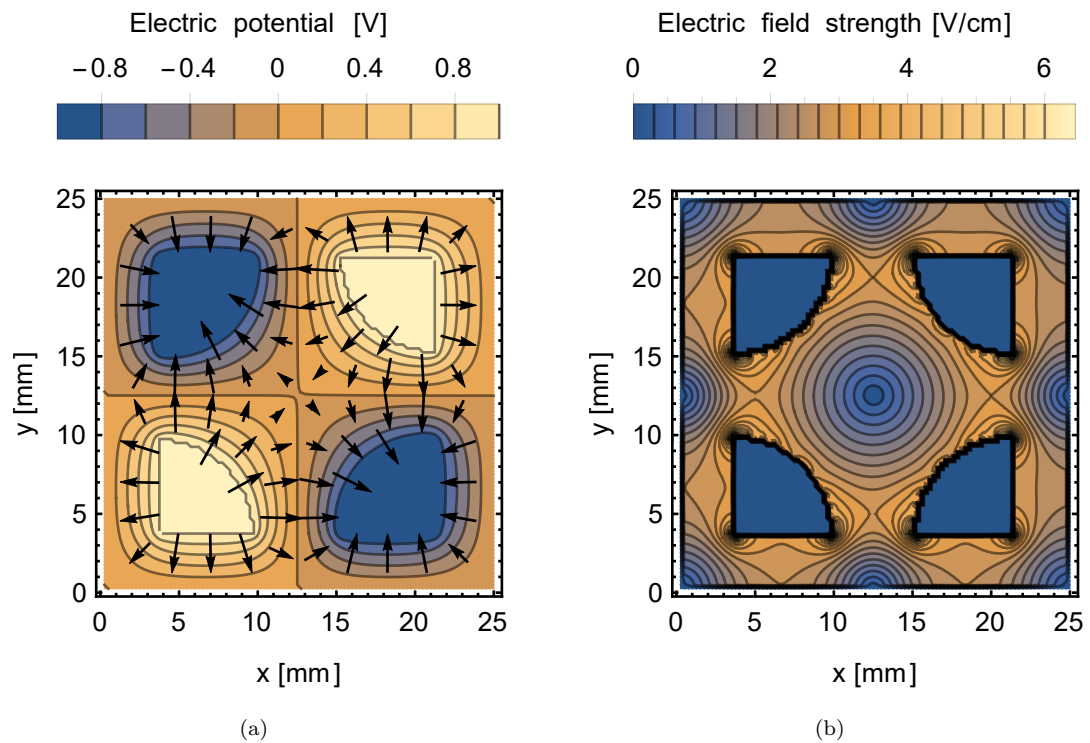


FIGURE 5.21: The electric potential generated from quadrupole rod voltages set to  $\pm 1$  V and the grounded vacuum chamber walls (along the borders). The electric potentials shown in (a) are computed from a relaxation method to solve the Laplace equation. The electric field is computed from the gradient of the electric potential, and the strength of the field is shown in (b).

Ps\* kinetic energy. The trajectory is computed with a fourth-order Runge-Kutta technique that is widely used for numerically solving differential equations and has a small accumulated error compared to lower-order techniques.

The Ps\* atom initially moves between 3-dimensional grid points used for the SOR, and the local electric field strength is computed by a trilinear interpolation to obtain the potential gradient. After traversing 8.5 mm into the guide, the axial potential gradient varies by less than 1% such that its effect is negligible. The electric potential is then computed in a 2-dimensional grid where only radial effects are considered. The electric potential and electric field strength within the quadrupole are shown in Figure 5.21 with the rods biased to  $\pm 1$  V. The strength of the electric field is also shown, where the contours are nearly harmonic near the center (shown by concentric circles).

The guide efficiency for Ps  $11^3S_1$  atoms as a function of kinetic energy for various

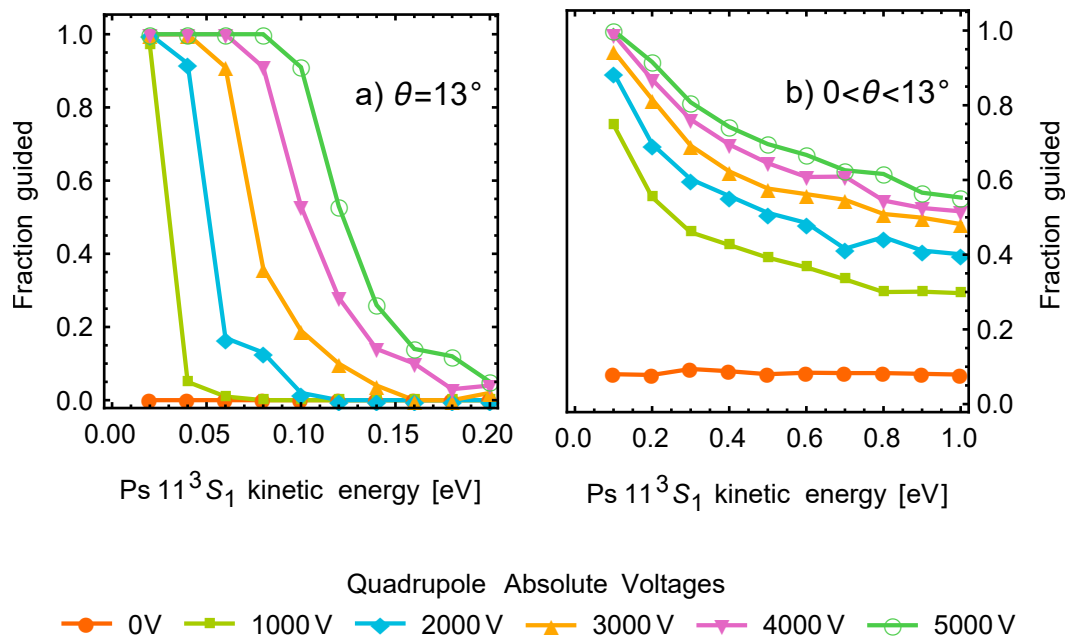


FIGURE 5.22: The modeled fraction of Ps  $11^3S_1$  atoms emitted at (a)  $\theta = 13^\circ$  (b)  $0^\circ < \theta < 13^\circ$  half-angle that are guided as a function of kinetic energy at various quadrupole rod voltages. A total of 1000 particles are flown for each data point.

absolute quadrupole voltages is shown in Figure 5.22. The system was designed to operate up to  $\pm 5000$  V. As it can be seen, at higher absolute quadrupole rod voltages, a larger range of energies can be guided. At  $\pm 5000$  V, Ps  $11^3S_1$  with  $< 100$  meV that are emitted at the extreme  $\theta = 13^\circ$  half-angle can be efficiently guided. For Ps atoms emitted uniformly between  $0^\circ < \theta < 13^\circ$ , a modest  $\pm 1000$  V quadrupole voltage can guide  $> 70\%$  of atoms with 100 meV of kinetic energy. A sample of trajectories is shown in Figure 5.24 for  $\theta = 13^\circ$ . The electric field that a Ps  $11^3S_1$  experiences along the trajectory is sufficiently low compared to the field required for ionization, 20 kV/cm. The guide efficiency for all  $l$ -states for singlet and triplet Ps is shown in Figure 5.25. A broad range of high-field seeking  $l$ -states are removed from the guide by becoming attracted towards the rods and annihilating within a short distance of entering.

The models shown thus far neglect the lifetime of the Ps atoms. In order for the Ps to be detected, it must survive a long enough time to travel towards the detection region. The electric fields within the quadrupole guide mix the  $l$ -character of

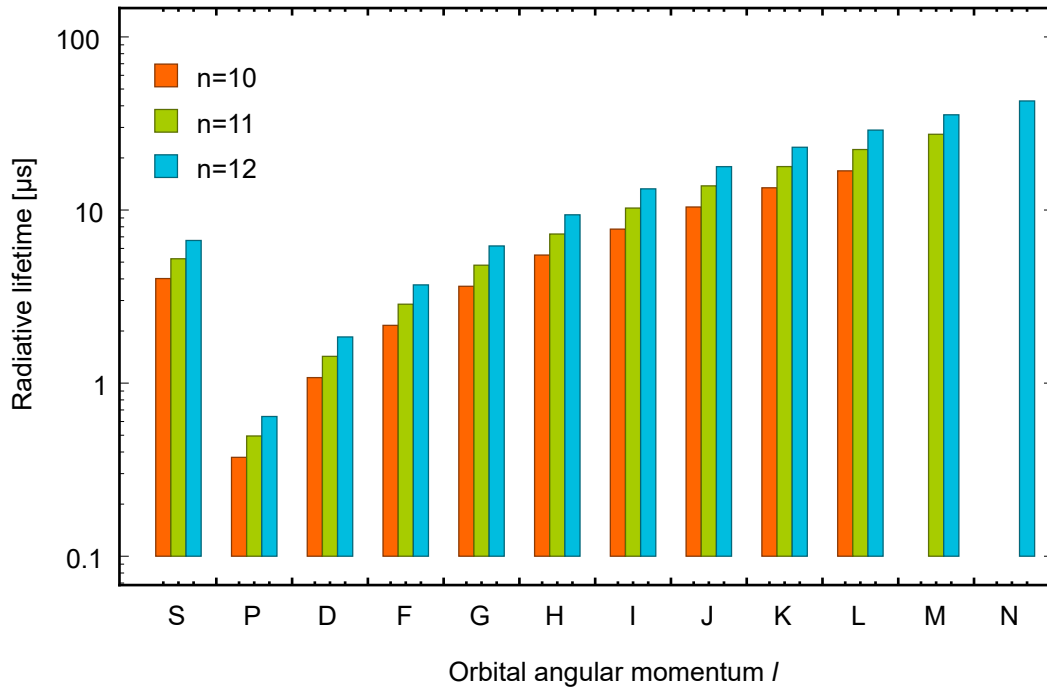


FIGURE 5.23: The field-free radiative lifetime of the  $n = 10 - 12$  triplet Ps states. The S-states have a larger lifetime than the P-states which is useful for spectroscopy measurements where transitions are driven between these states.

the states within the Stark fan. The S-states of interest are expected to have a reduced radiative lifetime due to a mixture of short-lived  $P$ -character. The field-free lifetime of the  $n = 10 - 12$  triplet states are shown in Figure 5.23. For an  $n = 11$  triplet S-state, the atom must have at least 50 meV of kinetic energy to be detected based on a lifetime of 5.2  $\mu\text{s}$  and a travel distance of 48 cm. A secondary pair of “upstream” detectors located at the start of the quadrupole is mainly used for diagnostic purposes to check for any Ps annihilating near the entrance. This could be from Ps that annihilate due to poor capture by the guide, or from shorter-lived states of Ps for example. Experiments can be conducted to transfer signal from the upstream to downstream detectors as an indication of Ps\* traversing guide. The upstream detectors are separated by the vacuum tube diameter of 5.08 cm, subtending a solid angle of  $\frac{4\pi}{3}$  (33% coverage).

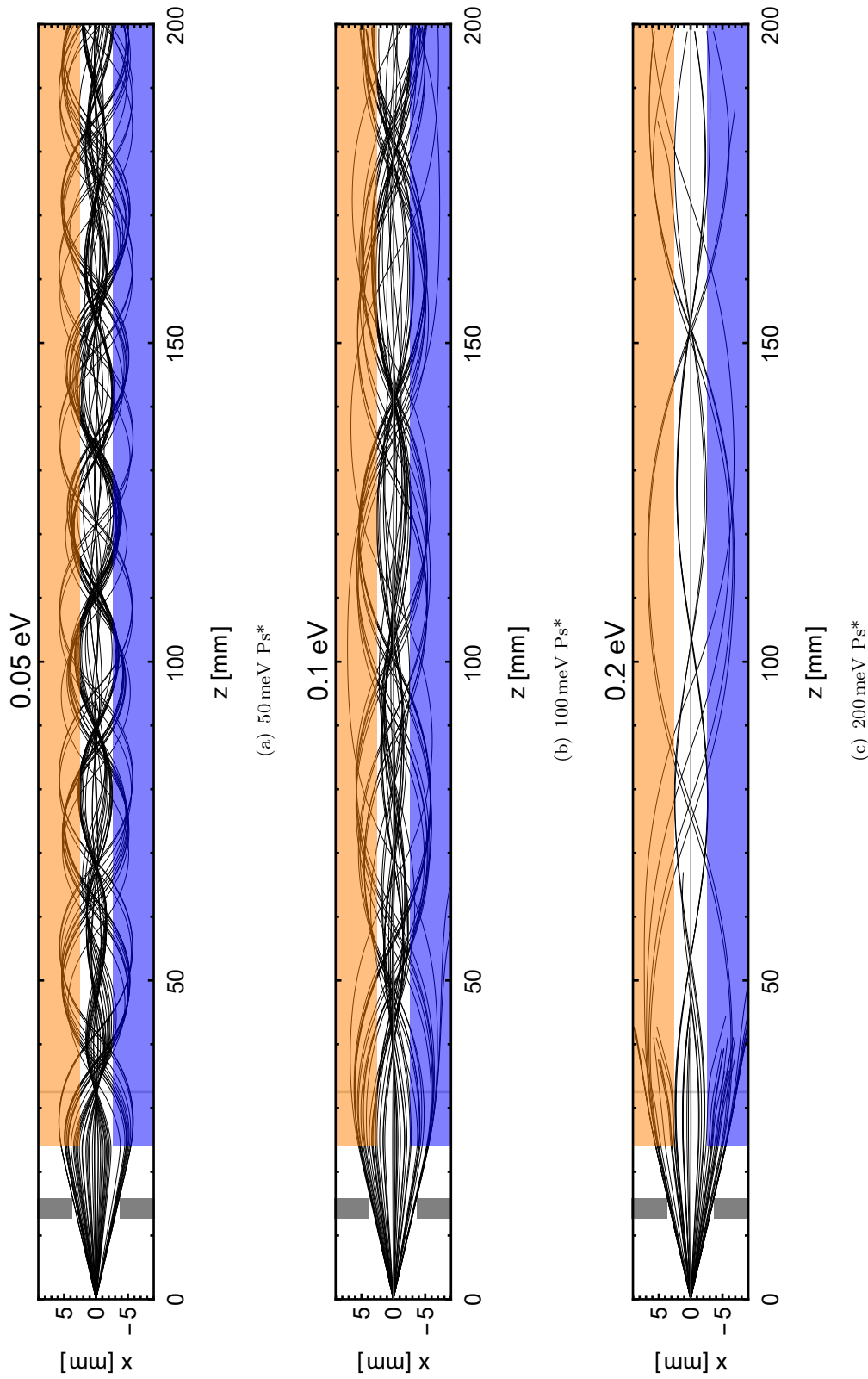


FIGURE 5.24: The modeled trajectories of 50  $\text{Ps } 1^3\text{S}_1$  atoms at  $\theta = 13^\circ$  with (a) 50 meV, (b) 100 meV and (c) 200 meV with the quadrupole bias fixed to  $\pm 5000$  V. The opposite quadrupole polarity is shown in orange and blue. The grey band represent the grounded entrance aperture to the guide. The thin grid line represents the transition from a 3-dimensional force to 2-dimensional force computation.

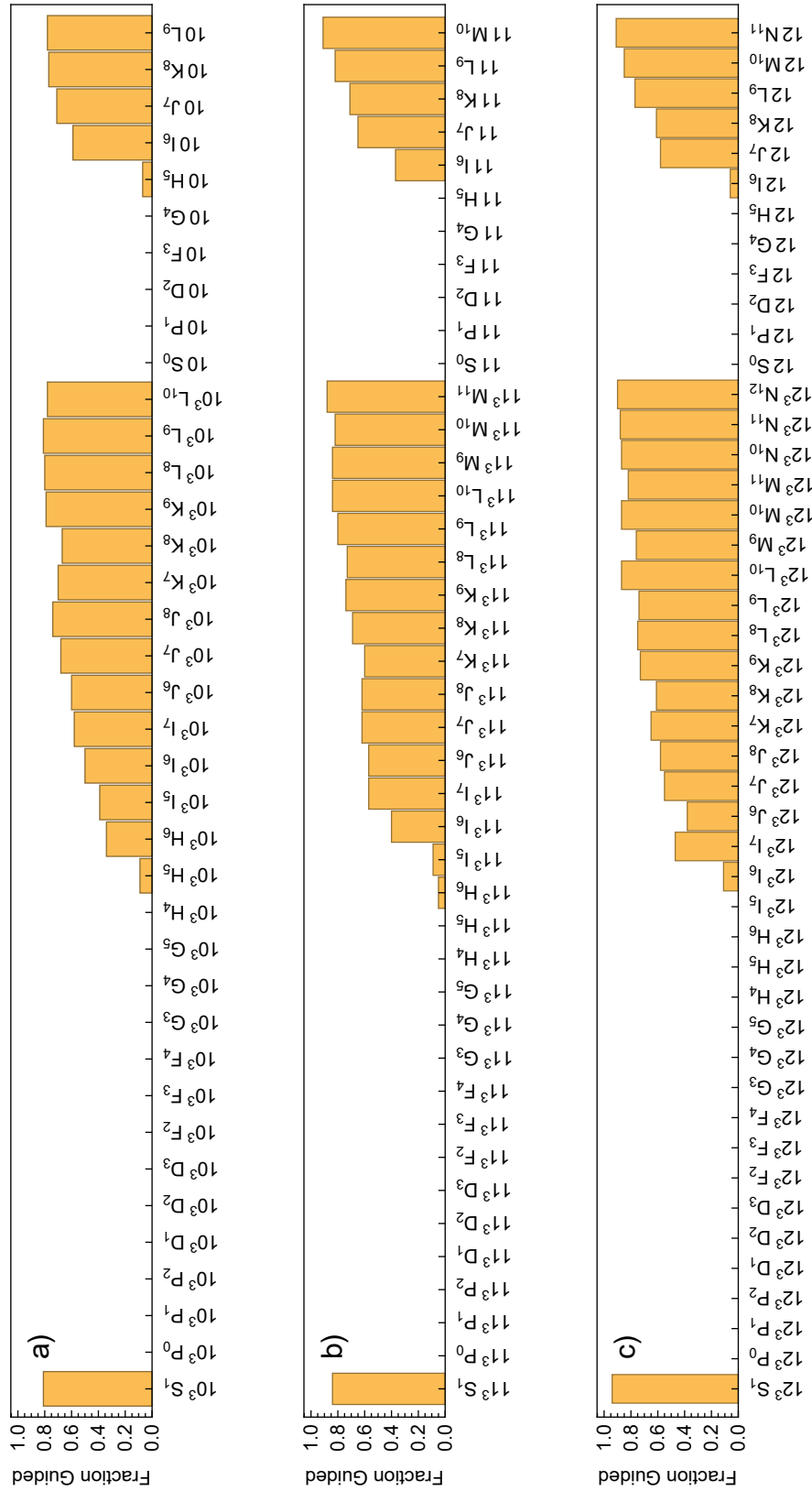


FIGURE 5.25: The modeled fraction of Ps atoms guided in the (a)  $n = 10$ , (b)  $n = 11$ , (c)  $n = 12$  manifold where the Ps has 100 meV of kinetic energy and the quadrupole rods are held at  $\pm 2000$  V. A large range of  $l$ -states are high-field seeking and are not guided. For higher- $n$ , the larger Stark shifts lead to a larger fraction of Ps that can be guided.

## 5.7 State-Selective Field-Ionization Detector

An alternative detector system is the state-selective field-ionization (SS-FI) detector. This was designed prior to the quadrupole guide, but the quadrupole guide was installed first for its compactness and simplicity to detect an initial Ps\* signal. This system can be installed in place of the quadrupole guide, or it can be adapted for installation after the quadrupole guide. In the present system, this system is not installed on the Ps apparatus.

The SS-FI detector is a system that is designed to distinguish and detect certain states of Ps\*. Depending on the Ps\* state, the Ps\* atom will ionize if it is within a sufficiently strong electric field. Classically, the electric field strength,  $F_{classical}$ , required to ionize an atom in state  $n$  follows the form

$$F_{classical} \propto \frac{F_0}{16n^4} \quad (5.13)$$

which demonstrates that atoms in higher Rydberg states become ionized in weaker electric fields. Within the Stark fan of a particular  $n$  state, the state with the largest positive shift is termed as the “blue state” and the state with the most negative shift is termed as the “red state”. For the RF spectroscopy program, the Ps  $11^3S_1$  state is the blue state, and the Ps  $11^3P_j$  states are the red states. For the red state, the field ionization strength scales as

$$F_{red} \propto \frac{F_0}{9n^4} \quad (5.14)$$

and the blue state scales as

$$F_{blue} \propto \frac{2F_0}{9n^4} \quad (5.15)$$

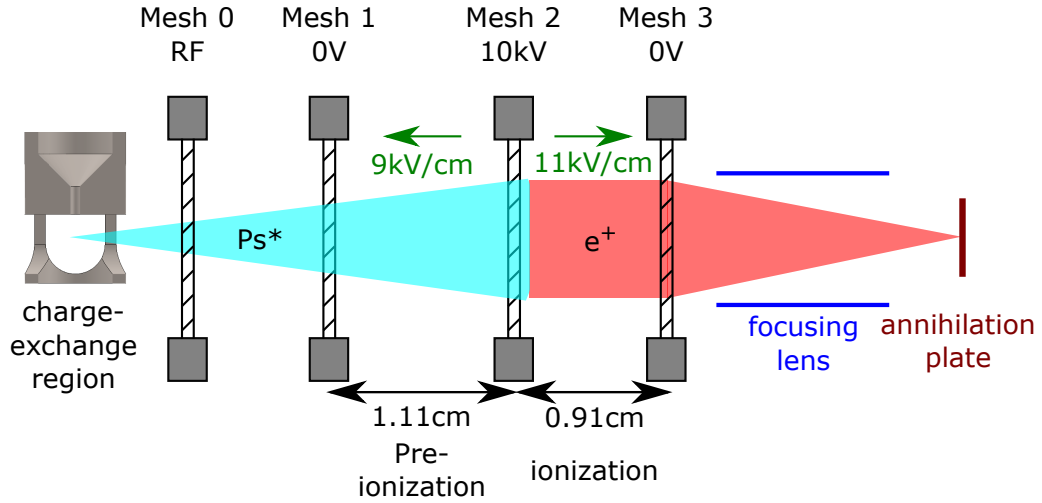


FIGURE 5.26: A depiction of the state-selective field-ionization detector system. Two electric field regions are generated by three wire meshes. A large solid-angle of  $\text{Ps}^*$  produced from charge-exchange enter the system. In this example, a  $\text{Ps}^*$  atom that ionizes at  $11 \text{ kV/cm}$  ionizes in the second electric field region, and the  $e^+$  transmits through the wire meshes and is focused onto an annihilation plate for detection. A radiofrequency applied to mesh-0 can induce transitions in  $\text{Ps}^*$  before it enters the electric field regions.

For the  $11^3\text{S}_1$  and  $11^3\text{P}_j$  states, the atom ionizes in an electric field strength of  $19.5 \text{ kV/cm}$  and  $9.8 \text{ kV/cm}$  respectively. The key to the design of the SS-FI detector is generating two electric field regions where both states can be ionized.

The electric fields are generated by a system of three wire meshes that are separated by  $1.11 \text{ cm}$  and  $0.91 \text{ cm}$ . The first and last wire mesh are grounded, and the second mesh is held at  $10 \text{ kV}$  for example. This generates a  $9 \text{ kV/cm}$  electric field between mesh-1 and mesh-2, and an  $11 \text{ kV/cm}$  electric field between mesh-2 and mesh-3. The region between mesh-1 and mesh-2 is termed as the “pre-ionization region” and the region between mesh-2 and mesh-3 is termed as the “ionization region”. A schematic of this system is shown in Figure 5.26. An additional mesh prior to these is used to induce an RF transition in  $\text{Ps}^*$  before entering the electric field regions.

In this example, for a  $\text{Ps}^*$  atom that ionizes in an  $11 \text{ kV/cm}$  electric field, the  $\text{Ps}^*$  transmits through the pre-ionization region since  $9 \text{ kV/cm}$  is not sufficient to ionize. In the ionization region, the  $11 \text{ kV/cm}$  electric field ionizes the atom into its  $e^-$  and  $e^+$  constituents. The  $e^+$  is accelerated in the direction of the field towards

a focusing lens to annihilate the  $e^+$  onto an annihilation plate for detection. The pre-ionization will ionize higher- $n$  state  $\text{Ps}^*$ , where the  $e^+$  is accelerated in the direction back towards the charge-exchange.

For the detection of  $11^3\text{S}_1$ , setting mesh-2 to 18 kV generates the necessary field to ionize and detect the state. The pre-ionization region filters out the  $11^3\text{P}_j$  states and  $n > 11$  atoms. Mesh-1 is placed 30 cm away from the charge-exchange such that there is a population difference between the  $11^3\text{S}_1$  ( $\tau = 5.2 \mu\text{s}$ ) and  $11^3\text{P}_j$  states ( $\tau = 0.5 \mu\text{s}$ ). For 100 meV  $\text{Ps}^*$ , the  $11^3\text{P}_j$  states are reduced to 1% of its initial population and the  $11^3\text{S}_1$  state is reduced to 65% of the initial population by the time the atoms reach mesh-1. The RF applied to mesh-0 can transfer population from  $11^3\text{S}_1$  to  $11^3\text{P}_j$ , resulting in a decreased detection of  $11^3\text{S}_1$  atoms.

The system was modelled in SIMION where the electric potentials were computed and Monte Carlo simulations were performed to study the  $\text{Ps}^*$  and  $e^+$  trajectory. Figure 5.27 is a cross-section view of the modelled wire mesh system.

The coloured lines around the wires are equipotential contours that represent constant electric field strength. The simulation sends  $\text{Ps}^*$  in an isotropic distribution towards the system and is programmed to ionize into a  $e^+$  at a set threshold. In 5.27 b), a  $\text{Ps}^*$  atom that hypothetically ionizes in a 10.75 kV/cm electric field is sent towards the SS-FI system. The atoms ionize in the pre-ionization region and the  $e^+$  is reflected back towards the charge-exchange and is undetected. If the  $\text{Ps}^*$  ionizes at 11 kV/cm as in 5.27 c), it is above threshold to ionize in the ionization region, where the  $e^+$  is accelerated and focused towards an annihilation plate for detection.

In the model, mesh-2 and mesh-3 are 0.25 mm diameter wires that are spaced 3 mm apart. Mesh-1 consists of 1 mm diameter wires that are positioned such that the  $\text{Ps}^*$  are blocked from a direct path to the wires in mesh-2. The purpose of these blocking wires is to minimize the highly non-uniform fields that  $\text{Ps}^*$  would experience close to the wires. Figure 5.28 demonstrates the sharp threshold to detect  $\text{Ps}^*$  atoms that ionize above a certain threshold. The model sends  $\text{Ps}^*$  that ionize in fields between 10 kV/cm to 11.2 kV/cm towards the SS-FI and counts

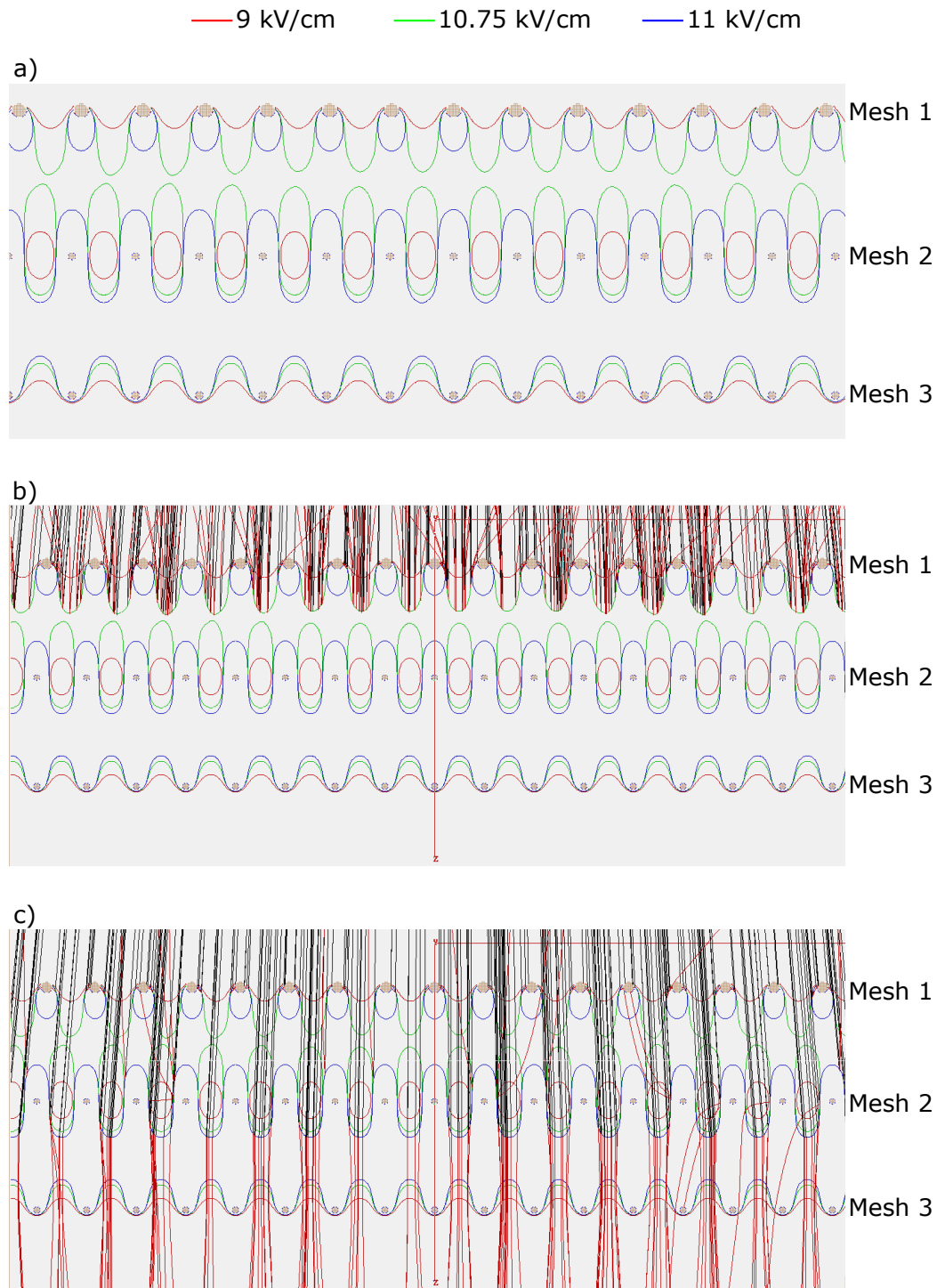


FIGURE 5.27: The equipotentials and trajectories generated in SIMION.  $\text{Ps}^*$  (black) and  $e^+$  (red) trajectories are shown in b) and c). a) A cross-section of the wire mesh system and the equipotentials generated with mesh-1 and mesh-3 held at 0V and mesh-2 held at 10kV. b) Trajectories for  $\text{Ps}^*$  that ionize in a 10.75kV/cm field,  $e^+$  are reflected. c) Trajectories for  $\text{Ps}^*$  that ionize in a 11kV/cm field,  $e^+$  are transmitted.

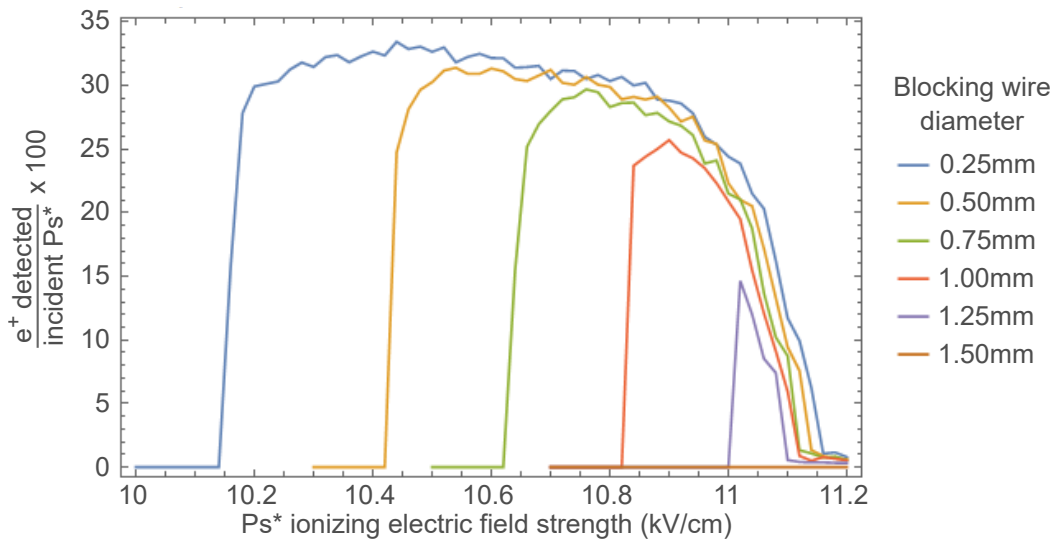
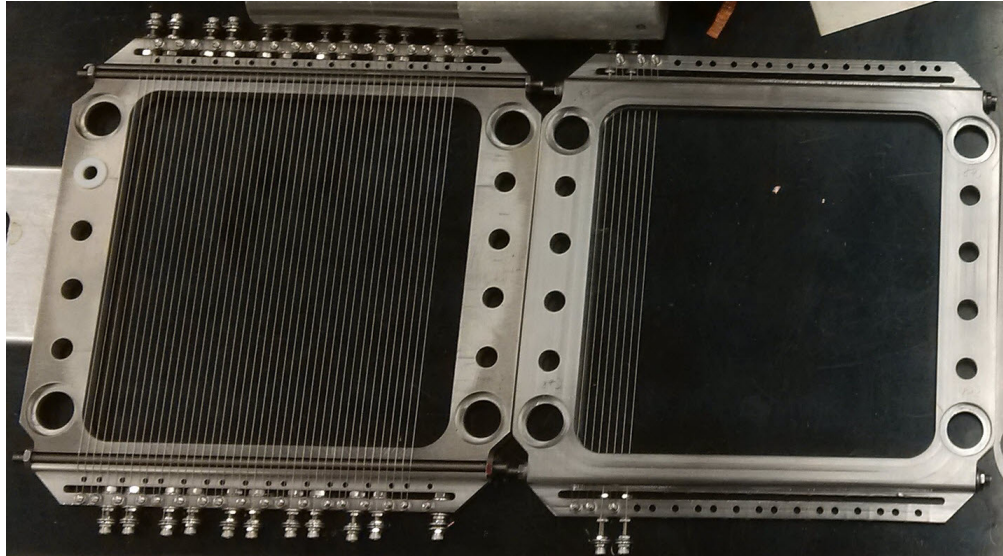


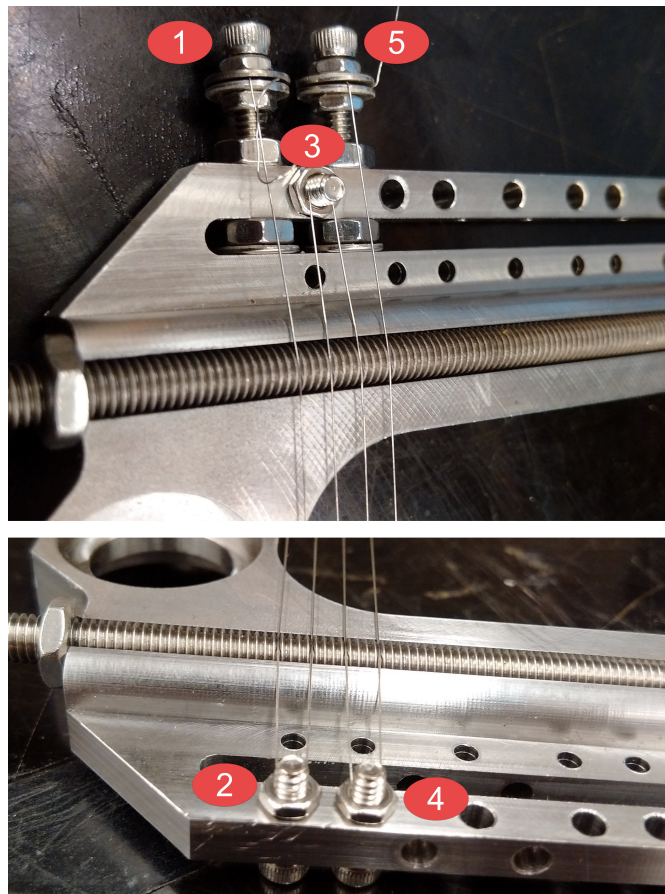
FIGURE 5.28: A Monte Carlo simulation of  $\text{Ps}^*$  sent towards the state-selective field-ionization detector. The  $\text{Ps}^*$  are programmed to ionize over a range of electric fields, and the number of ionized  $e^+$  collected on the annihilation plate are counted. The upper range of detection is due to  $\text{Ps}^*$  that do not ionize. The window of detection is dependent on the mesh-1 blocking wire diameter, where it limits how close  $\text{Ps}^*$  can get to the mesh-2 wires. The larger blocking wires limit  $\text{Ps}^*$  from experiencing highly non-uniform, strong electric fields near the mesh-2 wires and results in a narrow detection window.

the number of ionized  $e^+$  detected at the annihilation plate. This is conducted at various mesh-1 blocking wire diameters to study how the state-selection window narrows. For all blocking wire diameters, there is an upper limit of detection where the  $\text{Ps}^*$  do not ionize. For 0.25 mm diameter blocking wires, this provides the widest state-selection window since it can travel close to the mesh-2 wires where the electric field is highly non-uniform and has large electric fields. By increasing the blocking wire diameter, the electric fields observed near the mesh-2 wires become more uniform and a narrower range of  $\text{Ps}^*$  states ionize. This lead to the choice of using 1 mm diameter blocking wires since it provides a narrow range and moderately high detection fraction.

The system is constructed from a stainless steel frame that has a  $15.4 \text{ cm} \times 15.4 \text{ cm}$  opening where wires are strung across. For mesh-2 and mesh-3, 0.2 mm diameter stainless steel wire are used. A photograph of these frames during the wiring process is shown in Figure 5.29(a). The wires are spaced apart by 4 threads of a 10-32 threaded rod, resulting in a separation of 3.175 mm. A tension system



(a) Mesh-2 and mesh-3



(b) Tension system

FIGURE 5.29: Photographs of mesh-2 and mesh-3. (a) Wire mesh-2 (left) and mesh-3 (right) during the wiring process. The wires are spaced by the threads of a 10-32 rod. For mesh-2, the rod is external whereas it is internal for mesh-3. This ensures the appropriate distance the plane of wires between each frame. (b) The tension system for mesh-2 and mesh-3. The points of contact are numbered. Points 1 and 5 are raised to apply additional tension to the wires. Points 2, 3 and 4 are turning points for the wires.

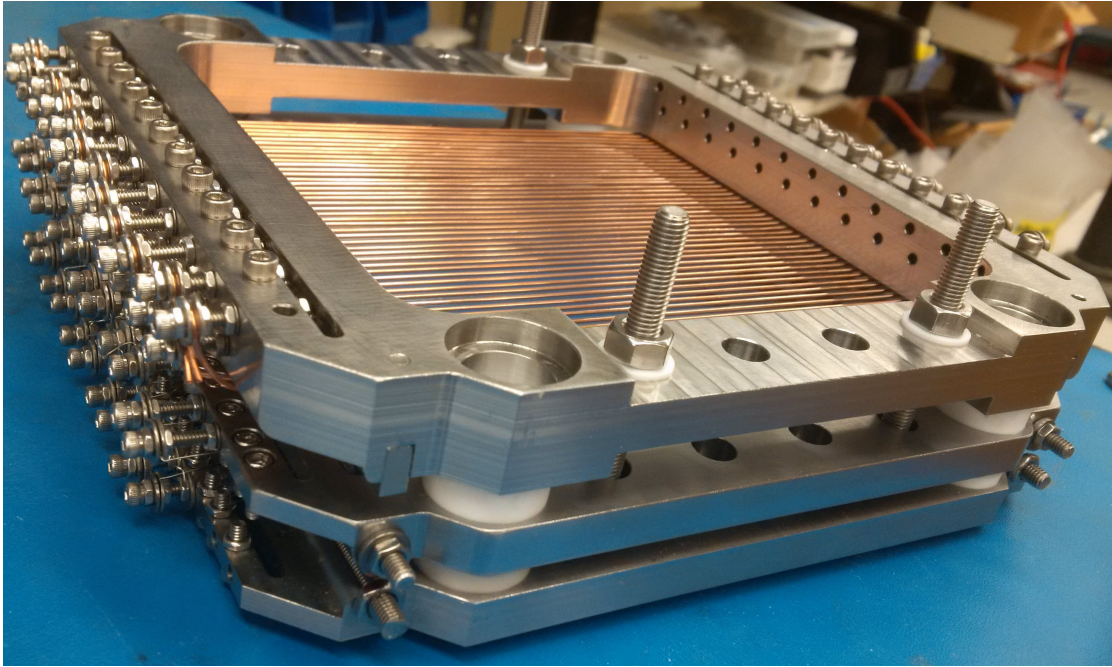


FIGURE 5.30: The assembled state-selective field-ionization detector. The frames are aligned and separated by Macor spacers such that each frame can be individually biased. The top frame is mesh-1 that contains 1 mm diameter copper wire, and the frames below contain 0.2 mm diameter stainless steel wires.

adjusts the tension for every group of 4 wires to ensure straightness (shown in Figure 5.29(b)). For mesh-1, 1 mm diameter copper wires are spaced apart by holes in a precisely machined stainless steel bar. For these wires, every group of 2 wires are tensioned with the tension system. The frames are aligned and separated by Macor spacers such that a bias can be applied to each frame (see Figure 5.30 for a photo of the assembly).

A mounting system and lens system has been prepared such that the SS-FI detector can be installed in a separate vacuum system. Upon successful  $\text{Ps}^*$  detection using the quadrupole guide, the guide can be replaced with the SS-FI vacuum system to perform RF spectroscopy and state-sensitive detection of the  $\text{Ps } 11^3\text{S}_1$  state.

## 5.8 Data Acquisition

The coincidence annihilation events are based on the techniques discussed in Section 2.1.1. The use of coincidence detection eliminates a high rate of false events

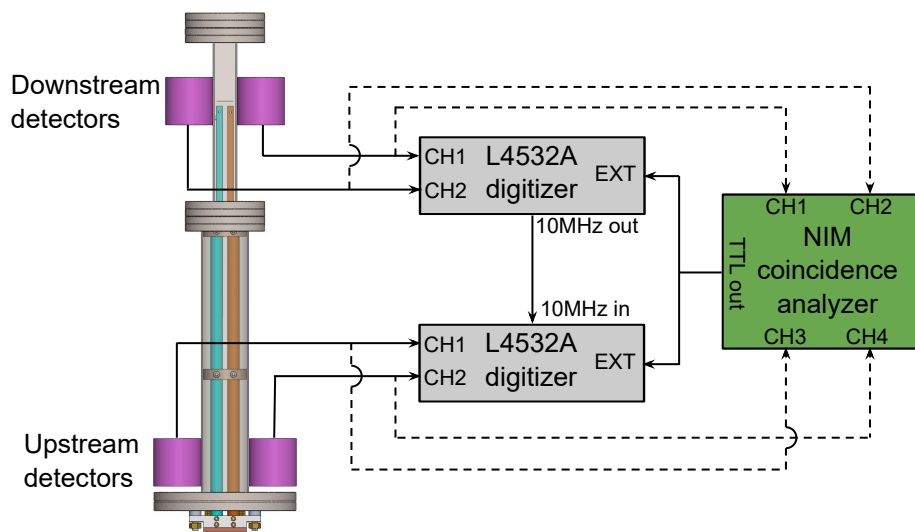


FIGURE 5.31: An overview of the data acquisition system for coincidence annihilation detection. The outputs of each detector are inputted to the NIM coincidence analyzer system (refer to Figure 2.1 for additional details). If any detector pair has a coincidence signal, the NIM system outputs a trigger to start the acquisition for both digitizers. The digitizer records the raw output signal from each gamma detector simultaneously and transfers the data to the computer for post-analysis.

from single-photon detection and localizes the detection volume to the space between a detector pair. The outputs of the SiPM are sent to the NIM detection modules for hardware coincidence detection and a pair of 2-channel digitizers (Agilent L4532A). The digitizers are synchronized to the 10 MHz clock reference of the master digitizer and have a 20 MSa/s sampling rate (50 ns/Sa). An overview of the system is shown in Figure 5.31. The upstream and downstream SiPM detector signals are assigned to each digitizer. The digitizers are simultaneously triggered on the rising edge of an external trigger, recording 20 samples. This record length (1  $\mu$ s) is sufficient to capture the full spectrum of a single gamma signal. The digitizers store up to 1024 records until they are transferred to the computer. The NIM modules produce a trigger signal when a coincidence is detected between either the upstream (US) or downstream (DS) detector pairs.

For the  $\text{Ps}^*$  trials using the ramped  $e^+$  beam, the data acquisition begins at the start of the ramp and ends when the ramp is complete. Each record is timestamped relative to the start of the ramp for timing cuts for the expected signal time window

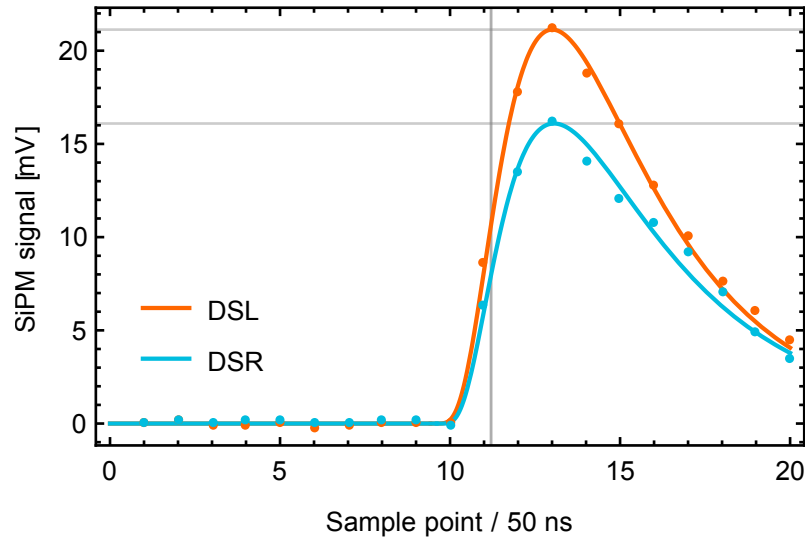


FIGURE 5.32: A raw sample coincidence signal between detectors DSL and DSR with the x-axis in terms of digitizer samples. The vertical grid lines denote the sample location where the signal has risen to the half-maximum value ( $t_{1/2}$  in sample units) and the horizontal grid lines are at the location of the fit maximums  $\gamma_{max}$ .

and background time window. The data is post-analyzed to ensure that each record contains a single coincidence event between a detector pair and removes any event where 3+ detectors received a gamma signal. A 3+ detector event typically corresponds to a shower of high-energy particles from a cosmic ray entering the atmosphere. A threshold voltage amplitude of 5 mV is set on any detector signal to proceed in the analysis. A cosmic background cut is then applied for signals exceeding 40 mV, which is far beyond the characteristic voltage produced from the  $e^+$  annihilation photopeak. The coincidence timing between the rising edges is also post-analyzed to ensure a strict time delay between the half-maximum value on the rising edge of the coincidence signals. A sample coincidence is shown in Figure 5.32. The amplitude of gamma signals are analyzed for each event, and the events are sorted to the expected signal time window and the expected background time window.

The gamma signals are fit to a logarithm-modified Gaussian with the form

$$\gamma(t) = \frac{A}{2\pi} \exp[-(\ln(t - t_0) - \mu)^2 / (2\sigma^2)] \quad (5.16)$$

Detector Fit Parameters				
Detector	$\mu$ [Sa]	$\sigma$ [Sa]	Time delay [ns]	Photopeak range [mV]
DSL	0.599(2)	1.282(2)	(-2.8, 11.3)	(20.46, 25.64)
DSR	0.645(2)	1.234(4)		(14.91, 18.86)
USL	0.593(2)	1.294(3)	(-10.9, 3.0)	(19.22, 25.72)
USR	0.570(2)	1.262(2)		(17.08, 22.76)

TABLE 5.2: The fit parameters used for each detector characterized by  $\mu$  and  $\sigma$ . The time delay window between left and right detectors where they pass the cut are listed. The photopeak detection window is also listed for each detector.

where  $A$  is an amplitude factor associated with the gamma energy,  $t_0$  is the start time of the signal,  $\mu$  is associated with the skew of the Gaussian, and  $\sigma$  is a width parameter. The value of  $\mu$  and  $\sigma$  is dependent on the characteristics of each NaI(Tl) scintillator. The ramped  $e^+$  beam is magnetically guided through the system and annihilated at the US and DS detectors. A large dataset of  $e^+$  gamma signals (>1000 events per detector pair) are fit to the four-parameter function  $\gamma(t)$  for each detector to extract an average value for  $\mu$  and  $\sigma$ . These values are subsequently used for all gamma signal fit to reduce the computation to a two-parameter fit and are listed in Table 5.2. The time at which the signal rises to the half-maximum value on the rising edge is analytically determined from the fit with

$$t_{1/2} = t_0 + \exp \left[ \sigma - \mu \sqrt{2 \ln 2} \right] \quad (5.17)$$

The time delay between the right detector signal relative to the left detector signal is measured with the difference in  $t_{1/2}$ . The distribution of time delays is fit to a Gaussian distribution (see Figure 5.33) to extract the  $1/e^2$  time windows for the time-cut. Coincidence signals that are outside of this window are removed due to this cut. The systematic effect that causes a shift of the Gaussian center from zero is due to unequal coaxial cable lengths between the detectors in a pair. The signal transmission is on the scale of 1 ft/ns, where a  $\sim 4$  ft cable length difference is reasonable.

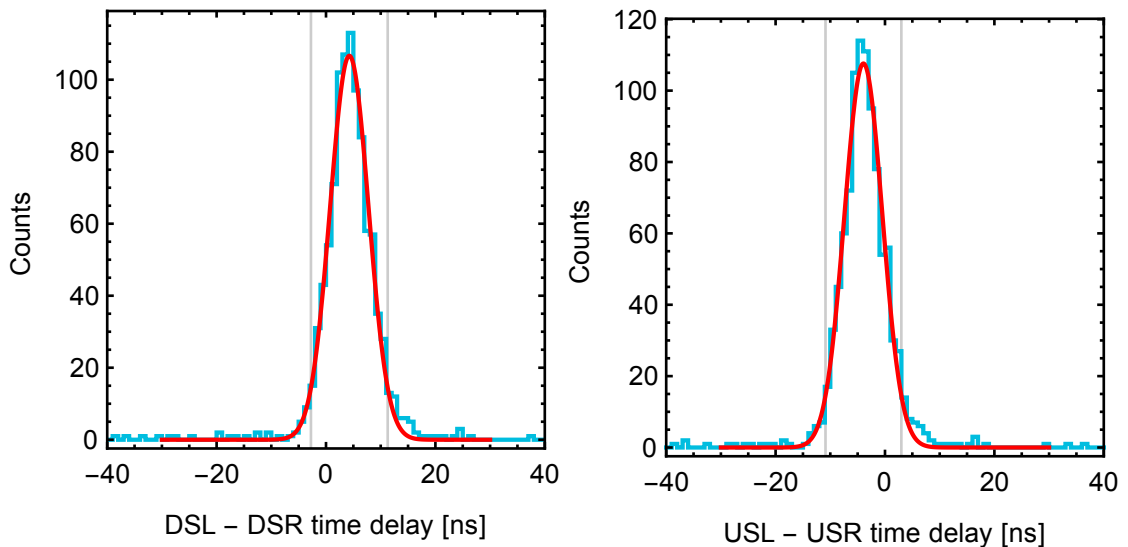


FIGURE 5.33: The time delay between  $t_{1/2}$  of the right detector signal relative to the left detector signal for the respective detector pair. The binned histogram distribution is shown in blue (1 ns bins) and the Gaussian fit is shown in red.

The amplitudes of the gamma signals are linearly proportional to the energy of the gamma-ray deposited in the scintillator. The amplitude of the gamma signals is analytically computed from the fits with

$$\gamma_{max} = \gamma(t)|_{t=t_0+\exp(\mu)} \quad (5.18)$$

The dual-gamma energy spectrum due to  $e^+$  annihilations is plotted to visualize the spectrum between a detector pair and to obtain energy cut regions. The scatter plots along with histogram distributions are shown in Figure 5.34. The distributions show the expected features from gamma annihilations, where most of the gamma energy is centered on the photopeak, and a smaller fraction is distributed over a low energy range due to Compton scattering. For a  $e^+$  annihilation, the photopeak is centered at 511 keV which is used to calibrate the detector output voltage scale to energy. The photopeak from each detector histogram distribution is fit to a Gaussian to extract the center position and the  $1/e^2$  position on each side for the energy cut window. The energy cut windows are also tabulated in Table 5.2.

In Figure 2.17, the scatter plot is divided into regions according to this energy cut. Cut A is the photopeak region where both 511 keV gamma rays deposited the full energy into each detector. This region has the largest signal-to-noise relative to the number of hits in the occupied “energy area”. Cut B is the single-Compton scatter region where one out of the two 511 keV gamma rays Compton scattered and deposited a fraction of its energy in one detector, and the other deposited the full energy in the second detector. Cut C is where both 511 keV gamma rays Compton scatter and deposit a fraction of the energy into the detectors. This  $e^+$  reference data also provides an expected ratio of signals in each cut region.

The background coincidence gamma distribution can also be studied in the same way to determine the expected ratios in each cut region defined by the  $e^+$  annihilation photopeak. The distribution is shown in Figure 5.35 where the data is collected over 10.9 hours. The background in each cut region follows a Poisson distribution with the mean rate denoted in the figure. The largest background rate is in cut C, followed by cut B. The  $e^+$  photopeak region cut A has the lowest background rate with  $14(1) \text{ hr}^{-1}$  for the downstream detector pair and  $3.3(6) \text{ hr}^{-1}$  for the upstream detector pair.

A false coincidence can occur from a pair of uncorrelated  $e^+$  annihilations with a photons trajectories directed towards the detector pair, or a single photon that Compton scatters between the pair, and these events arrive within the time-cut. A depiction of these events is shown in Figure 5.36. A majority of false coincidences are two 511 keV photons that Compton-scattered in the direction of the detectors which contribute to the background in cut C for the upstream detector. The downstream pair is shielded with 5 cm of lead on one side facing towards the charge-exchange to attenuate false coincidences and has a small solid angle for the detection of these events. In the rare event that two uncorrelated photons are directed to the downstream detector pair, the lead shielding attenuates and absorbs the photons leaving cut A unaffected from this event-type. Lead has a half-value layer of 4 mm, providing an attenuation 99.98% that essentially attenuates all incident 511 keV (including Compton scattered) photons. The background coincidence rate due to cosmic background gamma rays can be further reduced in

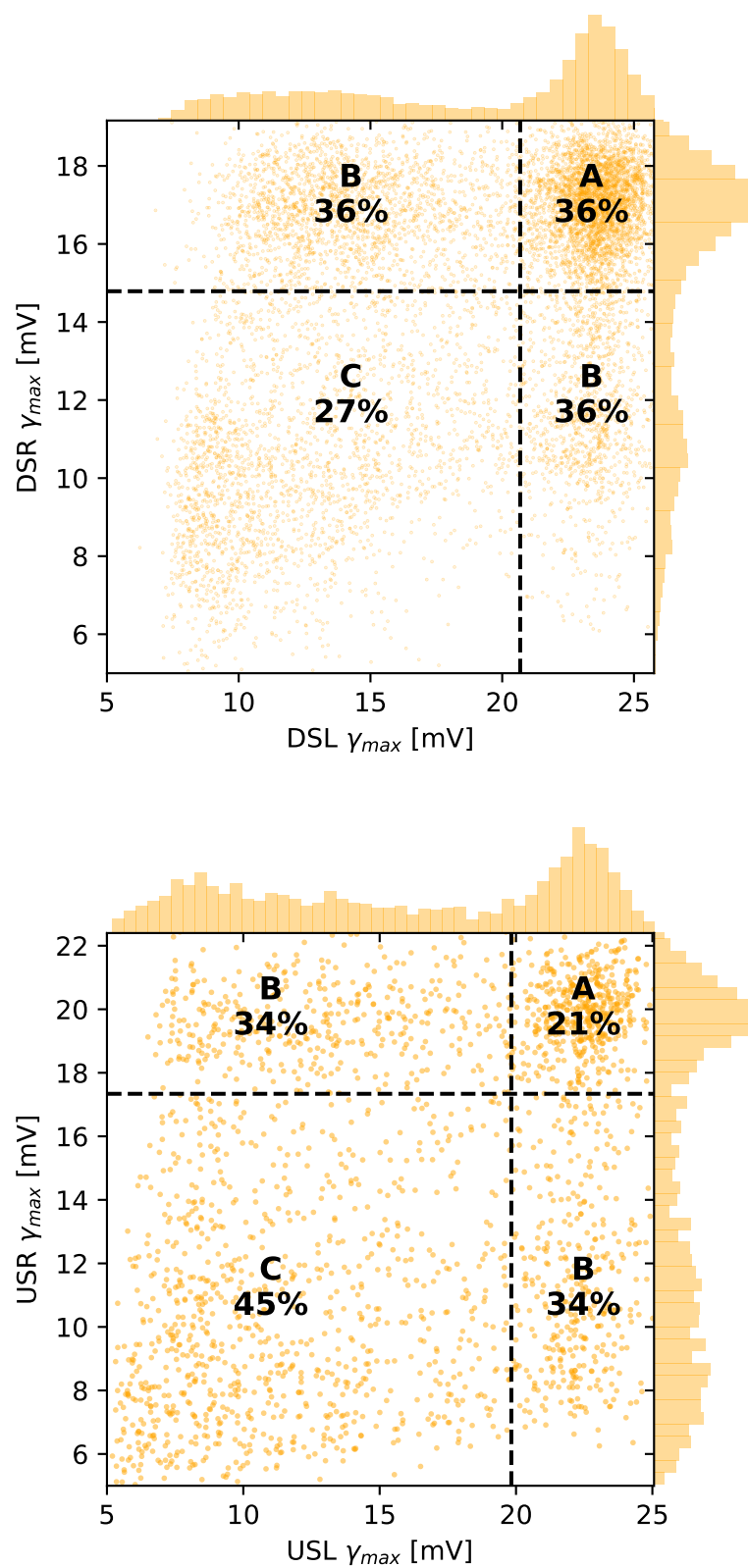


FIGURE 5.34: The coincidence gamma spectrum for each detector pair due to  $e^+$  annihilation. The dashed lines separate the various energy cut regions. The expected percentage distribution in each cut region is noted.

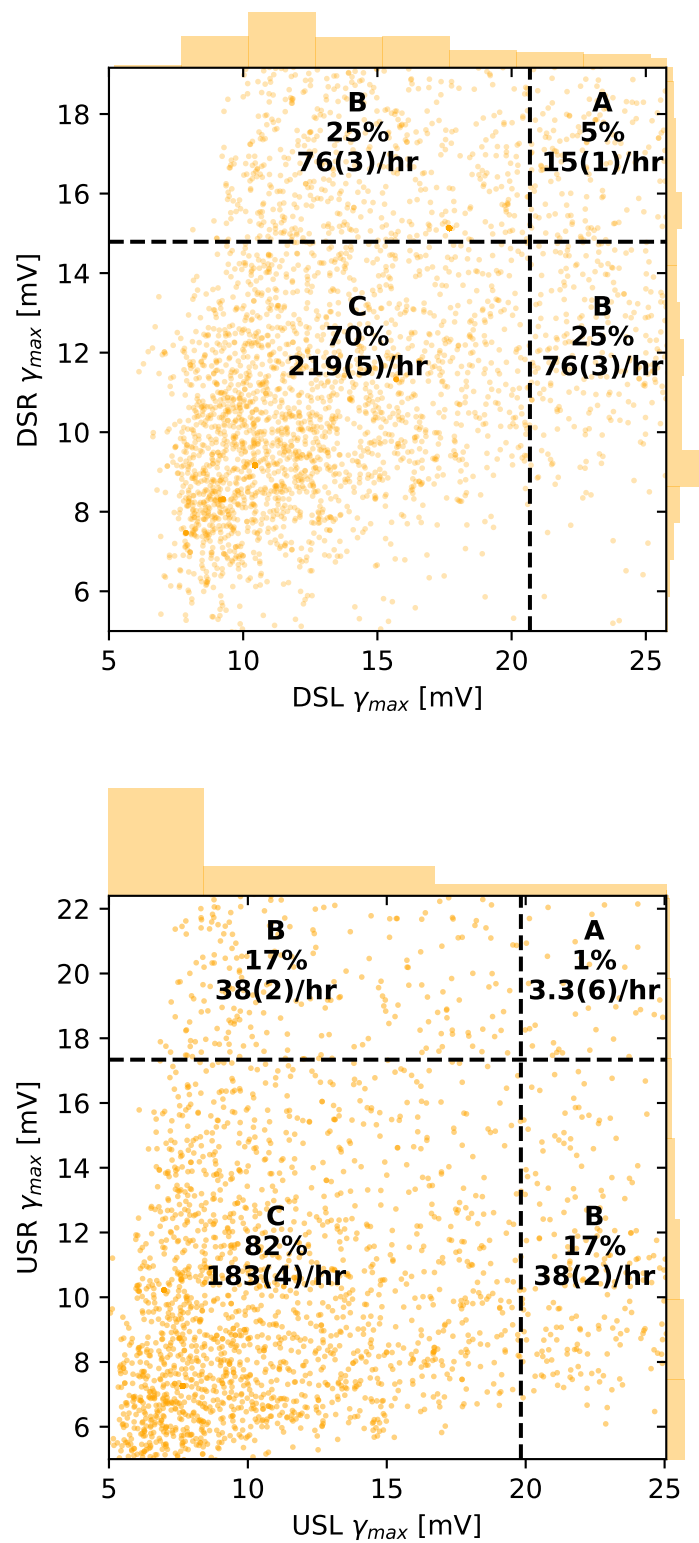


FIGURE 5.35: The coincidence gamma spectrum for each detector pair due to background. The dashed lines separate the various energy cut regions from the  $e^+$  reference data. The expected percentage distribution and rate in each cut region is noted.

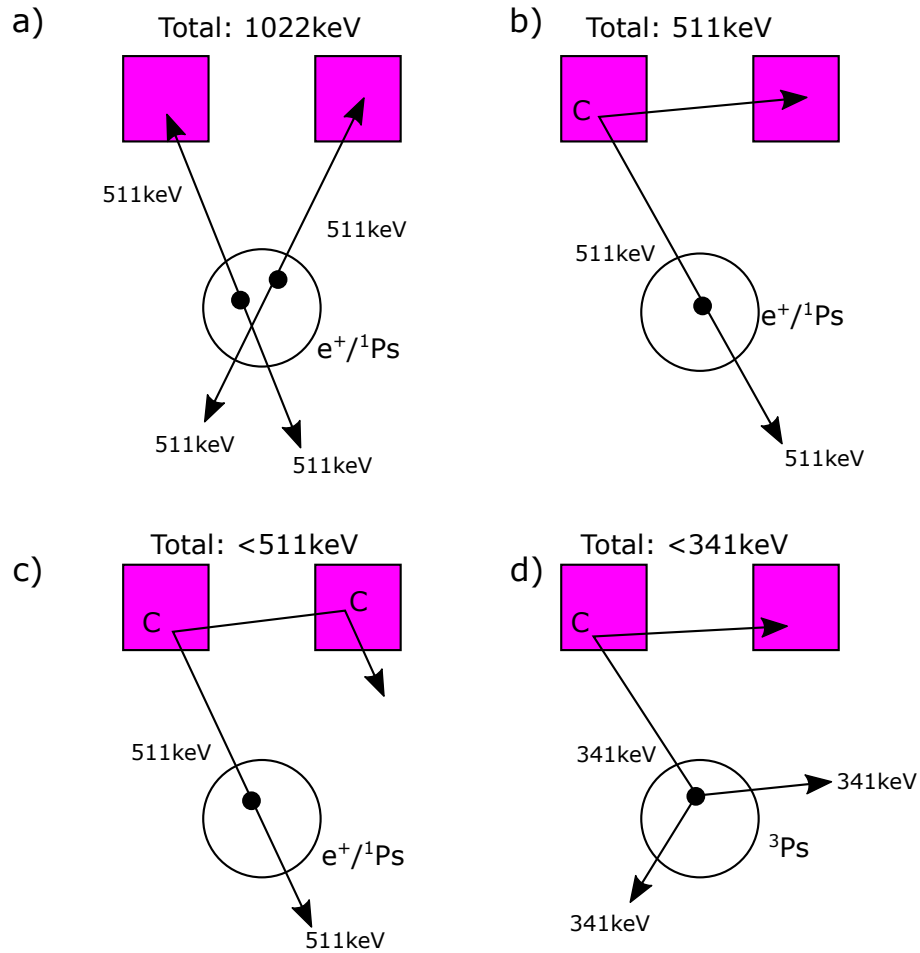


FIGURE 5.36: A depiction of uncorrelated annihilation events that are detected as a false coincidences. The events shown are a) two  $e^+$  annihilations that deposit the full 511 keV energy b) a single 511 keV photon Compton scatters in one detector and deposits the remaining energy in the other detector c) a single 511 keV photon Compton scatters in both detectors d) A triplet-state Ps decays into three 341 keV photons, one photon Compton scatters in a detector and the remaining energy is deposited in the other detector. C: a Compton scatter vertex.

the future with lead shielding surrounding the remaining five faces. A large fraction of  $e^+$  guided towards the charge-exchange location annihilate on a nearby surface and a distribution of false-coincidences due to uncorrelated Compton-scattered photons appears on the un-shielded upstream detector pair due to the proximity and larger solid angle of detection for these types of events.

The timing that the ramped  $e^+$  are released from the trap is studied by the trigger timestamps. The  $e^+$  are guided and annihilated in the detection region to obtain an expected time window for a Ps signal during a production trial. For a

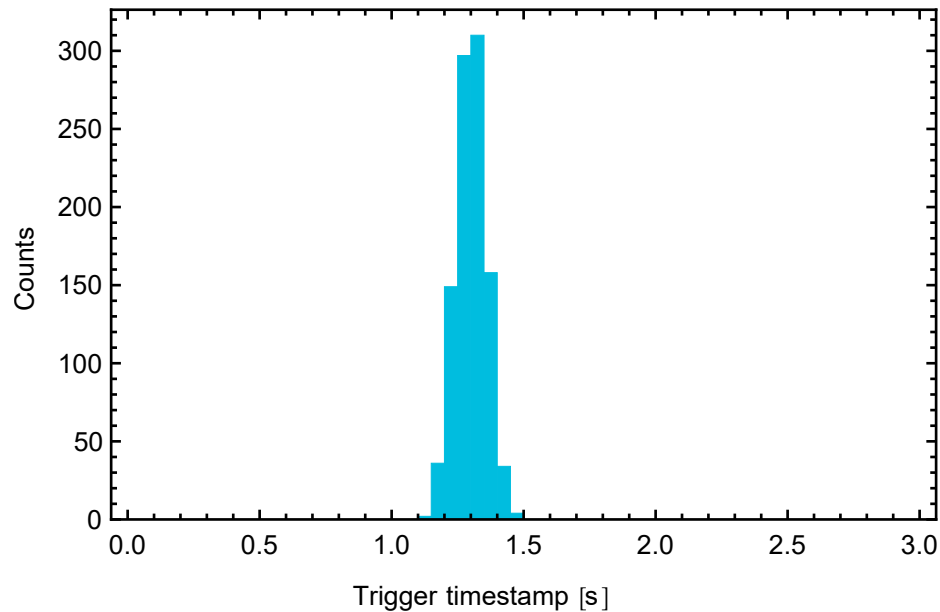


FIGURE 5.37: The time that the ramped  $e^+$  beam is released during a 3 s ramp out from the  $e^+$  trap. Each bin is 0.05 s wide. The majority of the  $e^+$  are released from the trap between 1 s to 1.6 s. This time window is the expected time that  $\text{Ps}^*$  is produced, and is considered the “signal time window”. The remaining time is the “background time window” where  $\text{Ps}^*$  is not expected to be produced.

typical ramp over 3 s, the distribution of triggers is shown Figure 5.37, where the distribution is peaked at 1.3 s. A window of 1 s to 1.6 s is set as the “signal time window” and the remaining time before and after the signal time window is used as a “background time window” that contains the low background rate of cosmic background coincidences.

In summary, the post-analysis procedure is as follows:

1. Load data file containing digitizer traces of DSL, DSR, USL, USR gamma signals and trigger timestamps for a single trial.
2. 3+ detector event cut: Remove events with 3+ detector signals with  $<5$  mV amplitude.
3. Cosmic threshold cut: Remove events with an amplitude exceeding 40 mV.
4. Sort events belonging to the downstream (DS) and upstream (US) detector pair based on raw trace amplitude.

5. Apply gamma signal fit  $\gamma(t)$  to extract the time delay of the right detector relative to the left detector.
6. Coincidence cut: Remove event if the time delay is out of the range listed in Table 5.2.
7. Extract amplitude based on  $\gamma(t)$  fit.
8. Categorize coincidence signals to energy cut windows A, B, C based on detector photopeak range listed in Table 5.2.
9. Categorize coincidences signals to background/signal time window based on trigger timestamp.

### 5.8.1 Detection of Triplet Ps Formation on Metal Surface

The  $e^+$  guided towards the copper plate in the detection region mostly annihilate on the surface, but a small fraction thermalizes within the metal and captures an  $e^-$  at the surface to form singlet and triplet Ps in the ground state. The Ps formation potential  $\epsilon_{Ps}$  is described as

$$\epsilon_{Ps} = \phi_+ + \phi_- - 6.8 \text{ eV} \quad (5.19)$$

where  $\phi_+ = -0.4 \text{ eV}$  is the  $e^+$  work function for copper,  $\phi_- = 4.65 \text{ eV}$  is the  $e^-$  work function for copper, and  $6.8 \text{ eV}$  is the Ps ground state binding energy. For copper, the formation potential is  $\epsilon_{Ps} = -2.55 \text{ eV}$ , where the Ps atom has a kinetic energy  $\leq -\epsilon_{Ps}$  [73].

The decay of the singlet state emits two back-to-back gamma photons of  $511 \text{ keV}$  that cannot be distinguished from a  $e^+$  annihilating with a surface  $e^-$ , however the triplet state annihilates into at least three photons where the total photon energy is  $1022 \text{ keV}$ . This has a unique gamma spectrum. The angular probability distribution is maximized for the three photons to be separated by  $120^\circ$ , corresponding to photon energies of  $\frac{1}{3}(1022 \text{ keV}) = 340.7 \text{ keV}$ .

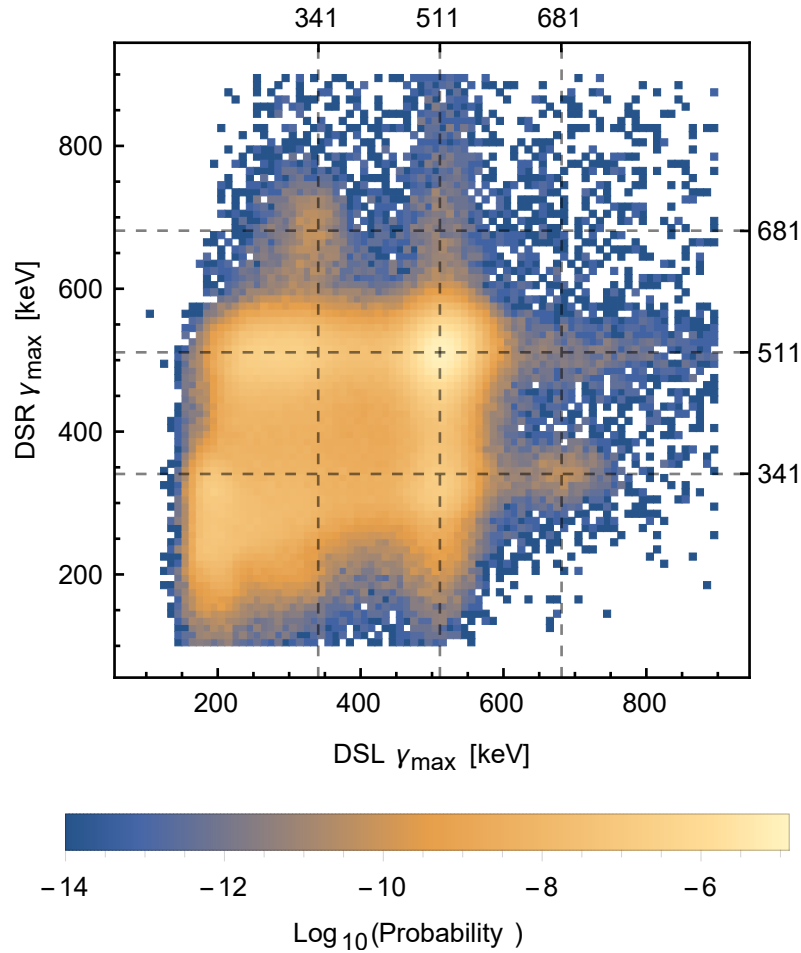


FIGURE 5.38: A density histogram plot of the downstream detector pair coincidence gamma spectrum beyond the photopeak region reveals additional clusters due to triplet Ps annihilation. The colours represent the logarithm of the probability for each bin.

The downstream detector pair layout allows for the absorption of 2 out of 3 photons in one detector and 1 out of 3 in the other, and vice-versa. This corresponds to a coincidence detection of a total photon energy  $2(340.7 \text{ keV}) = 681.3 \text{ keV}$  in one detector and  $340.7 \text{ keV}$  in the other. The decay of the triplet Ps atoms is apparent in Figure 5.38 where clusters of signal are shown at  $(\text{DSL}, \text{DSR}) = (340.7, 681.3) \& (681.3, 340.7) \text{ keV}$  that comprise of 0.6% of the total signal. This allows for the option to search for signals in this “triplet decay” region. This region is also a candidate for RF spectroscopy, where a cluster of signal in this region can only be due to triplet Ps annihilation.

## 5.9 Rydberg Positronium Production Trials

To prepare the system for a  $\text{Ps}^*$  production trial, the  $e^+$  steering is optimized to maximize the number of  $e^+$  guided through the nozzle and the quadrupole guide. The nozzle, cold trap, and quadrupole entrance aperture are set to 0 V to transmit the 40 eV ramped  $e^+$  beam. The magnetic field coils along the quadrupole guide are turned on to produce a guiding magnetic field to annihilate the  $e^+$  on the annihilation plate.

The magnet current parameters are initially optimized using the 40 eV moderated  $e^+$  beam at a low source magnetic field where it has a small diameter Gaussian distribution as discussed in Section 3.2. The moderated and ramped  $e^+$  beam is expected to follow nearly identical paths as long they share similar kinetic energy, and the moderated beam traverses the position of the trapped  $e^+$  during an accumulation.

The positioning of the in-vacuum coil is carefully studied to maximize the amount guided into the system and steered through the cold trap input hole. The moderated beam is guided through the quadrupole and annihilated on the annihilation plate where a continuous coincidence annihilation rate is monitored while optimizing magnet parameters. This is an automated process that randomly iterates through the magnet coils and adjusts the current to maximize the rate.

With a rate detected from the moderated beam, the system operation is switched to the ramped  $e^+$  beam with minor traverse magnetic field corrections along the transfer guide. The minor corrections account for the inexact alignment of the moderated beam through the trap center. The ramped  $e^+$  beam is guided to the detection region and the total number of triggers is counted using the data acquisition system. The magnet current settings are optimized to maximize the total trigger count. The trends for a select group of magnetic field coils are shown in Figure 5.39. The ramped  $e^+$  beam contains 1.5 million  $e^+$  after a 5 s accumulation. Approximately 10% of these transmit through the cold trap input hole and can traverse through the charge-exchange region and quadrupole guide towards the

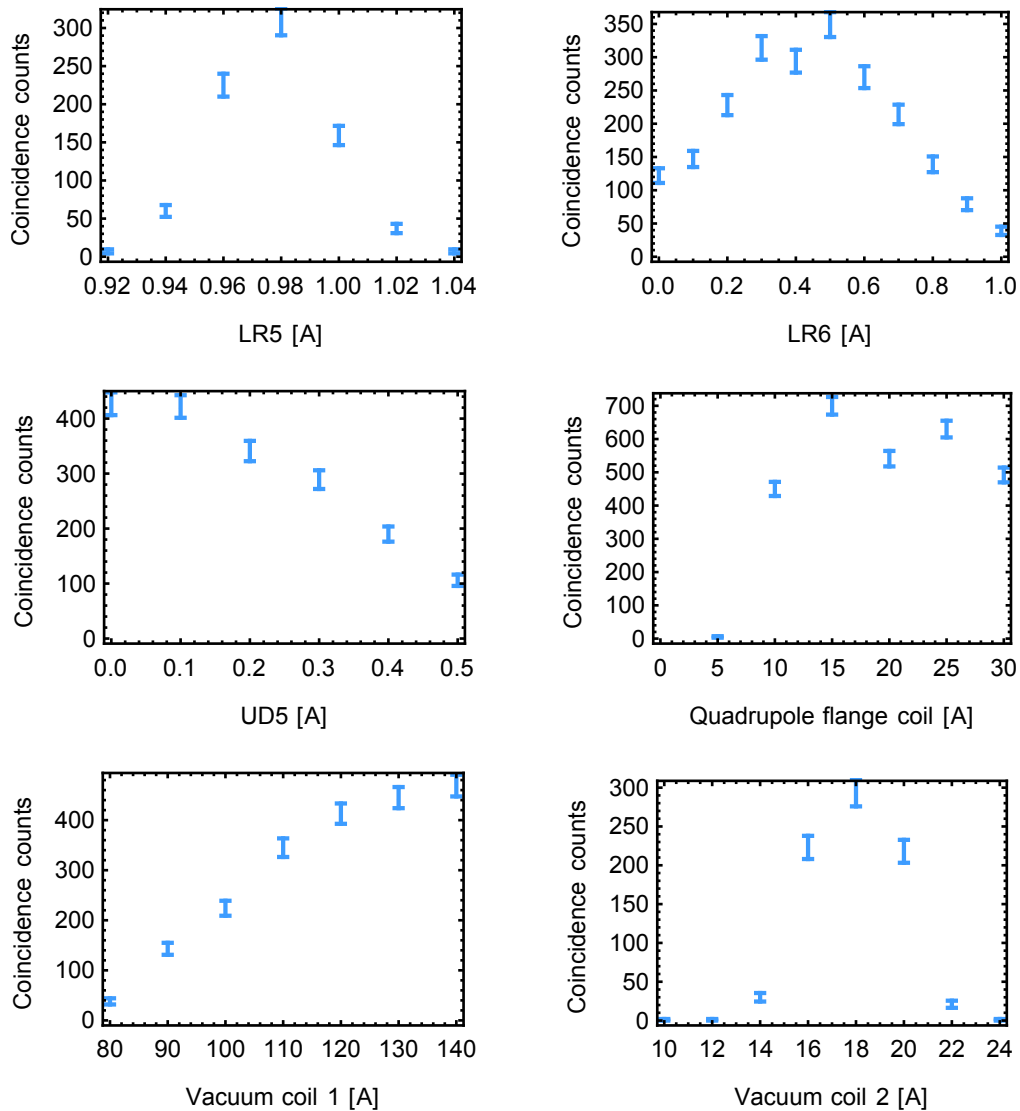


FIGURE 5.39: The number of coincidence triggers at the detection region for various magnet coil settings using the ramped  $e^+$  beam. The currents are optimized to maximize the number of counts.

detection region. From the plot trends, up to 700 triggers are detected. This is below the 1024 record limit per acquisition, and the low number is related to the single-photon detection efficiency of each detector.

The single-photon detection efficiency for the SiPM gamma detector is calibrated with  $1.5 \times 10^6 e^+$  annihilated on the phosphor screen and with a detector located 36 cm away. For comparison, the  $e^+$  number is counted on the Faraday cup located behind the phosphor screen when it is translated out of position. The SiPM detector subtends 0.13% of a full solid angle. The SiPM has a 410 nm photon

detection efficiency of 45%, a 30% coverage of the NaI(Tl) optical window, and the scintillator has a 65% absorption efficiency for 511 keV, corresponding to an expected 9% net efficiency. The SiPM detects on average 330(20) triggers based on a Poisson distribution for repeated trials. The total  $e^+$  number can be inferred based on the efficiency losses and the solid angle coverage following the formula

$$N_{single,est} = \frac{330}{(0.09)(0.0013)(2)} = 1.4 \times 10^6 e^+ \quad (5.20)$$

which is similar to the number of counts from Faraday cup detection. The factor of 2 accounts for the fact that each annihilation produces two gamma photons. For coincidence measurements, the dual-detector efficiency is a product of the individual efficiencies,  $9\% \times 9\% = 0.8\%$ . Accounting for the 60% solid angle coverage, the estimated number of  $e^+$  arriving at the detection region is

$$N_{coin,est} = \frac{700}{(0.008)(0.6)} = 1.4 \times 10^5 e^+ \quad (5.21)$$

which is 10% of the initial amount of  $e^+$  indicating that there are losses from apertures and guiding within the Ps apparatus. The overall coincidence detection efficiency is 0.5%, where there is room for a large improvement in the SiPM coverage of the NaI(Tl) optical window. The overall efficiency for a downstream Ps detection in the photopeak window (cut A) is  $(0.005)(0.36) = 0.2\%$ , leading to approximately 1/500 Ps atoms that are detectable.

The  $e^+$  are ramped over a barrier with 38.0 V applied to three consecutive electrodes, producing an estimated on-axis potential of 37.9 V. With the magnet current settings optimized to transmit the largest amount of ramped  $e^+$  through the charge-exchange, the  $e^+$  speed is reduced at the charge-exchange by applying an electric potential on the nozzle. The cold trap is held at 36.5 V to reduce the electric potential gradient near the nozzle. A sample scan of the nozzle bias is shown in Figure 5.40 where the energy distribution is peaked at 37.53(8) eV with a FWHM of 0.5(1) eV. The center of the nozzle where the charge-exchange

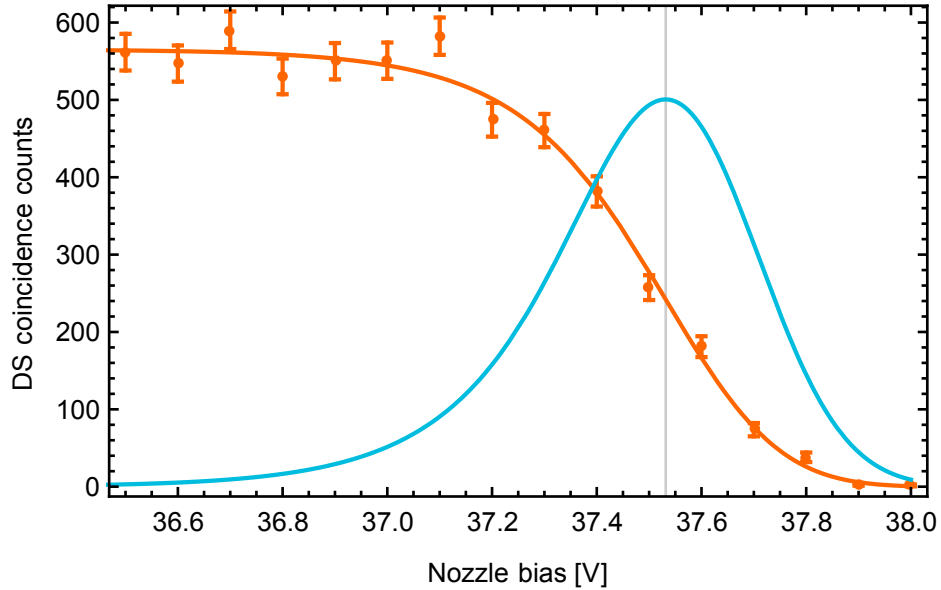


FIGURE 5.40: A scan of the blocking potential applied on the nozzle and the reduction of the coincidences detected on the downstream detector pair (orange). The derivative of the curve (shown in blue) represents the energy distribution of the ramped  $e^+$  beam (normalized, re-scaled for clarity).

takes place experiences 99.9% of the applied potential, indicating that the beam energy is centered on 37.48(8) eV which is in close agreement with the estimated kinetic energy upon exiting the  $e^+$  trap. The apparent broadening of the energy distribution is partially due to the nozzle geometry that generates a non-uniform potential distribution and that the  $e^+$  beam samples a large volume within the nozzle cage. The charge-exchange is expected to occur in a width of 100 meV, leading to an estimate that 20% of the incident  $e^+$  are usable for charge-exchange. For a ramped Ps trial, this corresponds to approximately 25 000  $e^+$  per trial.

The Ps\* is produced in an isotropic distribution with at most 1.3% being captured ( $13^\circ$  half-angle cone towards the guide) and  $\sim 50\%$  (that are in a low-field seeking state) being guided by the quadrupole. At the initial 370 K oven temperature, 1% of the useful  $e^+$  will charge-exchange with a Rydberg Cs atom. Including detection efficiency, an average of 350 trials will produce 1 Ps\* atom detected on the downstream detector pair in the photopeak region. The expected background after this many trials is 1.3 background hits in the photopeak region.

To initiate a Ps\* production trial, the nozzle bias potential is set to 37.5 V to slow the  $e^+$  to an average velocity of zero. The quadrupole aperture is biased

Ps Trial Hits Cut [A, B, C], 396.6 s Signal Time Per Experiment					
Det.	Laser	0 V	$\pm 900$ V	$\pm 1900$ V	Expected background
DS	ON	[1, 7, 20]	[3, 6, 33]	[1, 12, 25]	[1.2(1), 7.3(3), 25.1(5)]
	OFF	[1, 6, 18]	[0, 9, 26]	[0, 7, 28]	
US	ON	[5, 68, 870]	[9, 68, 832]	[9, 73, 840]	[0.40(7), 4.7(2), 19.5(5)]
	OFF	[9, 51, 885]	[6, 59, 839]	[4, 55, 853]	

TABLE 5.3: The number of observed coincidences classified in the energy cuts A, B, C. The 852 nm laser is on for all trials, and the 520 nm laser is alternated on and off. The noted voltages are the voltages applied to the quadrupole rods.

to 100 V to reflect the stray fraction of  $e^+$  with enough energy to overcome the nozzle potential barrier. The magnetic field coils along the quadrupole guide are turned off since  $e^+$  are no longer intentionally guided and the quadrupole guide does not require a magnetic field. A plasma of  $1.5 \times 10^6$   $e^+$  are accumulated for 5 s, with 5 s to vent the nitrogen buffer-gas, and 3 s to ramp the  $e^+$  out of the trap for a total trial time of 13 s. The data is acquired during the ramp, where 1 s to 1.6 s is used as the signal time window (4.6 % signal duty cycle). The optical shutter state for the Rydberg laser is randomly alternated with the 852 nm laser on throughout, and the quadrupole voltage is randomly alternated between 0 V,  $\pm 900$  V, and  $\pm 1900$  V. The results of this trial are summarized in Table 5.3. At this low oven temperature, the signals observed in all energy cut regions for the downstream detectors are consistent with background which is due to the low expected signal rate and the potential for unaccounted loss factors.

The upstream detectors observe signals that are over 10 times the expected background rate which is attributed to false coincidences arriving at the pair. This makes the upstream pair less reliable compared to the downstream pair. The density histogram distribution for the aggregate of the laser on trials is shown in Figure 5.41. The total energy from the coincidence gamma pairs reveals that the distribution is peaked at a total photon energy of 511 keV indicating that most of the signal observed is from a single 511 keV photon Compton scattering in one detector, and the remaining photon energy is absorbed in the second detector in the pair. This can be seen in the 2D histogram distribution plot where a cluster of signals lies along the 511 keV total energy line. These are false coincidences

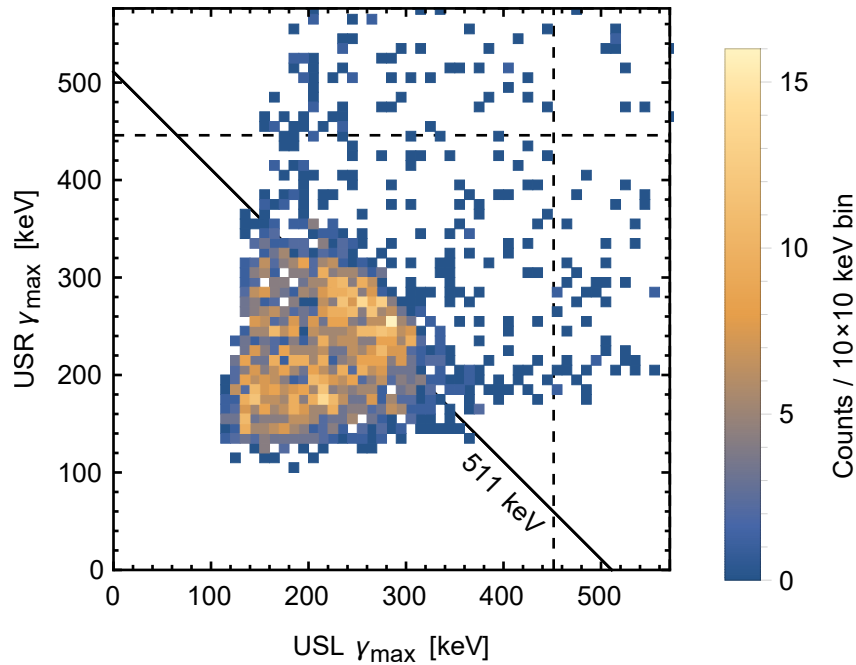


FIGURE 5.41: The 2D histogram distribution for the laser on trials. The diagonal line represents the total photon energy equating to 511 keV.

that originate from  $e^+$  annihilations with  $e^-$  within the charge-exchange vicinity, or ground state singlet Ps annihilations.

In order for a 511 keV photon that originated from the charge-exchange location to Compton scatter from one detector to the other, the photon must scatter between  $80^\circ$  to  $130^\circ$ . The results of a Monte-Carlo simulation simulating this process is shown in Figure 5.42 as the red cluster. The Compton-scattered photon also has a probability to Compton scatter in the second detector, resulting in the cluster shown in green. The production and decay of triplet Ps has the largest probability to annihilate into three photons of 340.6 keV, and a photon that Compton scatters out of one detector and is absorbed in the other results in the cluster shown in blue. The number of counts within the 340.6 keV total energy cluster does not show a significant difference between laser on and off trials, indicating that the cluster is not from Rydberg Cs charge-exchange but potentially from ground-state Cs charge-exchange producing low- $n$  triplet-Ps. This signature may be useful for studies that cause less triplet-Ps annihilations where they are extracted from the charge-exchange location and become undetected.

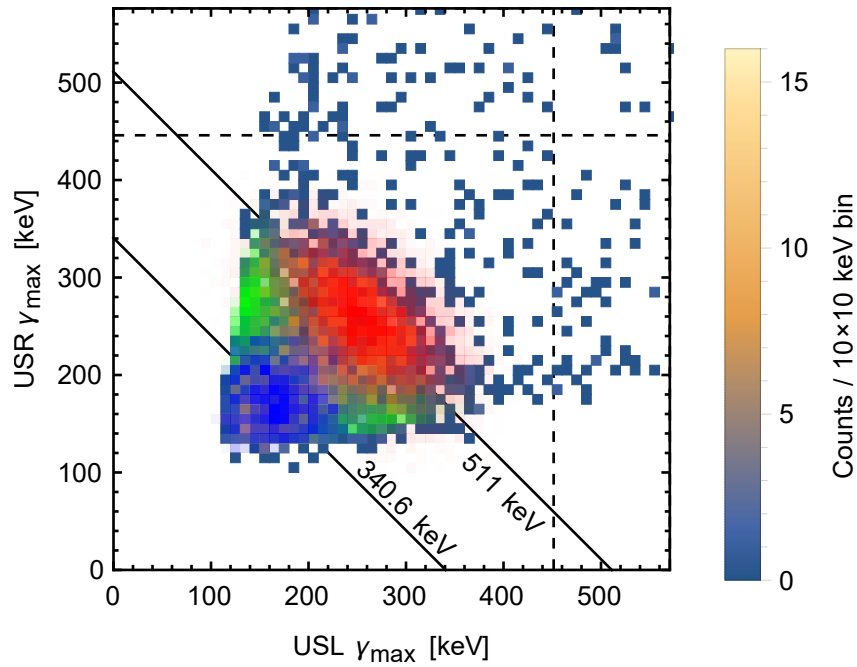


FIGURE 5.42: The cluster distributions for various Compton scattering scenarios for annihilations originating from the charge-exchange point. Red: A 511 keV photon Compton scatters out of one detector and is absorbed in the other. Green: A 511 keV photon Compton scatters in each detector. Blue: A 340.6 keV photon Compton scatters out of one detector and is absorbed in the other. The diagonal lines represent combinations of gamma energies that sum to 511 keV or 340.6 keV.

To attempt to improve the  $\text{Ps}^*$  production rate, the oven temperature is further increased from 370 K to 400 K where the expected charge-exchange efficiency should increase from 1% to 10%. The ramped  $e^+$  beam energy is re-analyzed with the nozzle bias and the transmitted  $e^+$  are magnetically guided and detected on the downstream detector pair. At the increased temperature, the nozzle bias energy scans show a difference in whether the Rydberg excitation laser is on or off. As seen in Figure 5.43, with the Rydberg excitation laser off, the ramped  $e^+$  beam energy is centered at 37.4 eV where the beam is slowed to zero average velocity. The 852 nm laser is on for both cases at the typical power of 0.1 mW. When the Rydberg excitation laser is on (8 mW) to produce  $\text{Cs}^*$ , there is a loss of guided  $e^+$  to the detection region centered around  $e^+$  beam energy with an energy width of  $\sim 100$  meV. This is consistent with the picture of  $e^+$  charge-exchanging with  $\text{Cs}^*$  to produce  $\text{Ps}^*$  that are not magnetically guided to the detector region. The fraction transmitted compared to the laser off case is also shown to account for the

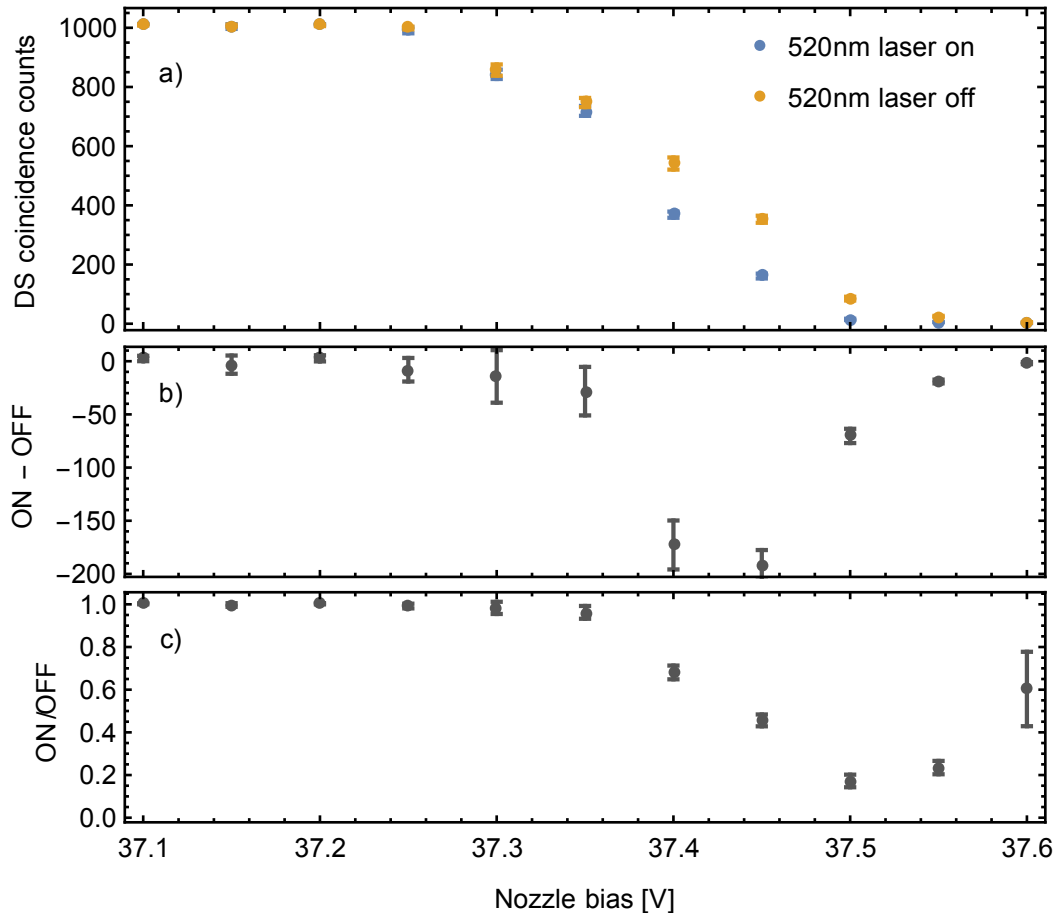


FIGURE 5.43: A scan of the ramped  $e^+$  beam energy using the nozzle as a retarding potential analyzer. a) The scan is studied with the Rydberg laser on (8 mW) and off, with the 852 nm laser on (0.1 mW) for both cases. b) The difference between the scans, indicating a loss of guided  $e^+$  with the presence of  $Cs^*$ . c) The fraction transmitted with the laser on compared to laser off.

loss of total counts from blocking. This effect is only observed with the presence of  $Cs^*$ , confirmed by blocking the 852 nm laser, and no difference observed between the Rydberg-excitation laser being on or off.

The 852 nm is increased to 1 mW and the scan is repeated as shown in Figure 5.44. It is observed that there is significantly more loss that occurs at higher  $e^+$  energies. The difference plot appears to shift to a lower energy because there are near zero  $e^+$  guided at 37.4 V such that further losses are not possible. Table 5.4 summarizes the scans with various operating parameters and notes the absolute and fractional losses observed. The loss of  $e^+$  guided to the downstream detectors is strongly dependent on the 852 nm and 520 nm Rydberg excitation laser powers and on the oven temperature. The absolute amount of loss scales linearly with the

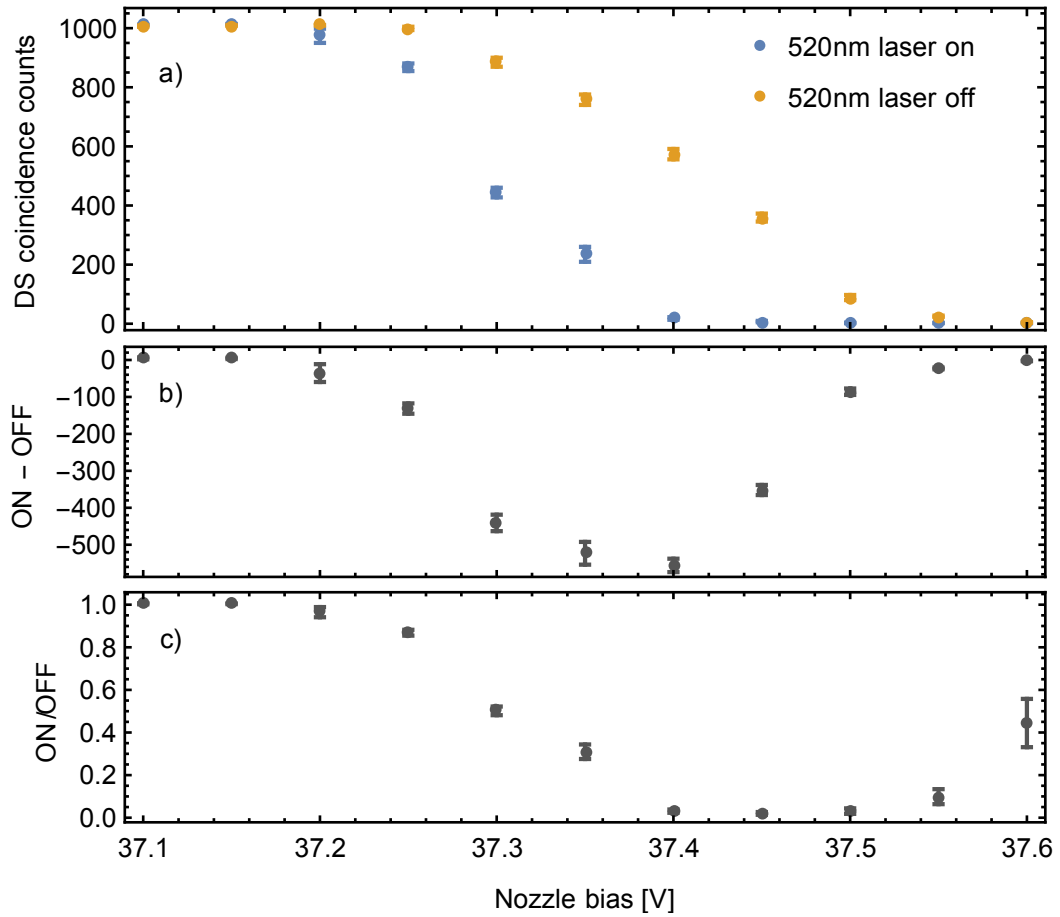


FIGURE 5.44: A scan of the ramped  $e^+$  beam energy using the nozzle as a retarding potential analyzer. a) The scan is studied with the Rydberg laser on (8 mW) and off, with the 852 nm laser on (1 mW) for both cases. b) The difference between the scans, indicating a loss of guided  $e^+$  with the presence of  $Cs^*$ . c) The fraction transmitted with the laser on compared to laser off.

number of incident  $e^+$ . At this low  $e^+$  speed, the cross-section for  $e^+$  scattering on ground state Cs atoms is much smaller than for Rydberg charge-exchange, thus the loss observed with the presence of  $Cs^*$  is attributed to  $Ps^*$  formation. The largest loss of 700 coincidence counts corresponds to 150 000  $Ps^*$  atoms in a single trial.

Approximately half of the  $Ps^*$  atoms are in a state that can be guided to the detector region, thus an upper limit of 5  $Ps^*$  atoms per trial can be detected when detection efficiencies are included. A  $Ps^*$  trial was conducted with 10 mW of 852 nm laser power, 8 mW of 520 nm laser power, with the quadrupole aperture grounded and the quadrupole rods set to  $\pm 2$  kV. A  $e^+$  that passes the aperture is immediately attracted to the  $-2$  kV rods and does not contribute to a background

Energy Scans with Various Experiment Parameters					
$P_{852}$ [mW]	$P_{520}$ [mW]	DS count	$T_{oven}$	(Max loss, %, V)	(Min %, V)
10	8	1000	400	(700, 10, 37.35)	(1, 37.45)
10	4	1000	400	(270, 50, 37.4)	(12, 37.5)
1	8	1000	400	(550, 5, 37.4)	(2, 37.45)
0.1	8	1000	400	(190, 45, 37.45)	(17, 37.5)
1	8	500	400	(270, 15, 37.35)	(2, 37.45)
1	8	800	380	(20, 90, 37.5)	(75, 37.55)
1	8	800	387	(140, 60, 37.45)	(13, 37.5)

TABLE 5.4: The results for the energy scans for various laser powers,  $e^+$  numbers, and oven temperatures using the nozzle as an RPA. The loss is measured when the Rydberg excitation laser is on during the scan. “DS count” is the amount of counts observed without a blocking potential applied to the nozzle, (Max loss, %, V) represents the data point with the largest loss of counts at voltage V, and % is the transmitted fraction. (Min %, V) is the smallest fraction transmitted located at voltage V.

for the downstream detector pair. The 520 nm laser is alternated on and off for consecutive trials. The downstream detector pair does not observe a signal significant over background, however the upstream detector pair detects a significant overall loss of coincidence counts with the Rydberg-excitation laser on. Table 5.5 summarizes the results for this trial. The coincidence gamma spectrum for the upstream pair indicates a large signal from  $e^+$  interacting with the Cs\* atoms, the nozzle, and cold trap surfaces that dominates over the expected background from cosmic background coincidences. In cut B, the significance between the Rydberg excitation laser on and off is  $6\sigma$ , and for cut C, the significance is  $14\sigma$ .

The reduction of  $e^+$  annihilations producing the upstream coincidence gamma spectrum is a partial indicator of Ps\* formation. Ps\* in an isotropic distribution has 0.244 sr (2% of  $4\pi$ ) solid angle to leave the charge-exchange region via the cold trap laser access holes and the input/output holes. The Ps\* travelling towards the quadrupole guide should have been guided towards the downstream detectors but there is no apparent signal over background. A Ps\* atom that annihilates a partial distance through the guide due to imperfections (such as rod misalignment or patch potentials) could only be detected on the upstream detectors from a false coincidence detection of a single photon scatter, however, the solid angle for an

Ps Trial Hits Cut [A, B, C], 954 s Signal Time Per Experiment			
Det.	Laser	$\pm 2000$ V	Expected background
DS	ON	[4, 10, 31]	[3.5(5), 17(1), 54(2)]
	OFF	[1, 20, 21]	
US	ON	[15, 195, 1938]	[0.7(3), 13(1), 46(2)]
	OFF	[14, 296, 2629]	

TABLE 5.5: The number of observed coincidences classified in the energy cuts A, B, C. The 852 nm laser is on for all trials, and the 520 nm laser is alternated on and off. The quadrupole rods are held at  $\pm 2000$  V for all trials.

upstream detection decreases the further it travels.

The loss of  $e^+$  requires further studies to understand the full picture. The downstream detectors have not seen a significant signal above background, therefore it may be useful to position them at a variable distance along the quadrupole guide, closer to the upstream detectors. An additional detector pair that monitors the coincident annihilations at the charge-exchange location may give another indicator of the process that occurs. A detector pair that can capture annihilations on the cold trap surfaces will be useful to observe the isotropic production of  $\text{Ps}^*$ , where a large fraction will annihilate on the cold trap walls.

These initial  $\text{Ps}^*$  trials were conducted prior to the first provincial lockdown due to the COVID-19 pandemic. Up to this point, the apparatus was maintained at liquid nitrogen cooled temperatures for over a year to collect the Cs on cryogenic surfaces. The lockdown led to an unreliable supply of liquid nitrogen and the laboratory was requested to shut down for about a half year. The cryogenic components warmed to room temperature and Cs has likely coated all surfaces of the Ps apparatus. The delay to return to the lab, the amount of work required to clean the Ps apparatus, and to restart the entire experiment would have required an additional year's worth of effort to continue the research. Because of this, plans to continue experimentation were halted at this point.

In summary,  $\text{Ps}^*$  has not been detected with the DS detectors (Tables 5.3 and 5.5), however there is an indirect detection of  $\text{Ps}^*$  around the charge-exchange region before the quadrupole guide (DS Max Loss in Table 5.4). The reason for no  $\text{Ps}^*$

detection at the DS detectors is still unknown, however, there are still many more diagnostics checks that can be performed with this apparatus.

# Chapter 6

## Conclusion

The work presented in this thesis outlines the progress made towards the production of long-lived Rydberg Ps and spectroscopic measurements of Ps\* fine structure. The apparatus developed for this research includes a system to transport cold  $e^+$  to a chamber for Ps\* production. In this Ps apparatus, an intense thermal beam of Cs is generated and is isolated by cryogenically cooled apertures to protect  $e^+$  buffer-gas accumulator. Two frequency-stabilized laser systems were developed to laser excite Cs to Cs\*. The  $e^+$  are guided and slowed at the Cs\* target to produce Ps\* by resonant charge-exchange. Ps\* from charge-exchange is detected with a coincidence gamma detection system. A state-sensitive electrostatic quadrupole Ps\* guide and technique was prepared for radiofrequency spectroscopy of the  $11^3S_1 \rightarrow 11^3P_j$  transitions.

Upgrades were made to the  $e^+$  system in preparation for this program of Ps\* research. The original  $e^+$  source had decayed to 7.5 mCi. This source was replaced with a stronger 28.5 mCi source reused from the ATRAP collaboration at CERN. The solid neon moderator was optimized to provide a slow  $e^+$  rate of  $7.3(14) \times 10^6 e^+/s$  ( $2.6(5) \times 10^5 e^+/s/mCi$ ). The stability of the Ne moderator was optimized with a decay rate of  $-3.3\%/day$  for the current source.

The  $e^+$  accumulator was optimized to trap the moderated  $e^+$  where a linear accumulation rate of  $1 \times 10^4 e^+/s/mCi$  was achieved. For increased  $e^+$  samples, the

electric potential structures of the buffer-gas accumulator were modified to accommodate larger numbers of stored  $e^+$  ( $>50 \times 10^6 e^+$  in 250 s). The nitrogen buffer-gas pressure was optimized for a faster  $e^+$  accumulation rate. To prepare compressed  $e^+$  for a localized charge-exchange collision, the radial profile of the moderated and pulsed  $e^+$  beam was imaged with an MCP-phosphor screen system. To study the effect of the rotating wall, a wide variety of experiment parameters were optimized for this research.

The moderated and trap-based  $e^+$  beams have been guided  $90^\circ$  out of the buffer-gas accumulator and directed towards a new Ps apparatus. A magnetic field model was generated to aid in the design of the  $e^+$  transfer guide to expand the apparatus while remaining in the confines of a small laboratory. The guide is composed of custom hand-wound coils and a large recuperated surplus hoop coil that produce a  $90^\circ$  bend in the trajectory for  $e^+$  exiting the  $e^+$  accumulator. A 100% transfer efficiency has been achieved in guiding the moderated beam to a gate valve before the Ps apparatus. A ramped  $e^+$  beam technique has been developed that enables single-event detection of  $e^+$  annihilations, similar to the moderated beam. The technique has been optimized to preserve the low-energy width of buffer-gas trapped  $e^+$  (200 meV), required for efficient charge-exchange.

The Ps apparatus was constructed for the experiment region where laser-controlled charge-exchange takes place. A thermal Cs oven was developed to emit a dense beam of ground state Cs atoms. These are laser excited by a two-step laser excitation to produce Cs\*. Laser systems were developed and these have been frequency-stabilized with a SD-DAVLL technique and a modulation lock technique to an EIT signal. Experimental methods have been developed to magnetically guide the ramped  $e^+$  beam towards the Cs\* to initiate Ps\* production. The Cs atoms are collected onto liquid-nitrogen cooled surfaces where cryogenics are provided from an exchangeable bulk dewar. The internal dewar has kept the components at cryogenic surfaces for over one year, despite several power outages on the campus, allowing all Cs to remain trapped on cold surfaces to protect the  $e^+$  buffer-gas accumulator. This system allows for both reloading of additional Cs under vacuum, and for collected Cs to be recuperated from the cold trap.

An electrostatic quadrupole guide has been developed to efficiently guide  $\text{Ps}^*$  states to the detection region. A data acquisition system has developed to detect  $e^+$  annihilations based on coincidence detection of the back-to-back 511 keV annihilations. A variety of  $\text{Ps}$  annihilation locations and processes were modelled and studied experimentally. A complex system of analog electronics triggers a pair of digitizers when a coincidence is detected and stores each detector output for post-analysis. A system of 4 gamma detectors is implemented, where the outputs are simultaneously digitized at the common trigger. The data is post-analyzed with strict coincidence timing conditions and for sorting events based on energy and timestamp.

A ramped monoenergetic  $e^+$  beam has been developed. Electric potentials slow the  $e^+$  at the charge-exchange region, and the  $e^+$  that overcome the potential barrier are magnetically guided towards the detection region. A loss of guided  $e^+$  occurs when the  $e^+$  are slowed to zero average velocity in the presence of  $\text{Cs}^*$ . This loss has been studied at a variety of  $\text{Cs}$  densities and  $\text{Cs}^*$  laser excitation intensities. With the 852 nm laser blocked, this effect is not seen with the Rydberg-excitation laser on or off, providing a strong indicator that it is due to Rydberg charge-exchange collisions. During  $\text{Ps}^*$  production trials, a blocking potential transmits  $\text{Ps}^*$  through the quadrupole guide to the detection region, and reflects  $e^+$  from entering. To date however, direct evidence of  $\text{Ps}^*$  guided to the annihilation plate has not been confirmed. Coincidence signals were categorized based on the  $e^+$  gamma spectrum, and compared to the expected rate produced by background signals. The gamma detector pair closer to the charge-exchange are susceptible to false coincidence signals where a loss in signal with  $\text{Cs}^*$  present was observed. The oven was operated at a relatively low temperature where a 1% to 10% charge-exchange efficiency was expected. This cautious approach was taken to observe any degradation of the delicate  $e^+$  source and buffer-gas accumulator. The continuously operated system is well prepared for 10 to 100 times more intense  $\text{Cs}$  beams for this challenging research objective.

Future work will require additional diagnostics of where the losses observed distribute to by adding additional detector pairs or systematically moving the detector position.

With further improvements to the apparatus, precision measurements of  $\text{Ps}^*$  states will be possible and can provide an independent measurement of fundamental constants for stringent tests of QED. The apparatus has been designed to support future pulsed  $\text{Ps}^*$  experiments using the pulsed  $e^+$  beam with Faraday cups to locate the beam trajectory. The pulsed  $e^+$  would charge-exchange with  $\text{Cs}^*$  in  $<200 \mu\text{s}$  with a large fraction annihilating near the nozzle. This generates a large prompt gamma signal to timestamp the time of expected  $\text{Ps}^*$  production. Slow  $\text{Ps}^*$  generated would be detected as delayed single-event annihilations relative to the prompt. These experiments will provide additional studies of the  $\text{Ps}^*$  such as lifetime determination of Ps Rydberg states, and the measured lifetimes can be compared to QED predictions.

# Bibliography

- [1] P.A M. Dirac. The quantum theory of the electron. *Proc. R. Soc. Lond., A*: 610–624, Jan 1928.
- [2] Carl D. Anderson. The positive electron. *Phys. Rev.*, 43:491–494, Mar 1933.
- [3] Martin Deutsch. Evidence for the formation of positronium in gases. *Phys. Rev.*, 82:455–456, May 1951.
- [4] Willis E. Lamb and Robert C. Retherford. Fine structure of the hydrogen atom by a microwave method. *Phys. Rev.*, 72:241–243, Aug 1947.
- [5] R. Pohl, A. Antognini, F. Nez, et al. The size of the proton. *Nature*, 466: 213–216, 2010.
- [6] N. Bezginov, T. Valdez, M. Horbatsch, A. Marsman, A. C. Vutha, and E. A. Hessels. A measurement of the atomic hydrogen lamb shift and the proton charge radius. 365(6457):1007–1012, 2019.
- [7] Axel Beyer, Lothar Maisenbacher, Arthur Matveev, Randolph Pohl, Ksenia Khabarova, Alexey Grinin, Tobias Lamour, Dylan C. Yost, Theodor W. Hänsch, Nikolai Kolachevsky, and Thomas Udem. The rydberg constant and proton size from atomic hydrogen. *Science*, 358(6359):79–85, 2017.
- [8] L. Gurung, T. J. Babij, S. D. Hogan, and D. B. Cassidy. Precision microwave spectroscopy of the positronium  $n = 2$  fine structure. *Phys. Rev. Lett.*, 125: 073002, Aug 2020.
- [9] Nagendra Mondal. Challenges and advances of positronium bose-einstein condensation. *AIP Advances*, 9:055310, 05 2019.

- [10] D. Cassidy and S. Hogan. Atom control and gravity measurements using rydberg positronium. *International Journal of Modern Physics: Conference Series*, 30:1460259, 01 2014.
- [11] M. W. Ritter, P. O. Egan, V. W. Hughes, and K. A. Woodle. Precision determination of the hyperfine-structure interval in the ground state of positronium. *Phys. Rev. A*, 30:1331–1338, Sep 1984.
- [12] A. P. Mills and G. H. Bearman. New measurement of the positronium hyperfine interval. *Phys. Rev. Lett.*, 34:246–250, Feb 1975.
- [13] M. S. Fee, A. P. Mills, S. Chu, E. D. Shaw, K. Danzmann, R. J. Chichester, and D. M. Zuckerman. Measurement of the positronium  $1^3s_1$ - $2^3s_1$  interval by continuous-wave two-photon excitation. *Phys. Rev. Lett.*, 70:1397–1400, Mar 1993.
- [14] D. Hagena, R. Ley, D. Weil, G. Werth, W. Arnold, and H. Schneider. Precise measurement of  $n=2$  positronium fine-structure intervals. *Phys. Rev. Lett.*, 71:2887–2890, Nov 1993.
- [15] S. Hatamian, R. S. Conti, and A. Rich. Measurements of the  $2^3s_1$ - $2^3p_j$  ( $j=0,1,2$ ) fine-structure splittings in positronium. *Phys. Rev. Lett.*, 58:1833–1836, May 1987.
- [16] A. P. Mills, S. Berko, and K. F. Canter. Fine-structure measurement in the first excited state of positronium. *Phys. Rev. Lett.*, 34:1541–1544, Jun 1975.
- [17] S. G. Karshenboim. Precision study of positronium: Testing bound state qed theory. *International Journal of Modern Physics A*, 19(23):38793896, Sep 2004.
- [18] B. S. Cooper, A. M. Alonso, A. Deller, T. E. Wall, and D. B. Cassidy. A trap-based pulsed positron beam optimised for positronium laser spectroscopy. *Review of Scientific Instruments*, 86(10):103101, 2015.

- [19] D. B. Cassidy, S. H. M. Deng, H. K. M. Tanaka, and A. P. Mills. Single shot positron annihilation lifetime spectroscopy. *Applied Physics Letters*, 88(19):194105, 2006.
- [20] A. Deller, A. M. Alonso, B. S. Cooper, S. D. Hogan, and D. B. Cassidy. Measurement of rydberg positronium fluorescence lifetimes. *Phys. Rev. A*, 93:062513, Jun 2016.
- [21] T. E. Wall, A. M. Alonso, B. S. Cooper, A. Deller, S. D. Hogan, and D. B. Cassidy. Selective production of rydberg-stark states of positronium. *Phys. Rev. Lett.*, 114:173001, Apr 2015.
- [22] A. Deller, A. M. Alonso, B. S. Cooper, S. D. Hogan, and D. B. Cassidy. Electrostatically guided rydberg positronium. *Phys. Rev. Lett.*, 117:073202, Aug 2016.
- [23] A. M. Alonso, B. S. Cooper, A. Deller, L. Gurung, S. D. Hogan, and D. B. Cassidy. Velocity selection of rydberg positronium using a curved electrostatic guide. *Phys. Rev. A*, 95:053409, May 2017.
- [24] T. D. Steiger and R. S. Conti. Formation of  $n=2$  positronium from untreated metal surfaces. *Phys. Rev. A*, 45:2744–2752, Mar 1992.
- [25] A. P. Mills, E. D. Shaw, R. J. Chichester, and D. M. Zuckerman. Positronium thermalization in  $\text{SiO}_2$  powder. *Phys. Rev. B*, 40:2045–2052, Aug 1989.
- [26] S.M. Curry and A.L. Schawlow. Measurements of the kinetic energy of free positronium formed in mgo. *Physics Letters A*, 37(1):5 – 6, 1971. ISSN 0375-9601.
- [27] M Charlton, T C Griffith, G R Heyland, K S Lines, and G L Wright. The energy dependence of positronium formation in gases. *Journal of Physics B: Atomic and Molecular Physics*, 13(24):L757–L760, dec 1980.
- [28] A. P. Mills and E. M. Gullikson. Solid neon moderator for producing slow positrons. *Applied Physics Letters*, 49(17):1121–1123, 1986.

- [29] C. M. Surko, M. Leventhal, and A. Passner. Positron plasma in the laboratory. *Phys. Rev. Lett.*, 62:901–904, Feb 1989.
- [30] D. B. Cassidy, P. Crivelli, T. H. Hisakado, L. Liskay, V. E. Meline, P. Perez, H. W. K. Tom, and A. P. Mills. Positronium cooling in porous silica measured via doppler spectroscopy. *Phys. Rev. A*, 81:012715, Jan 2010.
- [31] D. B. Cassidy, T. H. Hisakado, H. W. K. Tom, and A. P. Mills. Efficient production of rydberg positronium. *Phys. Rev. Lett.*, 108:043401, Jan 2012.
- [32] C. J. Baker, D. Edwards, C. A. Isaac, H. H. Telle, D. P. van der Werf, and M. Charlton. Excitation of positronium: from the ground state to rydberg levels. *Journal of Physics B: Atomic, Molecular and Optical Physics*, 51(3):035006, Jan 2018.
- [33] A Deller, D Edwards, T Mortensen, C A Isaac, D P van der Werf, H H Telle, and M Charlton. Exciting positronium with a solid-state UV laser: the doppler-broadened lyman-transition. *Journal of Physics B: Atomic, Molecular and Optical Physics*, 48(17):175001, jul 2015.
- [34] A. P. Mills. Time bunching of slow positrons for annihilation lifetime and pulsed laser photon absorption experiments. *Applied physics*, 22(3):273–276, Jul 1980. ISSN 1432-0630.
- [35] C. H. Storry, A. Speck, D. Le Sage, N. Guise, G. Gabrielse, D. Grzonka, W. Oelert, G. Schepers, T. Sefzick, H. Pittner, M. Herrmann, J. Walz, T. W. Hänsch, D. Comeau, and E. A. Hessels. First laser-controlled antihydrogen production. *Phys. Rev. Lett.*, 93:263401, Dec 2004.
- [36] R McConnell et al. Large numbers of cold positronium atoms created in laser-selected rydberg states using resonant charge exchange. *J. Phys. B: At. Mol. Opt. Phys.*, 49:064002, 2016.
- [37] E. A. Hessels, D. M. Homan, and M. J. Cavagnero. Two-stage rydberg charge exchange: An efficient method for production of antihydrogen. *Phys. Rev. A*, 57:1668–1671, Mar 1998.

- [38] A. Kellerbauer et al. Proposed antimatter gravity measurement with an anti-hydrogen beam. *Nuclear Instruments and Methods in Physics Research Section B: Beam Interactions with Materials and Atoms*, 266(3):351 – 356, 2008.
- [39] A. M. Alonso, L. Gurung, B. A. D. Sukra, S. D. Hogan, and D. B. Cassidy. State-selective electric-field ionization of rydberg positronium. *Phys. Rev. A*, 98:053417, Nov 2018.
- [40] E. E. Salpeter and H. A. Bethe. A relativistic equation for bound-state problems. *Phys. Rev.*, 84:1232–1242, Dec 1951.
- [41] Michael A. Stroschio. Positronium: A review of the theory. *Physics Reports*, 22(5):215 – 277, 1975.
- [42] K.-H. Weber and Craig J. Sansonetti. Accurate energies of ns, np, nd, nf, and ng levels of neutral cesium. *Phys. Rev. A*, 35:4650–4660, Jun 1987.
- [43] Philip M. Stone. Cesium oscillator strengths. *Phys. Rev.*, 127:1151–1156, Aug 1962.
- [44] Douglas S. McGregor. Materials for gamma-ray spectrometers: Inorganic scintillators. *Annual Review of Materials Research*, 48(1):245–277, 2018.
- [45] D. W. Fitzakerley. *Antihydrogen via Two-Stage Charge-Exchange*. PhD thesis, 2015.
- [46] V.A. Kuzminikh, I.A. Tsekhanovski, and S.A. Vorobiev. Backscattering of positrons from thick targets. *Nuclear Instruments and Methods*, 118(1):269 – 271, 1974. ISSN 0029-554X.
- [47] G.R. Massoumi, Peter J. Schultz, W.N. Lennard, and J. Ociepa. Positron emission yields for encapsulated  $^{22}\text{Na}$  sources. *Nuclear Instruments and Methods in Physics Research Section B: Beam Interactions with Materials and Atoms*, 30(4):592 – 597, 1988. ISSN 0168-583X.
- [48] M.P. Petkov, K.G. Lynn, L.O. Roellig, and T.D. Troev. An investigation of positrons interacting with solid argon, krypton and xenon. *Applied Surface*

- Science*, 116:13 – 18, 1997. ISSN 0169-4332. Proceedings of the Seventh International Workshop on Slow-Positron Beam Techniques for Solids and Surfaces.
- [49] A. Vehanen, K. G. Lynn, Peter J. Schultz, and M. Eldrup. Improved slow-positron yield using a single crystal tungsten moderator. *Applied Physics A*, 32(3):163–167, Nov 1983. ISSN 1432-0630.
- [50] E. M. Gullikson and A. P. Mills. Positron dynamics in rare-gas solids. *Phys. Rev. Lett.*, 57:376–379, Jul 1986.
- [51] R. G. Greaves and C. M. Surko. Solid neon moderator for positron-trapping experiments. *Canadian Journal of Physics*, 74(7-8):445–448, 1996.
- [52] A. Fardad. Positron moderation and detection for positronic atoms. Master’s thesis, York University, 2013.
- [53] D. Hanneke, S. Fogwell, and G. Gabrielse. New measurement of the electron magnetic moment and the fine structure constant. *Phys. Rev. Lett.*, 100:120801, Mar 2008.
- [54] M Amoretti, Claude Amsler, Germano Bonomi, A Bouchta, P. Bowe, C Carraro, C Cesar, M Charlton, M Collier, Michael Doser, V Filippini, Kevin Fine, Andrea Fontana, M Fujiwara, Ryo Funakoshi, P Genova, J Hangst, R Hayano, Michael Holzscheiter, and Dirk van der Werf. Production and detection of cold antihydrogen atoms. *Nature*, 419:456–9, 11 2002.
- [55] G. Gabrielse, N. S. Bowden, P. Oxley, A. Speck, C. H. Storry, J. N. Tan, M. Wessels, D. Grzonka, W. Oelert, G. Schepers, T. Sefzick, J. Walz, H. Pittner, T. W. Hänsch, and E. A. Hessels. Background-free observation of cold antihydrogen with field-ionization analysis of its states. *Phys. Rev. Lett.*, 89:213401, Oct 2002.
- [56] G. Gabrielse, L. Haarsma, and S.L. Rolston. Open-endcap penning traps for high precision experiments. *International Journal of Mass Spectrometry and Ion Processes*, 88(2):319 – 332, 1989. ISSN 0168-1176.

- 
- [57] T. J. Murphy and C. M. Surko. Positron trapping in an electrostatic well by inelastic collisions with nitrogen molecules. *Phys. Rev. A*, 46:5696–5705, Nov 1992.
- [58] C. Surko, G. Gribakin, and S. Buckman. Low-energy positron interactions with atoms and molecules. *Journal of Physics B: Atomic, Molecular and Optical Physics*, 38:R57, 03 2005.
- [59] Soumen Ghosh, J Danielson, and clifford surko. Energy distribution and adiabatic guiding of a solid-neon-moderated positron beam. *Journal of Physics B: Atomic, Molecular and Optical Physics*, 02 2020.
- [60] J. P. Marler and C. M. Surko. Positron-impact ionization, positronium formation, and electronic excitation cross sections for diatomic molecules. *Phys. Rev. A*, 72:062713, Dec 2005.
- [61] R. Greaves and C. Surko. Inward transport and compression of a positron plasma by a rotating electric field. *Physical review letters*, 85:1883–6, 09 2000.
- [62] F. Anderegg, E. M. Hollmann, and C. F. Driscoll. Rotating field confinement of pure electron plasmas using trivelpiece-gould modes. *Phys. Rev. Lett.*, 81:4875–4878, Nov 1998.
- [63] F. Anderegg. *Trapped Charged Particles*, chapter Rotating Wall Technique and Centrifugal Separation, pages 221–238.
- [64] S. J. Gilbert, C. Kurz, R. G. Greaves, and C. M. Surko. Creation of a monoenergetic pulsed positron beam. *Applied Physics Letters*, 70(15):1944–1946, 1997.
- [65] M. R. Natisin, J. R. Danielson, and C. M. Surko. Formation mechanisms and optimization of trap-based positron beams. *Physics of Plasmas*, 23(2):023505, 2016.
- [66] Dian-Qiang Su, Teng-Fei Meng, Zhong-Hua Ji, Jin-Peng Yuan, Yan-Ting Zhao, Lian-Tuan Xiao, and Suo-Tang Jia. Application of sub-doppler davll

- to laser frequency stabilization in atomic cesium. *Appl. Opt.*, 53(30):7011–7016, Oct 2014.
- [67] Michael Fleischhauer, Atac Imamoglu, and Jonathan P. Marangos. Electromagnetically induced transparency: Optics in coherent media. *Rev. Mod. Phys.*, 77:633–673, Jul 2005.
- [68] M. Weel and A. Kumarakrishnan. Tutorial: Laser-frequency stabilization using a lock-in amplifier. *Canadian Journal of Physics - CAN J PHYS*, 80:1449–1458, 12 2002.
- [69] V. S. (Vladimir S.) Lebedev. *Physics of highly excited atoms and ions*. Springer series on atoms + plasmas, 22. Springer Verlag, Berlin ;. ISBN 354064234X.
- [70] C. G. Wade. *Terahertz Wave Detection and Imaging with a Hot Rydberg Vapour*. PhD thesis, Durham University, 2017.
- [71] D. Halwidl. *Development of an Effusive Molecular Beam Apparatus*. Best-Masters. Springer Spektrum, 1 edition, 2016.
- [72] M. Barbisan, S. Cristofaro, L. Zampieri, R. Pasqualotto, and A. Rizzolo. Laser absorption spectroscopy studies to characterize cs oven performances for the negative ion source SPIDER. *Journal of Instrumentation*, 14(12):C12011–C12011, dec 2019.
- [73] Mani Farjam and Herbert B. Shore. Positron work function and deformation potential. *Phys. Rev. B*, 36:5089–5092, Oct 1987.